ORIGINAL CONTAINS
COLOR ILLUSTRATIONS

Microburst Vertical Wind Estimation From Horizontal Wind Measurements

Dan D. Vicroy
Langley Research Center • Hampton, Virginia

December 1994

This publication is available from the following sources:

Contents

Summary

The vertical wind or downdraft component of a microburst-generated wind shear can significantly degrade airplane performance. Doppler radar and lidar are two sensor technologies being tested to provide flight crews with early warning of the presence of hazardous wind shear. An inherent limitation of Doppler-based sensors is the inability to measure velocities perpendicular to the line of sight; this results in an underestimate of the total wind shear hazard. One solution to the line-of-sight limitation is to use a vertical wind model to estimate the vertical component from the horizontal wind measurement. The objective of this study was to assess the ability of simple vertical wind models to improve the hazard prediction capability of an airborne Doppler sensor in a realistic microburst environment. Both simulation and flight test measurements were used to test the vertical wind models. The results indicate that, in the altitude region of interest (at or below 300 m), the simple vertical wind models improved the hazard estimate. The radar simulation study showed that the magnitude of the performance improvement was altitude dependent. The altitude of maximum performance improvement occurred at about 300 m. At lower altitudes, the improvement was minimized by the diminished contribution of the vertical wind. The vertical hazard estimate errors from flight tests were less than those of the radar simulation study.

Introduction

Wind shear is considered by many in the aviation industry to be a major safety issue. Numerous accidents and incidents have occurred that were attributed to low-altitude wind shear, which can be found in a variety of weather conditions such as gust fronts, sea breeze fronts, and mountain waves (ref. 1). However, hazardous wind shear is most often associated with the convective outflow of thunderstorms known as microbursts. A microburst is a strong localized downdraft that causes a significant outflow as it impacts the ground (ref. 2). The hazard of a microburst encounter occurs when a head wind rapidly shifts to a tail wind as the airplane penetrates the outflow, which reduces the airspeed and the potential rate of climb of the airplane. The potential rate of climb of the airplane is further reduced by the microburst downdraft. The general effect on the airplane is a rapid loss of energy from which it may not have enough altitude, airspeed, or thrust to overcome.

The National Aeronautics and Space Administration, in a joint effort with the Federal Aviation Administration, has been conducting research in the development of forward-look, airborne, wind shear detection technologies. Forward-look systems warn the flight crew of the presence of wind shear at low altitude (under 305 m) in time to avoid the affected area or to prepare for and escape from the encounter. A fundamental requirement of such a wind shear detection system is the ability to reliably estimate the magnitude of an upcoming wind shear hazard along the flight path of the airplane. Doppler radar and lidar are two technologies being tested to provide this capability. Both measure the Doppler shift from rain drops, aerosols, and other debris in the air to determine the line-of-sight relative velocity of the air.

An inherent limitation of this system is its inability to measure velocities perpendicular to the line of sight. The presence of a microburst can be detected by measuring the divergence of the horizontal velocity profile; however, the inability to measure the downdraft can result in a significant underestimate of the magnitude and spatial extent of the hazard (ref. 3).

One solution to the line-of-sight limitation of Doppler sensors is to use a theoretical or empirical model of a microburst to estimate the perpendicular velocities from the measured line-of-sight values. A preliminary assessment of this technique showed that the microburst-generated downdraft could be estimated at low altitudes with very simple vertical wind models (ref. 3). This study was, however, limited in scope. It assumed perfect knowledge of the horizontal wind field produced by an idealized axisymmetric microburst simulation.

The objective of this study was to assess the ability of simple vertical wind models to improve the hazard prediction of an airborne Doppler sensor in a realistic microburst environment. Both simulation and flight test measurements were used to test the vertical wind models. A Doppler radar simulation was used with a high-fidelity asymmetric microburst model to establish the performance limits of the vertical wind models and to establish the effects of radar signal noise and measurement errors. Flight test measurements from an airborne Doppler radar were used to compute the vertical wind velocity in front of the airplane. These velocities were compared with onboard in situ measurements. The flight test results were also compared with the expected results established from the radar simulation.

Although the simulation and the flight test results presented in this report are for an airborne Doppler radar system, the techniques for estimating the vertical wind velocity should be applicable to other Doppler-based sensors such as lidar. However,

the performance will vary with the signal properties of the sensor and the spatial resolution.

This paper reviews the wind shear hazard index known as the F-factor, which is used extensively to quantify the hazard of a wind shear encounter. The microburst simulation data sets used in the radar simulation are introduced. The coordinate system, the two vertical wind velocity estimation techniques, the radar simulation, and the flight test data are then described. The method of analysis and results are also presented.

Symbols

F	wind shear hazard index
F_h	horizontal component of wind shear hazard index
F_v	vertical component of wind shear hazard index
$\overline{F}$	wind shear hazard index averaged over specified distance
$\overline{F_v}$	vertical wind shear hazard index averaged over specified distance
$f(r_m)$	empirical model radial shaping function of radial wind velocity, m/s
g	gravitational acceleration, m/s^2
$g(r_m^2)$	empirical model radial shaping function of vertical wind velocity
$p(z_m)$	empirical model vertical shaping function of radial wind velocity
$q(z_m)$	empirical model vertical shaping function of vertical wind velocity, m/s
R	linear correlation coefficient
Res	residual of linear least-squares curve fit of radial velocity profile, m/s
r_c	sensor radial coordinate to origin of microburst reference system, m
r_m	microburst-referenced radial coordinate, m
r_{max}	microburst radial coordinate of maximum horizontal wind, m
r_{min}	minimum radar range
r_s	airplaine sensor-referenced radial coordinate, m
$\mathbf{T}_{\phi_s}$	velocity transformation matrix for sensor elevation angle
$\mathbf{T}_{\theta_m}$	velocity transformation matrix for microburst azimuth angle
$\mathbf{T}_{\theta_s}$	velocity transformation matrix for sensor azimuth angle
t	time
$\mathbf{U}_m$	microburst-referenced wind vector, m/s
$\mathbf{U}_s$	sensor-referenced wind vector, m/s
$\mathbf{U}_\infty$	microburst-referenced free-stream wind vector, m/s
u_m	microburst-referenced radial wind, m/s
u_s	sensor-referenced radial wind, m/s
u_∞	microburst-referenced free-stream radial wind, m/s
$\dot{u}$	time rate of change of horizontal wind component (tailwind positive), m/s^2
V	true airspeed at time of radar measurement, m/s
V_g	ground speed, m/s
v_m	microburst-referenced velocity in θ_m direction, m/s
v_s	sensor-referenced velocity in θ_s direction, m/s
w	vertical wind component (updraft positive), m/s
w_s	sensor-referenced velocity in ϕ_s direction, m/s
w_m	microburst-referenced vertical wind component, m/s
x	coordinate in west-east direction about center of microburst, m
y	coordinate in south-north direction about center of microburst, m
z	coordinate in vertical direction, m
z_m	microburst-referenced vertical coordinate, m
z_{max}	altitude of maximum horizontal wind, m
z_s	altitude of sensor, m
α	empirical model shaping function variable
λ	empirical model scaling factor, s^{-1}

Δr_s	sensor range bin length, m
Δt	time shift between radar and in situ measurement, s
$\eta(z_m)$	empirical model altitude weighting function, m
θ_c	sensor azimuth coordinate to microburst reference system origin, deg
θ_m	microburst-referenced azimuth coordinate, deg
θ_s	airplane sensor-referenced azimuth angle, deg
θ_∞	microburst-referenced azimuth of free-stream wind, deg
ϕ_s	airplane sensor-referenced elevation angle, deg

Abbreviations:

AWDRS	Airborne Windshear Doppler Radar Simulation Program
TASS	Terminal Area Simulation System
2D	two-dimensional
3D	three-dimensional

Wind Shear Hazard Index

The magnitude of the hazard posed by a microburst to an airplane can be quantified through the F-factor (ref. 4). The F-factor is a hazard index that represents the rate of specific energy loss because of wind shear. For straight and level flight, the F-factor can be expressed as

$$F = \frac{\dot{u}}{g} - \frac{w}{V} \qquad (1)$$

Positive values of F indicate a performance-decreasing condition. Conversely, negative values indicate a performance-increasing condition. The F-factor is directly related to the climb gradient capability of the airplane. For example, a value of F of 0.2 would indicate a loss in climb gradient capability of 0.2 rad (11.5°). If an airplane had a maximum climb angle capability of 10°, it would be unable to maintain level flight in that sustained wind shear environment. A wind shear is considered hazardous to landing or departing airplanes if the F-factor average over 1 km is 0.1 or greater (ref. 4).

The F-factor can be separated into a horizontal component F_h and a vertical component F_v, so that

$$F = F_h + F_v \qquad (2)$$

where

$$F_h = \frac{\dot{u}}{g} \qquad (3)$$

$$F_v = -\frac{w}{V} \qquad (4)$$

Doppler-based wind shear sensors can only measure the line-of-sight divergence of the wind and therefore can only determine the horizontal F-factor component. The inability to measure the vertical component can result in a significant underestimate of the magnitude of the microburst hazard. For landing or departing airplanes, the vertical component of F can exceed half the total F-factor.

Microburst Simulation Model

The Terminal Area Simulation System (TASS) high-fidelity microburst simulation model was used in the development and the analysis of the downdraft estimation techniques discussed in this paper. TASS is a time-dependent, multidimensional, non-hydrostatic, numerical cloud model that has been used extensively in the study of microbursts (refs. 5 and 6). The model is initiated with the observed environmental conditions (altitude profiles of temperature, humidity, and wind) that existed prior to microburst development and outputs a three-dimensional time history of radar reflectivity, winds, temperature, pressure, water vapor, rainwater, snow, hail, and cloud water. The model has been validated with both ground-based and airborne measurements (refs. 6 and 7). Microburst data sets generated with TASS have also been selected by the Federal Aviation Administration as test cases for certifying forward-look wind shear sensors (ref. 8). Although TASS is much too complex to be practical as a downdraft estimation model, it is very useful for generating the high-fidelity data sets necessary to evaluate such models.

Two TASS microburst data sets were used in this study. One was an axisymmetric case (symmetric about the vertical axis) with a 20-m grid resolution, and the other was a three-dimensional asymmetric case with a 200-m horizontal grid.

Axisymmetric Microburst Data Set

The axisymmetric data set used in the study reported herein was also used in an earlier feasibility study of vertical wind estimation techniques (ref. 3).

In this study, it is used to illustrate the general characteristics of a microburst wind field. These characteristics are discussed in the section "Vertical Wind Models." The axisymmetric data set extended from the microburst core to 4000 m radially and from the ground to 600 m vertically. This was a subset of the larger TASS modeled domain. The model was initiated with the atmospheric conditions measured before a microburst event on August 2, 1985, at Dallas-Fort Worth International Airport (ref. 9). Four different times in the microburst simulation were selected, each 2 min apart. Figure 1 shows the wind vector plots for the four time periods selected. The first was just before the downdraft impacted the ground, which was at 9 min into the microburst simulation. The second was just after the downdraft hit the ground and began to spread out, which was approximately the time of maximum horizontal shear. The third was at a point when the outflow vortex was well defined, and the last, near the end of the life cycle of the microburst event.

Contour plots of F-factor for an airplane flying level at 130 knots are also shown in figure 1. Figure 2 shows the same data sets with the F-factor contours computed without the vertical winds. The magnitude and spatial extent of the detectable hazard are clearly diminished. This further illustrates the need for some means of determining the magnitude of the vertical winds.

Asymmetric Microburst Data Set

The asymmetric data set was used in the Doppler radar simulation, which is described in section "Radar Simulation." The data set was generated from an atmospheric sounding taken before a microburst event on July 11, 1988, in Denver. This event was inadvertently encountered by four successive airplanes on final approach to the Stapleton International Airport in Denver. This data set accurately simulates the major features of the microburst-producing storm and is discussed in detail in reference 7. The data set extends 12 km in the west-east direction (x-direction), 12 km in the south-north direction (y-direction), and 2 km vertically (z-direction), with a vertical resolution of approximately 80 m. Only the data set from the lowest 600 m was used in this study. Three times from this simulation were selected, each 1 min apart. Figure 3 shows the horizontal cross section of the wind vector field at an altitude of 283 m for each of the three times selected. Also shown in the figure is an outline of the simulated radar scan area that is discussed later. At the bottom of the figure is the vertical cross section of the wind vector field through the location

$y = 0$. The three times selected correspond to an instant roughly 1 min prior, during, and 1 min after the first of the four airliners encountered the microburst. These times are also near the time of maximum shear produce by the microburst.

Velocity Transformation Equations

Estimating the vertical wind with a microburst model requires a transformation between the cylindrical coordinate system (r_m, θ_m, z_m) of the microburst and the spherical coordinate system (r_s, ϕ_s, θ_s) of the airplane sensor. The sensor is assumed to be inertially referenced so that the airplane motion is compensated for and is removed from the sensor-measured velocities. Figure 4 shows the two coordinate systems and their corresponding velocity components. The wind field is assumed to be a microburst wind field superimposed on a uniform horizontal wind field. The microburst vertical axis is located in the sensor coordinate system at (r_c, ϕ_s, θ_c). The origin of the sensor coordinate system is at an altitude z_s above the origin of the microburst coordinate system. Derivation of the velocity transformation equations and their spatial derivatives are provided in the appendix.

Vertical Wind Models

Two vertical wind models are analyzed in this report. The derivation of these models is provided in this section. Both of the models determine the vertical divergence $\partial w_m / \partial z_m$ from the measured radial wind profile with the mass continuity equation. The vertical wind w_m is then determined from a model-based relationship between the vertical divergence and the vertical wind with altitude.

Estimating Vertical Divergence

The mass continuity equation for incompressible flow in the microburst cylindrical coordinate system is

$$\frac{1}{r_m}\frac{\partial(r_m u_m)}{\partial r_m} + \frac{1}{r_m}\frac{\partial v_m}{\partial \theta_m} + \frac{\partial w_m}{\partial z_m} = 0 \qquad (5)$$

If the microburst is assumed to be symmetrical about the vertical axis ($\partial U_m / \partial \theta_m = 0$) with no rotational flow ($v_m = 0$), then equation (5) simplifies to

$$\frac{u_m}{r_m} + \frac{\partial u_m}{\partial r_m} + \frac{\partial w_m}{\partial z_m} = 0 \qquad (6)$$

The microburst radial velocity u_m and the radial shear $\partial u_m / \partial r_m$ can be determined from the sensor measurements and the transformation equations of

the appendix. If the sensor elevation angle is assumed to be level with the horizon ($\phi_s = 0$), then equation (7), which is equation (A46), can be used to relate the sensor-measured radial shear $\partial u_s / \partial r_s$ to the microburst-referenced values:

$$\frac{\partial u_s}{\partial r_s} = \frac{\partial u_m}{\partial r_m} \cos^2(\theta_m - \theta_s) + \frac{u_m}{r_m} \sin^2(\theta_m - \theta_s) \quad (7)$$

Figures 5 and 6, reproduced from reference 3, show the radial profiles of the radial and the vertical wind from the symmetrical microburst data set. Figure 5 shows that near the core of the microburst (from $r = 0$ to $r \approx 1200$ m) the radial velocity variation is nearly linear. Comparing figure 5 with figure 6 shows that this linear region corresponds to the primary downdraft region of the microburst for each of the four times. The vertical velocity variations outside the core area are due to the outflow vortex ring, which expands radially with time. In the linear core region,

$$\frac{\partial u_m}{\partial r_m} \approx \frac{u_m}{r_m} \quad (8)$$

and equation (7) simplifies to

$$\frac{\partial u_s}{\partial r_s} = \frac{\partial u_m}{\partial r_m} = \frac{u_m}{r_m} \quad (9)$$

Combining equation (9) with equation (6) yields a simple relationship for the vertical wind divergence as a function of the sensor-measured radial shear in the core of the microburst:

$$\frac{\partial w_m}{\partial z_m} = -\left(\frac{\partial u_m}{\partial r_m} + \frac{u_m}{r_m} \right) = -2 \frac{\partial u_s}{\partial r_s} \quad (10)$$

This relationship is not valid outside the microburst core where the radial velocity profile becomes non-linear. As the distance from the microburst core increases, the ratio u_m/r_m becomes small. If this term is neglected, then equations (6) and (7) become

$$\frac{\partial u_m}{\partial r_m} + \frac{\partial w_m}{\partial z_m} = 0 \quad (11)$$

and

$$\frac{\partial u_s}{\partial r_s} = \frac{\partial u_m}{\partial r_m} \cos^2(\theta_m - \theta_s) \quad (12)$$

respectively. Since $0 \leq \cos^2(\theta_m - \theta_s) \leq 1$, then

$$\frac{\partial u_s}{\partial r_s} \leq \frac{\partial u_m}{\partial r_m} \quad (13)$$

or

$$\frac{\partial u_s}{\partial r_s} \leq -\frac{\partial w_m}{\partial z_m} \quad (14)$$

If this inequality is approximated as an equality, then the magnitude of the resultant vertical wind divergence estimate outside the microburst core may be low. Underestimating the magnitude of the divergence outside the core should not adversely impact the hazard estimate since the vertical wind in this region is generally characterized as either performance-increasing updrafts or small scale downdrafts, as shown in figure 6. Therefore, a practical vertical divergence estimate outside the microburst core is

$$\frac{\partial w_m}{\partial z_m} = -\frac{\partial u_s}{\partial r_s} \quad (15)$$

The vertical wind divergence can be estimated from the sensor-measured radial wind profile with equations (10) and (15). However, these equations require the core of the microburst to be identified. The method used to identify the core of the microburst from the sensor-measured radial velocity profile is discussed in the section "Analysis and Results."

Linear Model

The linear model is the simplest of the two vertical wind models used in this study. The model is based on the assumption that there is no vertical wind at the ground and it increases linearly with altitude (i.e., $\partial w_m / z_m = $ Constant). The vertical wind can be computed from the vertical wind divergence as

$$w_m = \frac{\partial w_m}{\partial z_m} z_m \quad (16)$$

Figure 7 shows the vertical wind variation with altitude at the center of the microburst presented in figures 5 and 6. The assumption of linearity appears reasonable near the center, particularly at altitudes below 400 m. At higher altitudes the linearity begins to break down. Figure 8 shows the vertical wind profile at a radius of 2000 m; the linearity breaks down at this location as well. This nonlinearity occurs primarily because of the outflow vortex, which is generated when the downdraft core impacts the ground and begins to diverge horizontally (ref. 3). The degree to which these nonlinearities introduce errors into the downdraft calculation is discussed in the section "Analysis and Results."

Empirical Model

The empirical vertical wind model is based on measurements of several microburst events. This model utilizes the empirical microburst model developed by Oseguera and Bowles (ref. 10) and subsequently modified by Vicroy (ref. 11). The model is

an axisymmetric, steady state model that uses shaping functions to simulate boundary layer effects and to satisfy the mass continuity equation. The mass continuity equation (eq. 6) can be satisfied by solutions of the form

$$u_m = f(r_m)p(z_m) \qquad (17)$$

$$w_m = g(r_m^2)q(z_m) \qquad (18)$$

provided

$$\frac{\partial[r_m f(r_m)]}{\partial r_m^2} = \frac{\lambda}{2}g(r_m^2) \qquad (19)$$

$$\frac{\partial q(z_m)}{\partial z_m} = -\lambda p(z_m) \qquad (20)$$

where $f(r_m)$ and $g(r_m^2)$ are the empirical radial shaping functions for the radial and the vertical wind velocities, respectively; $p(z_m)$ and $q(z_m)$ are the vertical empirical shaping functions for the radial and the vertical wind velocities, respectively; and λ is a scale factor. The characteristic shape of the radial and the vertical shaping functions is shown in figures 9 and 10. The shaping functions are used to approximate the characteristic profile of the microburst winds. The radial shaping functions appear to compare well with the axisymmetric microburst profiles presented in figures 5 and 6, particularly for the first two times. The radial profiles of the last two times show the growth of the outflow vortex, which is not modeled by the shaping function.

The equations for the shaping functions are

$$f(r_m) = \frac{\lambda r_m}{2}\exp\left[\frac{2 - (r_m^2/r_{max}^2)^\alpha}{2\alpha}\right] \qquad (21)$$

$$g(r_m^2) = \left[1 - \frac{1}{2}\left(\frac{r_m^2}{r_{max}^2}\right)^\alpha\right]\exp\left[\frac{2 - (r_m^2/r_{max}^2)^\alpha}{2\alpha}\right] \qquad (22)$$

$$p(z_m) = \exp\left(c_1\frac{z_m}{z_{max}}\right) - \exp\left(c_2\frac{z_m}{z_{max}}\right) \qquad (23)$$

$$q(z_m) = -\lambda\left[\frac{z_{max}}{c_1}\exp\left(c_1\frac{z_m}{z_{max}} - 1\right)\right. \\ \left. - \frac{z_{max}}{c_2}\exp\left(c_2\frac{z_m}{z_{max}} - 1\right)\right] \qquad (24)$$

with

$$c_1 = -0.15 \qquad (25)$$

$$c_2 = -3.2175 \qquad (26)$$

$$z_{max} = 60 \text{ m} \qquad (27)$$

The values of c_1, c_2, and z_{max} were selected from curve fits of data from several microburst events. Differentiating equation (18) with respect to altitude yields

$$\frac{\partial w_m}{\partial z_m} = g(r_m^2)\frac{\partial q(z_m)}{\partial z_m} \qquad (28)$$

Substituting equation (20) for $\partial q(z_m)/\partial z_m$ yields

$$\frac{\partial w_m}{\partial z_m} = -\lambda p(z_m)g(r_m^2) \qquad (29)$$

Combining equation (29) with equation (18) yields

$$w_m = \frac{-q(z_m)}{\lambda p(z_m)}\frac{\partial w_m}{\partial z_m} = \eta(z_m)\frac{\partial w_m}{\partial z_m} \qquad (30)$$

where

$$\eta(z_m) = \frac{\frac{z_{max}}{c_1}\left[\exp\left(c_1\frac{z_m}{z_{max}} - 1\right)\right]}{\exp\left(c_1\frac{z_m}{z_{max}}\right) - \exp\left(c_2\frac{z_m}{z_{max}}\right)} \\ - \frac{\frac{z_{max}}{c_2}\left[\exp\left(c_2\frac{z_m}{z_{max}} - 1\right)\right]}{\exp\left(c_1\frac{z_m}{z_{max}}\right) - \exp\left(c_2\frac{z_m}{z_{max}}\right)} \qquad (31)$$

The vertical wind can now be computed from the vertical wind divergence and the altitude dependent function η.

Radar Simulation

The effects of measurement noise and signal processing techniques on the vertical wind estimate were determined with the Airborne Windshear Doppler Radar Simulation (AWDRS) Program (ref. 12). The simulation program computes the airborne radar signal returns for a given TASS microburst simulation and ground clutter map. The radar simulation includes algorithms for signal filtering and automatic gain control, as well as computing in-phase and quadrature base-band signal components, Doppler velocity, spectral width, and F-factor. The AWDRS program requires the relative location of the airplane and the microburst to the runway touchdown point and the radar system parameters, such as antenna pattern, pulse width, transmitted power, and antenna elevation.

The AWDRS program was initialized with the input data shown in table 1. The input data that varied between runs, namely the airplane starting range and the microburst position, are presented in table 2. The TASS generated asymmetric microburst data set was used for the radar simulation runs. The airplane and the microburst starting positions

were selected so that the airplane was at the same horizontal location relative to the microburst, and at the desired test altitude during the third scan of the simulation run. The data from the third scan of each simulation were used in the analysis. The third scan was selected to allow temporal filtering schemes within the simulation to initialize. Scan data were collected at six altitudes, from 100 to 600 m in 100-m increments, for each of the three times ($t = 49$, 50, and 51 min). The microburst wind field was frozen in time during each radar simulation run. The radar simulation scan area is outlined on the microburst wind vector plots shown in figure 3. The azimuth scan covered $-21°$ to $21°$, in $3°$ increments. Each scan line consisted of 30 range bins each 150 m long, with the initial range bin 425 m in front of the airplane. The resultant scan measurement grid is depicted in figure 11. The radar antenna elevation angle was set to 0 (level with the horizon) for all but the two lowest scan altitudes. At those altitudes, the elevation angle was set slightly above the horizon to minimize ground clutter returns. The elevation angle for the 100- and 200-m scans was $1.185°$ and $0.470°$, respectively. Contour plots of the true radial velocity and the simulated radar measurement with clutter and noise are shown in figure 12, for each of the three microburst cases.

Flight Test Data

A series of flight tests were conducted during the summers of 1991 and 1992 with a Transport Systems Research Vehicle (TSRV) Boeing 737-100 airplane at Langley that was equipped with a variety of prototype wind shear detection systems. The tests were conducted near Orlando, Florida, and Denver, Colorado. These two locations were selected based on their climatology, which is conducive to microburst development, and the availability of ground-based Doppler weather radar coverage. The Doppler weather radar was used to identify and to direct the research airplane to potential microburst activity. The microburst penetrations were typically flown at airspeeds between 210 and 230 knots and altitudes between 244 and 335 m. Details of the flight test procedure can be found in reference 13.

There were three forward-look wind shear detection sensors onboard the airplane: a passive infrared sensor, a lidar, and a Doppler radar (refs. 14–17). The ground-based Doppler weather radar wind divergence measurements were also transmitted to the airplane via radio data link and processed to compute F-factor estimates. The airplane was also equipped with a reactive, or in situ, system that computed the F-factor of the airspace the airplane was cur-

rently flying through (ref. 18). The in situ F-factor was used as a truth measurement for validation of the forward-look wind shear detection sensors. The F-factor predicted from the forward-look sensor was compared with the in situ measurement of the airplane as it penetrated the scanned airspace. The flight data in this study were limited to the onboard Doppler radar and the in situ measurements.

A limited subset of the vast flight data collected was selected for analysis in this study. This data selection was based on the following criteria:

1. The Doppler radar had to be operating at an antenna elevation of 0 (i.e., level with the horizon) with a pulse width of 0.96 μsec.

2. The airplane had to be flying nearly straight and level.

These flight requirements ensured that the airplane flew through the same airspace that was scanned by the radar. The pulse width restriction ensured that the radar range bin size was the same bin size used in the earlier radar simulation study. The microburst events selected for analysis are listed in table 3.

Analysis and Results

The analysis of the vertical wind estimation techniques was conducted in three parts. The objective of the first part was to determine how well the simple vertical wind models estimate the microburst winds independent of signal noise or measurement error. This objective established the upper performance limit for the vertical wind models. The second part of the analysis focused on the effects of signal noise and the measurement error on the vertical wind estimation. The TASS generated microburst data sets were used as the reference or truth for the first and second parts of the analysis. The third part of the analysis used the flight test measurements from the airborne Doppler radar to compute the vertical winds and to compare with the in situ measurements. The flight test results were then compared with the expected results established in the second part of the analysis.

All the simulation analysis was conducted for altitudes from 100 to 600 m. This range covers altitudes above those for which a forward-look wind shear system would be active. The altitudes above 300 m were included in the analysis for comparison with the results of the preliminary study of reference 3 and to establish the altitude limit of the vertical wind models.

Validity of Vertical Wind Model Assumptions

The two vertical wind models of this study relate the horizontal shear to the vertical wind as a function of altitude. These models share two basic characteristics:

1. Divergent radial winds (positive shear) are associated with downdrafts and conversely, convergent radial winds (negative shear) are associated with updrafts.

2. The magnitude of the vertical wind is proportional to the magnitude of the shear.

An earlier study (ref. 3) established that these two assumptions are reasonable for the simple axisymmetric microburst case presented in figure 1. Although some microbursts are roughly axisymmetric, many are asymmetric. The validity of these assumptions has not been established for asymmetric microbursts. Figure 13 shows where these assumptions are and are not valid for the asymmetric microburst data set of this study. Shown in the figure is the vertical wind at each radar range bin plotted as a function of the radial shear. Also shown in the figure are the two vertical wind model functions. The data points that lie in the lower left and the upper right quadrants of the graphs violate the first of the assumed characteristics. The nonzero data points that lie along the vertical axis violate the second assumed characteristic. Both basic assumptions appear reasonable at the lower altitudes ($z \leq 300$) and for the earliest of the three times. At the later times and the higher altitudes these assumptions break down. There appears to be very little correlation between the radial shear and the vertical wind above 300 m for $t = 51$ min.

Microburst Core Criteria

The vertical wind divergence (which is used in the vertical wind models) can be estimated from the sensor-measured radial wind with equation (10) or (15), depending on whether the estimate is inside or outside the downdraft core. Near the downdraft core, the radial velocity variation is nearly linear for the symmetrical data in figures 5 and 6. Figure 14 shows the vertical wind contours for the asymmetric microburst data at each scan altitude, with the $w = 0$ contour line highlighted in white. The white contour line was considered to outline the downdraft core. On the right side of the figure are the corresponding contour plots of the linear correlation coefficient R of the radial wind profile. The linear correlation coefficient was computed from a moving, 5-point linear least-squares fit of the radial wind profile. The

linear correlation coefficient for range bin i along scan line j was defined as

$$R_{i,j} = \frac{-2u_{s_{i-2,j}} - u_{s_{i-1,j}} + u_{s_{i+1,j}} + 2u_{s_{i+2,j}}}{\sqrt{10 \sum_{k=i-2}^{k=i+2} u_{s_{k,j}}^2 - 2\left(\sum_{k=i-2}^{k=i+2} u_{s_{k,j}}\right)^2}} \quad (32)$$

The value of R varied from -1 to 1 with the magnitude indicating how linear the 5 data points were, a value of 1 or -1 being linear and 0 being nonlinear. The sign of R corresponded to the sign of the slope or shear.

The $w = 0$ contour line was repeated on the R contour plot to evaluate the correlation between a positive linear shear and the downdraft core. As can be seen in figure 14, the region of positive linear shear encompasses most of the downdraft region. Once again, the lower altitudes provided the best results. At the higher scan altitudes, there were small regions of strong downdraft with either nonlinear or negative shears. This condition was assumed to be due to smaller microbursts being generated within the larger one.

The effect of measurement noise is shown in figure 15, which is the same as figure 14 except that the linear correlation coefficient was computed from the simulated radar-measured velocities. The measurement noise and the signal filtering reduce the region of positive linear shear, particularly at the lower altitudes where ground clutter is a major factor.

The correlation between the downdraft core area and the area of positive linear shear was significantly eroded when the effects of noise were included. Lacking any other mechanism to distinguish the downdraft core, $R \geq 0.9$ was selected to represent the microburst core area and $R < 0.9$ the area outside microburst core.

Radar Simulation Results

The vertical wind models were first tested independent of signal noise or measurement error to establish their upper performance limit. The true radial velocities, shown on the left side of figure 12, were used to compute the radial shear. The shear was computed in conjunction with the linear correlation coefficient by using a 5-point linear least-squares fit. The equation for the radial shear (slope of the linear fit) at range bin i along range line j is

$$\left(\frac{\partial u_s}{\partial r_s}\right)_{i,j} = \frac{-2u_{s_{i-2,j}} - u_{s_{i-1,j}} + u_{s_{i+1,j}} + 2u_{s_{i+2,j}}}{10 \, \Delta r_s}$$

$$(33)$$

The vertical divergence $\partial w_m / \partial z_m$ was then computed with equation (10) or (15), depending upon the core criteria established in the previous section. The vertical divergence was then used in either the linear or empirical model to compute the vertical wind for that range bin. The computed vertical winds were constrained between 10 and -20 m/s to preclude unrealistic estimates. A flowchart of the vertical wind calculation process is provided in figure 16.

The vertical wind computed from the two models and the true vertical wind are shown in figure 17. At the lower three scan altitudes, the difference between the two models is small, with both slightly underestimating the magnitude and the spatial extent of the downdraft. At the upper three altitudes, the empirical model produces stronger downdraft estimates than the linear model, which continues to underestimate the magnitude. Neither model replicates the spatial extent of the downdraft at the upper scan altitudes. This is because of the poor correlation between the positive radial shear and the downdraft region at these altitudes.

The error in the vertical wind estimation was defined as the computed value subtracted from the true value. The error was computed at each range bin of the scan for both models. The mean and the standard deviation of the error were then computed for each scan altitude. The results are shown in figure 18 along with the error statistics that result when the vertical wind is neglected (assume $w = 0$, which represents the lower limit of model performance). The statistics confirm the qualitative assessments of figure 17. The mean and the standard deviation of the error increase with altitude. Both models tended to underestimate the downdraft; however, the empirical model did slightly better but often with a larger standard deviation. These results agree with those of reference 3, in which a similar analysis was conducted with the symmetrical microburst data set shown in figure 1.

Vertical wind estimation with measurement error. The second part of the analysis computed the vertical winds with the simulated radar measurements, which included the effects of ground clutter and signal noise. The analysis described in the previous section was repeated by using the simulated radar velocity measurements shown on the right side of figure 12 as input to the vertical wind calculation. The mean and the standard deviation of the simulated radar radial velocity measurement error were computed at each scan altitude to establish the fidelity of input to the vertical wind calculation. Figure 19 shows the mean and the standard deviation of the simulated radial velocity measurement

error. The mean error varied from -2.0 to 2.3 with standard deviation from 2.6 to 6.4 m/s.

The effect of the radar measurement error on the vertical wind estimation can be seen in figure 20, which shows the true vertical wind and the computed vertical wind from the two models at each scan altitude. When compared with figure 17, it can be seen that the performance of the vertical wind models is sensitive to the fidelity of the radar measurement. The magnitude of this sensitivity is presented in figure 21 in terms of the mean and the standard deviation of vertical wind estimation error which includes the effects of radar measurement error. The estimation error results with no radar measurement error, which were presented in figure 18, are also shown to establish the performance limits of the models.

Vertical F-factor error. The effect of the wind measurement error on estimating the vertical component of the hazard was assessed by computing the vertical component of the 1-km averaged F-factor for each range bin. Recall that a 1-km averaged F-factor of 0.1 or greater is considered hazardous. The vertical F-factor F_v was first computed for each range bin and then averaged over seven successive range bins (1050 m) along the scan line to derive the averaged vertical component of the hazard estimate. The equation for the average vertical F-factor at range bin i is

$$\overline{F}_{v_i} = \frac{1}{7} \sum_{k=i}^{k=i+6} F_{v_k} = \frac{-1}{7V} \sum_{k=i}^{k=i+6} w_k \qquad (34)$$

Figure 22 shows the true $\overline{F}_v$ and that computed with the vertical wind estimates derived from the true radial winds (i.e., the vertical winds in fig. 17). The $\overline{F}_v$ contours of figure 22 are very similar to the vertical wind contours of figure 17. The true $\overline{F}_v = 0.05$ contour is highlighted in white to distinguish the area where the vertical contribution is at least half of the hazard alert threshold. Note that the area in which $\overline{F}_v$ exceeds 0.05 can be large, even at the lower altitudes where the vertical wind magnitude is reduced.

Figure 23 shows the $\overline{F}_v$ contours computed with the vertical wind estimates that included measurement error effects (i.e., the vertical winds of fig. 20). As with figure 22, the true $\overline{F}_v = 0.05$ contour is highlighted in white. The difference between the $\overline{F}_v$ contours with and without measurement errors (figs. 23 and 22, respectively) is much less than the difference between the vertical wind contours with and without measurement errors (figs. 20 and 17, respectively).

This difference is due to the filtering effect of averaging the vertical F-factor component.

The $\overline{F}_v$ error was computed in the same manner as the vertical wind error. The mean and the standard deviation of the $\overline{F}_v$ error are shown in figure 24 for each scan altitude. As with the vertical wind errors, shown in figure 21, the $\overline{F}_v$ error increased with altitude. The mean of the $\overline{F}_v$ error, with the measurement error effects, varied from 0.0003 to 0.075, and the standard deviation varied from 0.015 to 0.083. At the altitudes of primary interest for wind shear detection, at or below 300 m, the mean error was between 0.010 and 0.042 with the standard deviation between 0.014 and 0.028.

The improvement in the hazard estimate achieved through the vertical wind estimation models was assessed by computing the percent improvement in the $\overline{F}_v$ estimate. The percent improvement was computed relative to neglecting the vertical wind contribution as follows:

$$\text{Percent improvement} = 100 \times \left(1 - \left|\frac{\text{Error}_{\text{model}}}{\text{Error}_{w=0}}\right|\right) \tag{35}$$

With the above formulation, a 100-percent improvement would correspond to a perfect estimate from the model, and a negative percent improvement would indicate that the model estimate was worse than the neglected vertical contribution. Figure 25 shows percent improvement in the mean error of the two vertical wind models with and without the measurement error effects. Figure 26 shows the corresponding percent improvement of the standard deviation. The effect of the measurement error on the model performance is clearly shown in these figures. The simulated measurement error reduces the percent improvement to about one half of that achieved with perfect radial velocity measurements. The measurement error effect on the standard deviation is much less.

The altitude of maximum performance improvement of the models is about 300 m for both the mean and the standard deviation. Above 300 m, the percent improvement in the mean error gradually diminishes. The percent improvement in the standard deviation is much less and rapidly diminishes at the higher altitudes. At the lower altitudes, the percent improvement in the mean and the standard deviation is minimized by the diminished contribution of the vertical wind.

Total F-factor error. The effect of the vertical wind model errors on the total hazard estimate was determined by repeating the $\overline{F}_v$ analysis for the

1-km $\overline{F}$. The $\dot{u}$ term in the horizontal component of the total F-factor was approximated as

$$\dot{u} \approx \frac{\partial u_s}{\partial r_s} V_g \tag{36}$$

Figure 27 shows the true F and $\overline{F}$ computed with the vertical wind estimates derived without radar measurement errors. The true $\overline{F} = 0.1$ contour is highlighted in white to distinguish the areas exceeding the hazard alert threshold. The $\overline{F}$ contours of figure 27 are basically the same shape as the $\overline{F}_v$ contours of figure 22 with about a 0.05 increase in the magnitude of $\overline{F}$. This increase would indicate that the vertical component of the F-factor significantly contributes to the total F-factor for this simulated microburst with the aircraft at the assumed airspeed of 130 knots. This condition is illustrated in figure 28, which shows the contours of horizontal and vertical components of the true F-factor relative to the total.

Figure 29 shows the true $\overline{F}$ contours and those computed with the vertical wind estimates that included measurement error effects. As with the previous two figures, the true $\overline{F} = 0.1$ contour is highlighted in white to distinguish the hazard threshold. The primary effect of the measurement error on the $\overline{F}$ contours was an increase in the magnitude of the maximum and minimum values. This effect is illustrated by contrasting figure 27, which does not include measurement error effects, with figure 29, which does. This increase in the extremes is due to the compounding effect of the measurement error, which is a factor in the vertical wind estimate. The vertical wind estimation technique acts as an altitude dependent amplifier of the horizontal shear measurement. Consequently, the vertical wind estimate is sensitive to noise in the horizontal shear measurement, and this sensitivity increases with altitude.

The mean and the standard deviation of the $\overline{F}$ error are shown in figure 30 for each scan altitude. The mean $\overline{F}$ error was about the same as the mean $\overline{F}_v$ error. However, because of the compounding effect of the measurement error, the standard deviation of the $\overline{F}$ error was larger. The mean of the $\overline{F}$ error, with the measurement error effects, varied from 0.007 to 0.094, and the standard deviation varied from 0.029 to 0.089. At altitudes at or below 300 m, the mean error was between 0.019 and 0.057, with the standard deviation between 0.029 and 0.049.

Figure 31 shows percent improvement in the mean error of the two vertical wind models, with and without the measurement error effects. The curves for the improvement in the mean error of $\overline{F}$ are similar to those for $\overline{F}_v$ in figure 25. As for $\overline{F}_v$,

the altitude of maximum performance improvement occurs at about 300 m.

Figure 32 shows the corresponding percent improvement of the standard deviation. The percent improvement in the standard deviation of $\overline{F}$ is much less than that of $\overline{F}_v$. The compounding effect of the measurement error is clearly seen. The negative percent improvement values at altitudes above 200 m indicate that the standard deviation was larger than that from neglecting the vertical wind. The difference between the results with and without measurement error indicates that the standard deviation could be improved by reducing the measurement error below 300 m. Errors in the vertical wind models limit the improvement above 300 m.

Flight Test Results

The flight test data analysis consisted of computing $\overline{F}_v$ from the onboard Doppler radar measurement and comparing it with the in situ measurement, which was assumed to be the true value. The vertical wind was computed with both the linear and the empirical models. The results of the flight test data analysis were then compared with the radar simulation results.

The onboard in situ system only measures the F-factor along the flight path of the airplane. Therefore, the radar estimates of $\overline{F}_v$ can only be compared with the in situ at range bins along the flight path. As the airplane approaches a given point along the flight path, the point may have been scanned several times at various ranges from the airplane. This situation leads to a variety of possible methods to compare the radar measurements with the in situ measurements. For this study, a rather simple method was selected whereby the radar measurement at a fixed range directly in front of the airplane was compared with the in situ measurement of that airspace. The range selected was 2 km. This range was close enough to the airplane to minimize the effect of microburst dynamics and airplane maneuvering between the radar and in situ measurements and yet provided sufficient range for the radar signal filtering algorithms to be effective.

The radar measurements at 11 successive range bins were required to compute $\overline{F}_v$ at a given range. Range bin 10 along the 0 azimuth line corresponded to the forward-look point at 2 km, as shown in figure 33. The radar measurements from range bins 5 through 15 were used in the data analysis. The radial shear and corresponding vertical wind estimate were computed with the calculation flowchart provided in figure 16 for range bins 7 through 13. The radar algorithm had one additional calculation not shown on the flowchart. The algorithm computed the residual of the linear least-squares fit for the radial shear. The residual at range bin i was defined as

$$\text{Res}_i = \sqrt{\sum_{k=-2}^{k=2}\left[k\Delta r_s\left(\frac{\partial u_s}{\partial r_s}\right)_i - u_{s_{i+k}} + \frac{1}{5}\sum_{j=i-2}^{j=i+2}u_{s_j}\right]^2} \tag{37}$$

If the residual of the linear fit exceeded the residual threshold of 3.0 m/s, the radial shear was set to 0. This resulted in a vertical wind estimate of 0 for that range bin.

After the radial shear and vertical wind were computed for range bins 7 through 13, the 1-km averaged vertical F-factor for range bin 10 was computed as

$$\overline{F}_{v_{10}} = \frac{-1}{7V}\sum_{k=7}^{k=13}w_k \tag{38}$$

where V was the true airspeed of the airplane at the time of the radar measurement.

To compare the in situ and the radar measurements, the time scale for the radar measurement was shifted by the time required for the airplane to reach the radar measured location. An additional 5-s shift was applied to correct for the lag in the in situ measurement because of its gust rejection filter (ref. 18). The total time shift applied to the radar measurement was

$$\Delta t = \frac{r_{\min} + 9.5\Delta r_s}{V_g} + 5 \tag{39}$$

For the events selected, the minimum radar range ($r_{\min}$) was 781 m and the range bin size Δr_s was 144 m. The ground speed V_g was that of the airplane at the time of the radar measurement.

Figure 34 shows the $\overline{F}_v$ of the in situ measurement and the radar estimate at range bin 10 for the events listed in table 4. Also shown in the figure is the linear correlation coefficient R of the in situ measurement and the radar estimate with the linear and the empirical model. The radar measurements that exceeded the residual threshold over the averaging interval were excluded from the correlation statistics. Under such conditions, radar estimate of $\overline{F}_v$ defaults to zero.

Figure 35 shows a summary, plotted from best to worst, of the correlation coefficients for the events. Also shown in the figure are the maximum, minimum, and average altitudes during the event. The best correlation between the in situ and the radar measurements occurred in event 548. However, this

event had a large percent of the data exceed the residual threshold and therefore provided no estimate of $\overline{F}_v$. Events 438, 463, 464, 553, 555, and 573 all showed consistent correlation results, with values of R ranging from 0.778 to 0.656 with the linear model and 0.753 to 0.647 with the empirical model. The worst results were obtained from events 454, 554, and 556, with a negative correlation for event 454. These events also had the largest variation in altitude throughout the run; this indicates that perhaps the air mass measured by the radar was not the same air mass measured in situ. However, this hypothesis is not conclusive because event 548 yielded good results with an altitude variation only slightly less than event 454.

The estimated $\overline{F}_v$ (excluding values of 0) and the in situ measurement for all the selected events are shown in figure 36. Also shown in the figure are the lines of perfect agreement and of the standard deviation of 1 and -1 about the average error. The average error for the linear and empirical models was 0.0001 and -0.0007, with standard deviations of 0.0087 and 0.0093, respectively. The standard deviation lines shown on the figure are the maximum of the two models. The correlation coefficient for the linear and the empirical model was 0.561 and 0.557, respectively. If the events in which the altitude variation exceeded 200 m (events 454, 548, 554, and 556) are excluded, then the correlation coefficient for the linear and the empirical model improves to 0.659 and 0.648, respectively. The corresponding average error for the linear and the empirical models is -0.0007 and -0.0017, with a standard deviation of 0.0077 and 0.0083, respectively.

Comparison of Simulation and Flight Test Results

Table 4 lists the mean and the standard deviation of the $\overline{F}_v$ errors from the flight test and the radar simulation at 300 m. The errors from the flight test were much less than predicted from the simulation, which could be due to a number of differences between the simulation and the flight test. The simulated ground clutter environment may have been more severe than the clutter experienced in the flight test. The simulation errors were computed across the radar scan for a single microburst model at three different times. The flight test errors were computed at a single range bin for a variety of microbursts events. The microburst model used in the simulation produced a maximum $\overline{F}_v$ value of approximately 0.20, which was 4 times larger than any of the flight test events. This larger $\overline{F}_v$ resulted in the potential for much larger errors in the simulation. The values of

$\overline{F}_v$ of the simulation were larger in part because the airspeed of the simulation (130 knots) was less than the flight test (210 to 230 knots). Recall from equation (4) that the vertical F-factor is inversely proportional to the airspeed. For the same downdraft, an airplane traveling at 130 knots would experience a vertical F-factor 1.7 times greater than an airplane flying at 220 knots. The bottom row of table 4 lists the $\overline{F}_v$ errors from the flight test corrected from 220 to 130 knots. The airspeed corrected results were still less than the radar simulation.

Concluding Remarks

The objective of this study was to assess the ability of simple vertical wind models to improve the hazard prediction capability of an airborne Doppler sensor in a realistic microburst environment. The results indicate that, in the altitude region of interest (at or below 300 m), both the linear and the empirical vertical wind models improved the hazard estimate. The radar simulation study showed that the magnitude of the performance improvement was altitude dependent. The altitude of maximum performance improvement occurred at about 300 m. At lower altitudes, the percent improvement was minimized by the diminished contribution of the vertical wind. The performance difference between the two models was small.

The results of the radar simulation study showed that the measurement error due to signal noise and clutter can significantly degrade the wind shear hazard prediction. The radar measurement errors not only degrade the horizontal shear hazard prediction but also propagate the errors to the vertical hazard estimate. These errors can reduce the percent improvement of the vertical hazard estimate to about half of that achieved with perfect radial velocity measurements.

The vertical hazard estimate errors from flight tests were less than the radar simulation results. This difference may be due to the lower magnitude of the flight test events relative to the microburst data sets used in the radar simulation or to an overly conservative simulation of the radar measurement error.

The vertical hazard estimate could be significantly improved by reducing its sensitivity to the radar measurement error. This study was limited to processing a single radar scan to estimate the vertical wind. Methods of processing multiple radar scans at different elevation angles may reduce the measurement error sensitivity and improve the vertical hazard estimate.

Appendix

Transformation Equations

The following transformation equations relate the microburst-referenced velocities defined in a cylindrical coordinate system to the forward-look airborne sensor-measured velocities defined in a spherical coordinate system, as shown in figure 4.

The microburst velocities ($u_m, v_m,$ and w_m) can be transformed to sensor-referenced velocities ($u_s, v_s,$ and w_s) through

$$\begin{pmatrix} u_s \\ v_s \\ w_s \end{pmatrix} = \begin{pmatrix} \cos\phi_s & 0 & \sin\phi_s \\ 0 & 1 & 0 \\ -\sin\phi_s & 0 & \cos\phi_s \end{pmatrix} \begin{pmatrix} \cos\theta_s & \sin\theta_s & 0 \\ -\sin\theta_s & \cos\theta_s & 0 \\ 0 & 0 & 1 \end{pmatrix} \left[\begin{pmatrix} \cos\theta_m & -\sin\theta_m & 0 \\ \sin\theta_m & \cos\theta_m & 0 \\ 0 & 0 & 1 \end{pmatrix} \begin{pmatrix} u_m \\ v_m \\ w_m \end{pmatrix} + \begin{pmatrix} u_\infty \cos\theta_\infty \\ u_\infty \sin\theta_\infty \\ 0 \end{pmatrix} \right] \tag{A1}$$

or, in matrix form,

$$\mathbf{U}_s = \mathbf{T}_{\phi_s}\mathbf{T}_{\theta_s}(\mathbf{T}_{\theta_m}\mathbf{U}_m + \mathbf{U}_\infty) \tag{A2}$$

Conversely, the sensor velocities can be expressed in terms of the microburst velocities as

$$\mathbf{U}_m = \mathbf{T}_{\theta_m}^{-1}(\mathbf{T}_{\theta_s}^{-1}\mathbf{T}_{\phi_s}^{-1}\mathbf{U}_s - \mathbf{U}_\infty) \tag{A3}$$

The spatial derivatives of the sensor velocities, which are used in the F-factor calculation, can be derived from equation (A2) as

$$\frac{\partial\mathbf{U}_s}{\partial r_s} = \mathbf{T}_{\phi_s}\mathbf{T}_{\theta_s}\left(\frac{\partial\mathbf{T}_{\theta_m}}{\partial r_s}\mathbf{U}_m + \mathbf{T}_{\theta_m}\frac{\partial\mathbf{U}_m}{\partial r_s}\right) \tag{A4}$$

$$\frac{\partial\mathbf{U}_s}{\partial\phi_s} = \frac{\partial\mathbf{T}_{\phi_s}}{\partial\phi_s}\mathbf{T}_{\theta_s}(\mathbf{T}_{\theta_m}\mathbf{U}_m + \mathbf{U}_\infty) + \mathbf{T}_{\phi_s}\mathbf{T}_{\theta_s}\left(\frac{\partial\mathbf{T}_{\theta_m}}{\partial\phi_s}\mathbf{U}_m + \mathbf{T}_{\theta_m}\frac{\partial\mathbf{U}_m}{\partial\phi_s}\right) \tag{A5}$$

$$\frac{\partial\mathbf{U}_s}{\partial\theta_s} = \mathbf{T}_{\phi_s}\frac{\partial\mathbf{T}_{\theta_s}}{\partial\theta_s}(\mathbf{T}_{\theta_m}\mathbf{U}_m + \mathbf{U}_\infty) + \mathbf{T}_{\phi_s}\mathbf{T}_{\theta_s}\left(\frac{\partial\mathbf{T}_{\theta_m}}{\partial\theta_s}\mathbf{U}_m + \mathbf{T}_{\theta_m}\frac{\partial\mathbf{U}_m}{\partial\theta_s}\right) \tag{A6}$$

Equations (A4), (A5), and (A6) can be expanded by using the following geometric relationships and their spatial derivatives:

$$r_m = \sqrt{(r_s\cos\phi_s\cos\theta_s - r_c\cos\phi_s\cos\theta_c)^2 + (r_s\cos\phi_s\sin\theta_s - r_c\cos\phi_s\sin\theta_c)^2} \tag{A7}$$

$$\cos\theta_m = \frac{r_s\cos\phi_s\cos\theta_s - r_c\cos\phi_s\cos\theta_c}{r_m} \tag{A8}$$

$$\sin\theta_m = \frac{r_s\cos\phi_s\sin\theta_s - r_c\cos\phi_s\sin\theta_c}{r_m} \tag{A9}$$

$$z_m = r_s\sin\phi_s + z_s \tag{A10}$$

The partial derivatives with respect to the sensor radius r_s are

$$\frac{\partial r_m}{\partial r_s} = \cos\phi_s\cos(\theta_m - \theta_s) \tag{A11}$$

$$\frac{\partial\theta_m}{\partial r_s} = \frac{\cos\phi_s}{r_m}\sin(\theta_s - \theta_m) \tag{A12}$$

$$\frac{\partial z_m}{\partial r_s} = \sin\phi_s \tag{A13}$$

13

$$\frac{\partial \mathbf{T}_{\theta_m}}{\partial r_s} = \frac{\partial \theta_m}{\partial r_s}\frac{\partial \mathbf{T}_{\theta_m}}{\partial \theta_m}\frac{\cos\phi_s}{r_m}\sin(\theta_s - \theta_m)\begin{pmatrix} -\sin\theta_m & -\cos\theta_m & 0 \\ \cos\theta_m & -\sin\theta_m & 0 \\ 0 & 0 & 0 \end{pmatrix} \tag{A14}$$

$$\frac{\partial \mathbf{U}_m}{\partial r_s} = \frac{\partial r_m}{\partial r_s}\frac{\partial \mathbf{U}_m}{\partial r_m} + \frac{\partial \theta_m}{\partial r_s}\frac{\partial \mathbf{U}_m}{\partial \theta_m} + \frac{\partial z_m}{\partial r_s}\frac{\partial \mathbf{U}_m}{\partial z_m} \tag{A15}$$

The partial derivatives with respect to the sensor azimuth θ_s are

$$\frac{\partial r_m}{\partial \theta_s} = \cos\phi_s\sin(\theta_m - \theta_s) \tag{A16}$$

$$\frac{\partial \theta_m}{\partial \theta_s} = \frac{r_s\cos\phi_s}{r_m}\cos(\theta_m - \theta_s) \tag{A17}$$

$$\frac{\partial z_m}{\partial \theta_s} = 0 \tag{A18}$$

$$\frac{\partial \mathbf{T}_{\theta_m}}{\partial \theta_s} = \frac{\partial \theta_m}{\partial \theta_s}\frac{\partial \mathbf{T}_{\theta_m}}{\partial \theta_m}\frac{r_s\cos\phi_s}{r_m}\cos(\theta_m - \theta_s)\begin{pmatrix} -\sin\theta_m & -\cos\theta_m & 0 \\ \cos\theta_m & -\sin\theta_m & 0 \\ 0 & 0 & 0 \end{pmatrix} \tag{A19}$$

$$\frac{\partial \mathbf{T}_{\theta_s}}{\partial \theta_s} = \begin{pmatrix} -\sin\theta_s & \cos\theta_s & 0 \\ -\cos\theta_s & -\sin\theta_s & 0 \\ 0 & 0 & 0 \end{pmatrix} \tag{A20}$$

$$\frac{\partial \mathbf{U}_m}{\partial \theta_s} = \frac{\partial r_m}{\partial \theta_s}\frac{\partial \mathbf{U}_m}{\partial r_m} + \frac{\partial \theta_m}{\partial \theta_s}\frac{\partial \mathbf{U}_m}{\partial \theta_m} + \frac{\partial z_m}{\partial \theta_s}\frac{\partial \mathbf{U}_m}{\partial z_m} \tag{A21}$$

The partial derivatives with respect to the sensor elevation ϕ_s are

$$\frac{\partial r_m}{\partial \phi_s} = -r_m\tan\phi_s \tag{A22}$$

$$\frac{\partial \theta_m}{\partial \phi_s} = 0 \tag{A23}$$

$$\frac{\partial z_m}{\partial \phi_s} = r_s\cos\phi_s \tag{A24}$$

$$\frac{\partial \mathbf{T}_{\theta_m}}{\partial \phi_s} = \frac{\partial \theta_m}{\partial \phi_s}\frac{\partial \mathbf{T}_{\theta_m}}{\partial \theta_m} = 0 \tag{A25}$$

$$\frac{\partial \mathbf{T}_{\phi_s}}{\partial \phi_s} = \begin{pmatrix} -\sin\phi_s & 0 & \cos\phi_s \\ 0 & 0 & 0 \\ -\cos\phi_s & 0 & -\sin\phi_s \end{pmatrix} \tag{A26}$$

$$\frac{\partial \mathbf{U}_m}{\partial \phi_s} = \frac{\partial r_m}{\partial \phi_s}\frac{\partial \mathbf{U}_m}{\partial r_m} + \frac{\partial \theta_m}{\partial \phi_s}\frac{\partial \mathbf{U}_m}{\partial \theta_m} + \frac{\partial z_m}{\partial \phi_s}\frac{\partial \mathbf{U}_m}{\partial z_m} \tag{A27}$$

Simplifying Assumptions

The transformation equations are simplified by assuming the microburst is symmetrical about the vertical axis with no rotational velocity; therefore,

$$\frac{\partial \mathbf{U}_m}{\partial \theta_m} = 0 \tag{A28}$$

and

$$v_m = 0 \tag{A29}$$

Spatial Velocity Gradient Equations

Under the assumptions stated above, the spatial velocity derivatives in the microburst-centered coordinate system can be transformed to the sensor coordinate system as

$$\frac{\partial u_s}{\partial r_s} = \left[\frac{\partial u_m}{\partial r_m} \cos^2(\theta_m - \theta_s) + \frac{u_m}{r_m} \sin^2(\theta_m - \theta_s) \right] \cos^2 \phi_s$$

$$+ \left(\frac{\partial u_m}{\partial z_m} + \frac{\partial w_m}{\partial r_m} \right) \cos(\theta_m - \theta_s) \cos \phi_s \sin \phi_s + \frac{\partial w_m}{\partial z_m} \sin^2 \phi_s \tag{A30}$$

$$\frac{\partial v_s}{\partial r_s} = \left(\frac{\partial u_m}{\partial r_m} - \frac{u_m}{r_m} \right) \cos(\theta_m - \theta_s) \sin(\theta_m - \theta_s) \cos \phi_s + \frac{\partial u_m}{\partial z_m} \sin(\theta_m - \theta_s) \sin \phi_s \tag{A31}$$

$$\frac{\partial w_s}{\partial r_s} = \frac{\partial w_m}{\partial r_m} \cos(\theta_m - \theta_s) \cos^2 \phi_s - \frac{\partial u_m}{\partial z_m} \cos(\theta_m - \theta_s) \sin^2 \phi_s$$

$$- \left[\frac{\partial u_m}{\partial r_m} \cos^2(\theta_m - \theta_s) + \frac{u_m}{r_m} \sin^2(\theta_m - \theta_s) + \frac{\partial w_m}{\partial z_m} \right] \cos \phi_s \sin \phi_s \tag{A32}$$

$$\frac{\partial u_s}{\partial \theta_s} = \cos \phi_s \left\{ u_m \sin(\theta_m - \theta_s) + u_\infty \sin(\theta_\infty - \theta_s) \right.$$

$$\left. + r_s \sin(\theta_m - \theta_s) \left[\sin \phi_s \frac{\partial w_m}{\partial r_m} + \cos \phi_s \cos(\theta_m - \theta_s) \left(\frac{\partial u_m}{\partial r_m} - \frac{u_m}{r_m} \right) \right] \right\} \tag{A33}$$

$$\frac{\partial u_s}{\partial \phi_s} = \cos \phi_s \left[\left(r_s \cos \phi_s \frac{\partial u_m}{\partial z_m} - r_m \tan \phi_s \frac{\partial u_m}{\partial r_m} \right) \cos(\theta_m - \theta_s) + w_m \right]$$

$$+ \sin \phi_s \left[r_s \cos \phi_s \frac{\partial w_m}{\partial z_m} - r_m \tan \phi_s \frac{\partial w_m}{\partial r_m} - u_m \cos(\theta_m - \theta_s) - u_\infty \cos(\theta_\infty - \theta_s) \right] \tag{A34}$$

$$\frac{\partial v_s}{\partial \phi_s} = \sin(\theta_m - \theta_s) \left(r_s \cos \phi_s \frac{\partial u_m}{\partial z_m} - r_m \tan \phi_s \frac{\partial u_m}{\partial r_m} \right) \tag{A35}$$

$$\frac{\partial w_s}{\partial \phi_s} = - \sin \phi_s \left[\left(r_s \cos \phi_s \frac{\partial u_m}{\partial z_m} - r_m \tan \phi_s \frac{\partial u_m}{\partial r_m} \right) \cos(\theta_m - \theta_s) + w_m \right]$$

$$+ \sin \phi_s \left[r_s \cos \phi_s \frac{\partial w_m}{\partial z_m} - r_m \tan \phi_s \frac{\partial w_m}{\partial r_m} - u_m \cos(\theta_m - \theta_s) - u_\infty \cos(\theta_\infty - \theta_s) \right] \tag{A36}$$

Small Angle Approximation for ϕ_s

If ϕ_s is assumed to be small ($\phi_s < 1$), then $\cos \phi_s \approx 1, \sin \phi_s \approx \phi_s$, and $\sin^2 \phi_s \approx 0$; therefore,

$$\frac{\partial u_s}{\partial r_s} = \frac{\partial u_m}{\partial r_m} \cos^2(\theta_m - \theta_s) + \frac{u_m}{r_m} \sin^2(\theta_m - \theta_s) + \phi_s \left(\frac{\partial u_m}{\partial z_m} + \frac{\partial w_m}{\partial r_m} \right) \cos(\theta_m - \theta_s) \tag{A37}$$

$$\frac{\partial v_s}{\partial r_s} = \left(\frac{\partial u_m}{\partial r_m} - \frac{u_m}{r_m} \right) \cos(\theta_m - \theta_s) \sin(\theta_m - \theta_s) + \phi_s \frac{\partial u_m}{\partial z_m} \sin(\theta_m - \theta_s) \tag{A38}$$

15

$$\frac{\partial w_s}{\partial r_s} = \frac{\partial w_m}{\partial r_m} \cos(\theta_m - \theta_s) - \phi_s \left[\frac{\partial u_m}{\partial r_m} \cos^2(\theta_m - \theta_s) + \frac{u_m}{r_m} \sin^2(\theta_m - \theta_s) + \frac{\partial w_m}{\partial z_m} \right] \qquad (A39)$$

$$\frac{\partial u_s}{\partial \theta_s} = r_s \sin(\theta_m - \theta_s) \cos(\theta_m - \theta_s) \left(\frac{\partial u_m}{\partial r_m} - \frac{u_m}{r_m} \right)$$

$$+ u_m \sin(\theta_m - \theta_s) + u_\infty \sin(\theta_\infty - \theta_s) + \phi_s r_s \frac{\partial w_m}{\partial r_m} \sin(\theta_m - \theta_s) \qquad (A40)$$

$$\frac{\partial v_s}{\partial \theta_s} = r_s \left[\frac{\partial u_m}{\partial r_m} \sin^2(\theta_m - \theta_s) + \frac{u_m}{r_m} \cos^2(\theta_m - \theta_s) \right] - u_m \cos(\theta_m - \theta_s) - u_\infty \cos(\theta_\infty - \theta_s) \qquad (A41)$$

$$\frac{\partial w_s}{\partial \theta_s} = r_s \frac{\partial w_m}{\partial r_m} \sin(\theta_m - \theta_s) - \phi_s \left[r_s \left(\frac{\partial u_m}{\partial r_m} - \frac{u_m}{r_m} \right) \sin(\theta_m - \theta_s) \cos(\theta_m - \theta_s) + u_m \sin(\theta_m - \theta_s) + u_\infty \sin(\theta_\infty - \theta_s) \right] \qquad (A42)$$

$$\frac{\partial u_s}{\partial \phi_s} = r_s \frac{\partial u_m}{\partial z_m} \cos(\theta_m - \theta_s) + w_m - \phi_s \left[r_m \frac{\partial u_m}{\partial r_m} \cos(\theta_m - \theta_s) - r_s \frac{\partial w_m}{\partial z_m} + u_m \cos(\theta_m - \theta_s) + u_\infty \cos(\theta_\infty - \theta_s) \right] \qquad (A43)$$

$$\frac{\partial v_s}{\partial \phi_s} = \left(r_s \frac{\partial u_m}{\partial z_m} - \phi_s r_m \frac{\partial u_m}{\partial r_m} \right) \sin(\theta_m - \theta_s) \qquad (A44)$$

$$\frac{\partial w_s}{\partial \phi_s} = r_s \frac{\partial w_m}{\partial z_m} - u_m \cos(\theta_m - \theta_s) - u_\infty \cos(\theta_\infty - \theta_s) - \phi_s \left[w_m + r_s \frac{\partial u_m}{\partial z_m} \cos(\theta_m - \theta_s) + r_m \frac{\partial u_m}{\partial r_m} \right] \qquad (A45)$$

Small Angle Approximation for $\phi_s = 0$

If $\phi_s = 0$, then

$$\frac{\partial u_s}{\partial r_s} = \frac{\partial u_m}{\partial r_m} \cos^2(\theta_m - \theta_s) + \frac{u_m}{r_m} \sin^2(\theta_m - \theta_s) \qquad (A46)$$

$$\frac{\partial v_s}{\partial r_s} = \left(\frac{\partial u_m}{\partial r_m} - \frac{u_m}{r_m} \right) \cos(\theta_m - \theta_s) \sin(\theta_m - \theta_s) \qquad (A47)$$

$$\frac{\partial w_s}{\partial r_s} = \frac{\partial w_m}{\partial r_m} \cos(\theta_m - \theta_s) \qquad (A48)$$

$$\frac{\partial u_s}{\partial \theta_s} = r_s \left(\frac{\partial u_m}{\partial r_m} - \frac{u_m}{r_m} \right) \sin(\theta_m - \theta_s) \cos(\theta_m - \theta_s) + u_m \sin(\theta_m - \theta_s) + u_\infty \sin(\theta_\infty - \theta_s) \qquad (A49)$$

$$\frac{\partial v_s}{\partial \theta_s} = r_s \left[\frac{\partial u_m}{\partial r_m} \sin^2(\theta_m - \theta_s) + \frac{u_m}{r_m} \cos^2(\theta_m - \theta_s) \right] - u_m \cos(\theta_m - \theta_s) - u_\infty \cos(\theta_\infty - \theta_s) \qquad (A50)$$

$$\frac{\partial w_s}{\partial \theta_s} = r_s \frac{\partial w_m}{\partial r_m} \sin(\theta_m - \theta_s) \qquad (A51)$$

$$\frac{\partial u_s}{\partial \phi_s} = r_s \frac{\partial u_m}{\partial z_m} \cos(\theta_m - \theta_s) + w_m \qquad (A52)$$

$$\frac{\partial v_s}{\partial \phi_s} = r_s \frac{\partial u_m}{\partial z_m} \sin(\theta_m - \theta_s) \qquad (A53)$$

$$\frac{\partial w_s}{\partial \phi_s} = r_s \frac{\partial w_m}{\partial z_m} - u_m \cos(\theta_m - \theta_s) - u_\infty \cos(\theta_\infty - \theta_s) \qquad (A54)$$

16

References

1. National Research Council: *Low-Altitude Wind Shear and Its Hazard to Aviation.* National Academy Press, 1983.

2. Fujita, T. Theodore: *The Downburst—Microburst and Macroburst.* SMRP-RP-210, Univ. of Chicago, 1985. (Available from NTIS as PB85 148 880.)

3. Vicroy, Dan D.: Assessment of Microburst Models for Downdraft Estimation. *J. Aircr.,* vol. 29, no. 6, Nov.-Dec. 1992, pp. 1043-1048.

4. Bowles, Roland L.: Reducing Windshear Risk Through Airborne Systems Technology. *Proceedings of the 17th Congress of the International Council of the Aeronautical Sciences,* 1990, pp. 1603-1630.

5. Proctor, F. H.: *The Terminal Area Simulation System—Volume I: Theoretical Formulation.* NASA CR-4046, DOT/FAA/PM-86/50, I, 1987.

6. Proctor, F. H.: *The Terminal Area Simulation System—Volume II: Verification Cases.* NASA CR-4047, DOT/FAA/PM-86/50, II, 1987.

7. Proctor, F. H.; and Bowles, R. L.: Three-Dimensional Simulation of the Denver 11 July 1988 Microburst-Producing Storm. *Meteorol. Atmos. Phys.,* vol. 49, 1992, pp. 107-124.

8. Switzer, G. F.; Proctor, F. H.; Hinton, D. A.; and Aanstoos, J. V.: *Windshear Database for Forward-Looking Systems Certification.* NASA TM-109012, 1993.

9. Proctor, Fred H.: Numerical Simulation of the 2 August 1985 DFW Microburst With the Three-Dimensional Terminal Area Simulation System. *Proceedings of the 15th Conference on Severe Local Storms,* American Meteorol. Soc., Feb. 1988, pp. J99-J102.

10. Oseguera, Rosa M.; and Bowles, Roland L.: *A Simple, Analytic 3-Dimensional Downburst Model Based on Boundary Layer Stagnation Flow.* NASA TM-100632, 1988.

11. Vicroy, Dan D.: *A Simple, Analytical, Axisymmetric Microburst Model for Downdraft Estimation.* NASA TM-104053, DOT/FAA/RD-91/10, 1991.

12. Britt, C. L.: *User Guide for an Airborne Windshear Doppler Radar Simulation (AWDRS) Program.* NASA CR-182025, DOT/FAA/DS-90/7, 1990.

13. Lewis, Michael S.; Yenni, Kenneth R.; Verstynen, Harry A.; and Person, Lee H.: Design and Conduct of a Windshear Detection Flight Experiment. AIAA-92-4092, Aug. 1992.

14. Adamson, Pat: Status of Turbulence Prediction System's AWAS III. *Airborne Wind Shear Detection and Warning Systems—Third Combined Manufacturers' and Technologists' Conference,* Dan D. Vicroy and Roland L. Bowles, compilers, NASA CP-10060, Part 2, DOT/FAA/RD-91/2-II, 1991, pp. 609-613.

15. Robinson, Paul A.; Bowles, Roland L.; and Targ, Russell: The Detection and Measurement of Microburst Wind Shear by an Airborne Lidar System. Paper presented at the International Conference on Lasers '92 (Houston, Texas), Dec. 1992.

16. Blume, Hans-J. C.; Lytle, C. D.; Jones, W. R.; Bracalente, E. M.; and Britt, C. L.: Airborne Doppler Radar Flight Experiment for the Detection of Microbursts. *High Resolution Air and Spaceborne Radar,* AGARD-CP-459, Oct. 1989, pp. 14-32. (Available from DTIC as AD-A218 658.)

17. Harrah, S. D.; Bracalente, E. M.; Schaffner, P. R.; and Britt, C. L.: NASA's Airborne Doppler Radar for Detection of Hazardous Wind Shear: Development and Flight Testing. AIAA-93-3946, Aug. 1993.

18. Oseguera, Rosa M.; Bowles, Roland L.; and Robinson, Paul A.: Airborne In Situ Computation of the Wind Shear Hazard Index. AIAA-92-0291, 1992.

Table 1. Input Data for Airborne Windshear Doppler Radar Simulation Program

Simulation parameters:

Aircraft distance to touchdown, km	Variable[a]
Aircraft velocity, knots	130
Glide slope angle, deg	3
Number of complete scans	6
Time between scans, sec	3
Roll attitude, deg	0
Pitch attitude, deg	0
Yaw attitude, deg	0
Azimuth integration range/2, deg	5.0
Azimuth integration increment, deg	0.2
Elevator integration range/2, deg	5.0
Elevator integration increment, deg	0.2
Range integration increment, m	100
Random number seed (0-1)	0.224
Runway number	26
Right (1) or left (2)	2

Microburst and clutter:

Microburst type (1 = 3D, 0 = 2D)	1
Rotation of 3D microburst, deg	−90
Along track offset from touchdown, km	Variable[a]
Cross track offset from touchdown, km	0.4
Rain standard deviation, m/s	1
Clutter standard deviation, m/s	0.5
Clutter calculation flag (1 = ON, 0 = OFF)	1
Discrete calculation flag (1 = ON, 0 = OFF)	1
Reflectivity calculation threshold, dBZ	−14
Minimum reflectivity, dBZ	−15
Attenuation code (0, 1, 2)	2

Radar parameters:

Initial radar range, km	0.425
Number of range cells	30
Antenna azimuth—if no scan, deg	0
Total number of scan lines (odd number)	15
Azimuth scan increment, deg	3
Antenna elevation, deg	3
Autotilt range, km	Variable[a]
Autotilt maximum elevator, deg	5
Autotilt minimum elevator, deg	−1
Transmitted power, W	200
Frequency, GHz	9.3
Pulse width, μs	1
Pulse interval, μs	268.6
Receiver noise figure, dB	4
Receiver losses, dB	3
Antenna type	3

[a]Values shown in table 2.

18

Antenna radius, m 0.3048
Aperture taper parameter 0.316
Root-mean-square transmitter phase jitter, deg 0.2
Root-mean-square transmitter frequency jitter, Hz 0

Signal processing:
   Number of pulses 128
   Number of analog-to-digital bits 12
   Auto gain control gain factor 0.6
   Processing threshold, dB 4
   Clutter filter code (-2 to N) 2
   Clutter filter cutoff, m/s 3
   Number of bins for F-factor average 7
   Threshold for F-factor algorithm 0.4
   Model order autoregressive 5

Data products:
   Alarm program data code 1
   Comma separated values plot output code 1
   Inphase quadrature phase data output code 0
   Autoregressive coefficient code 0
   Autoregressive spectra data code 0
   Fourier spectra data code 0
   Start scan number 1
   Finish scan number 6
   Start line number 7
   Finish line number 7

Table 2. Input Data Variables for Airborne Windshear Doppler Radar Simulation Program

Variable	Input data for simulation at—					
	100 m	200 m	300 m	400 m	500 m	600 m
Aircraft distance to touchdown, km	2.309	4.217	6.125	8.033	9.941	11.849
Microburst along track offset from touchdown, km	2.892	0.984	−0.924	−2.832	−4.741	−6.649
Autotilt range, km	8	8	0	0	0	0
Elevation angle above horizon, deg	1.185	0.470	0	0	0	0

Table 3. Microburst Events Used in Flight Test Data Analysis

Event number	Location	Radar reflectivity, dBZ	Altitude, m			In situ $\overline{F}$		In situ $\overline{F}_v$	
			Maximum	Average	Minimum	Maximum	Minimum	Maximum	Minimum
438	Denver	20–25	411.2	296.0	243.4	0.1167	−0.1014	0.0388	−0.0192
454	Denver	10–20	559.8	358.8	269.1	0.0980	−0.1319	0.0229	−0.0210
463	Denver	15–25	395.0	285.2	248.8	0.0881	−0.0511	0.0175	−0.0091
464	Denver	15–25	453.9	323.1	257.0	0.1313	−0.0584	0.0311	−0.0119
548	Orlando	35–45	498.3	328.9	252.9	0.1448	−0.0807	0.0315	−0.0195
553	Orlando	45–50	377.5	290.2	235.1	0.1470	−0.0946	0.0504	−0.0094
554	Orlando	30–45	478.3	294.3	224.2	0.1269	−0.0321	0.0252	−0.0130
555	Orlando	35–40	439.9	299.4	240.2	0.1318	−0.0623	0.0234	−0.0117
556	Orlando	40–45	537.9	340.7	232.4	0.0933	−0.0687	0.0133	−0.0206
573	Orlando	25–35	391.9	279.9	222.3	0.1202	−0.0804	0.0167	−0.0134

Table 4. Averaged $\overline{F}_v$ Errors From Flight Test and Radar Simulation Results at 300-m Altitude

Test	Averaged $\overline{F}_v$ errors for—			
	Linear model		Empirical model	
	Mean	Standard deviation	Mean	Standard deviation
Simulation at—				
300 m, $t = 49$ min	0.0188	0.0218	0.0100	0.0274
300 m, $t = 50$ min	0.0313	0.0255	0.0196	0.0285
300 m, $t = 51$ min	0.0415	0.0251	0.0326	0.0244
Flight	0.0001	0.0087	−0.0007	0.0093
Flight corrected to 130 knots	0.0002	0.0147	−0.0012	0.0157
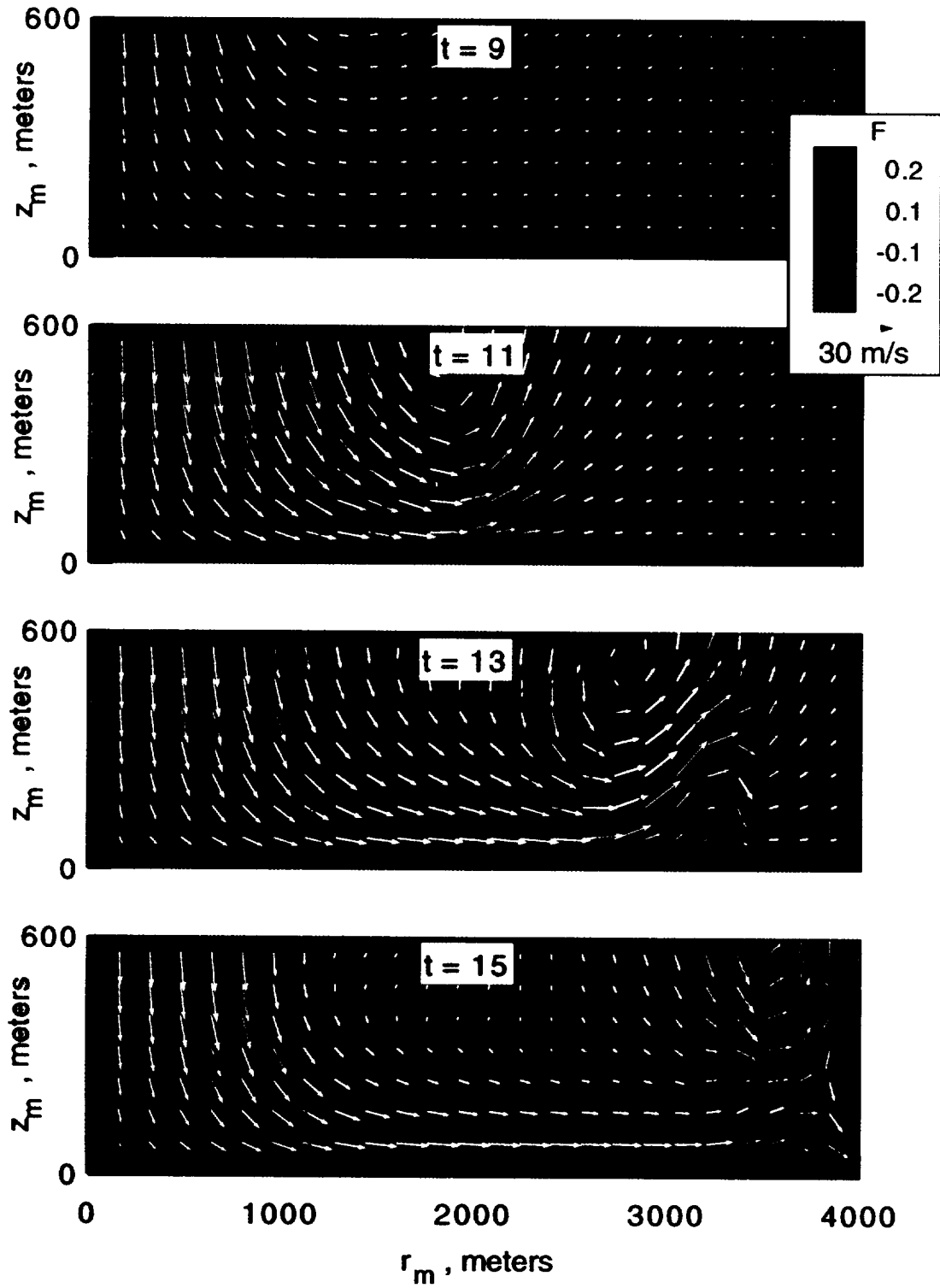
Figure 1. Wind vectors and F-factor contours of axisymmetric microburst simulation at four times.
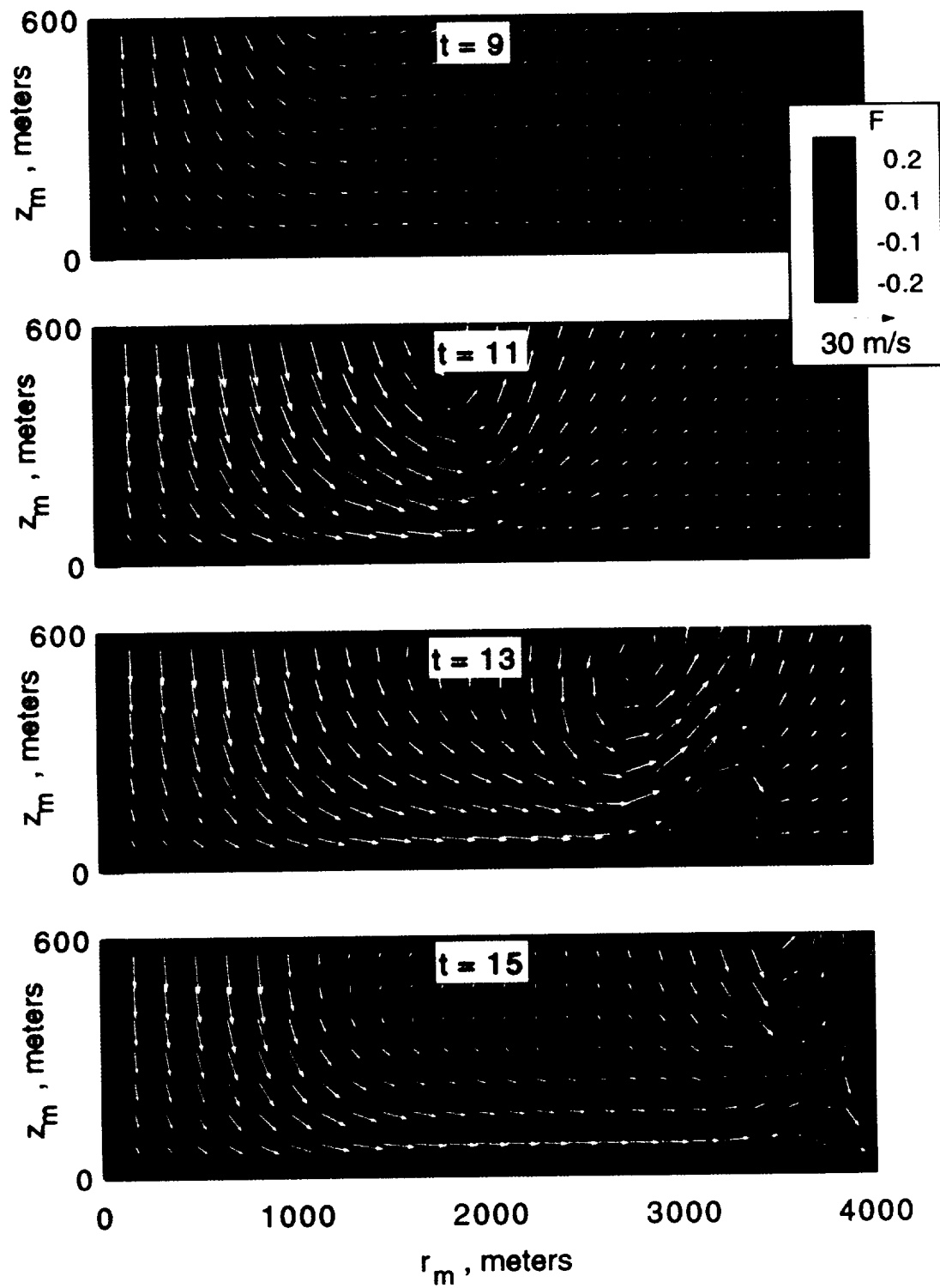
Figure 2. *F*-factor contours computed without vertical winds.

z = 283 meters

y, meters

10 m/s

y = 0

z, meters

x, meters
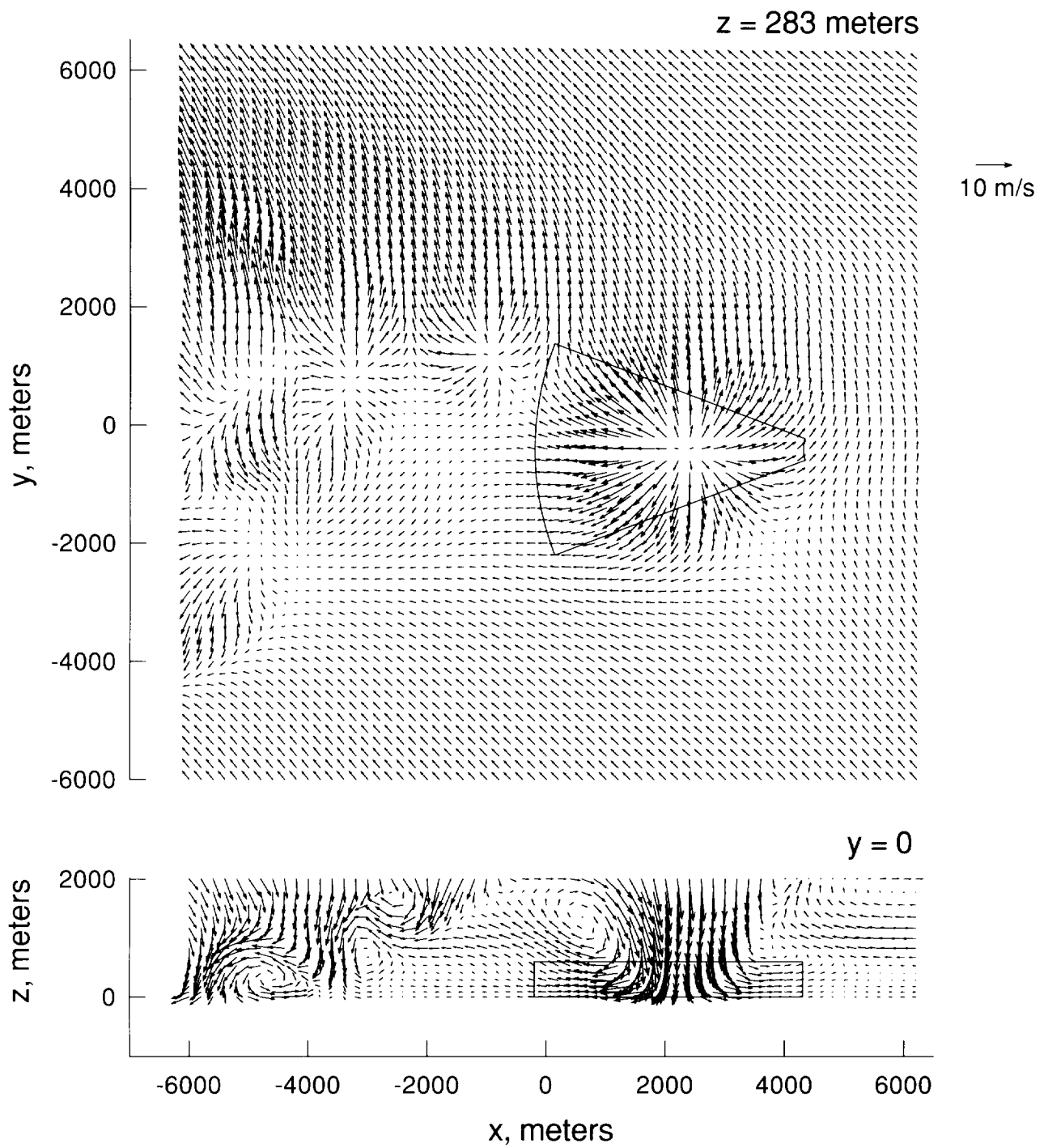
(a) $t = 49$ min.

Figure 3. Horizontal and vertical cross sections of wind vector field with radar scan area outlined.

z = 283 meters

→
10 m/s

y = 0

x, meters
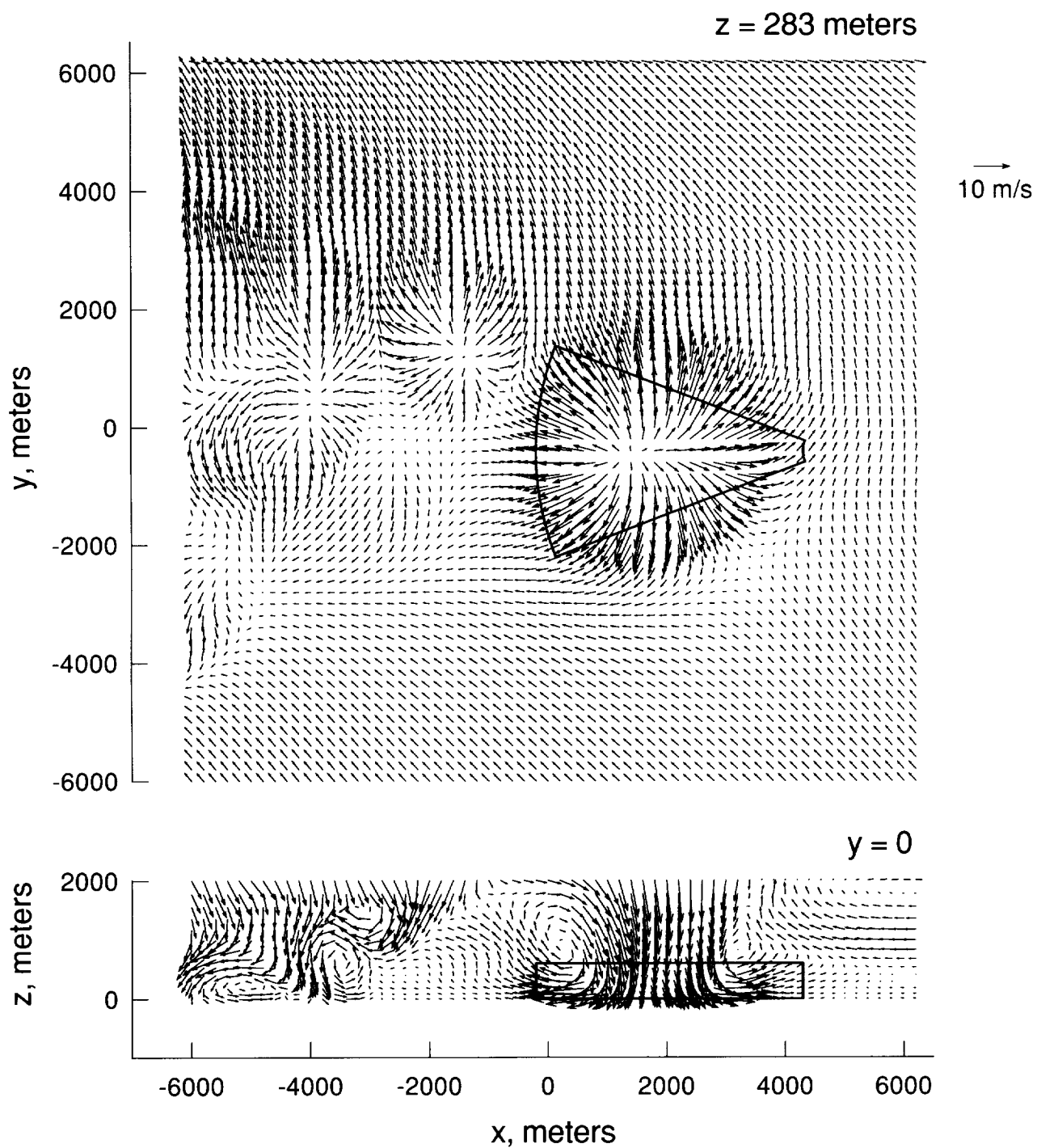
(b) $t = 50$ min.

Figure 3. Continued.

24

z = 283 meters

10 m/s

y = 0
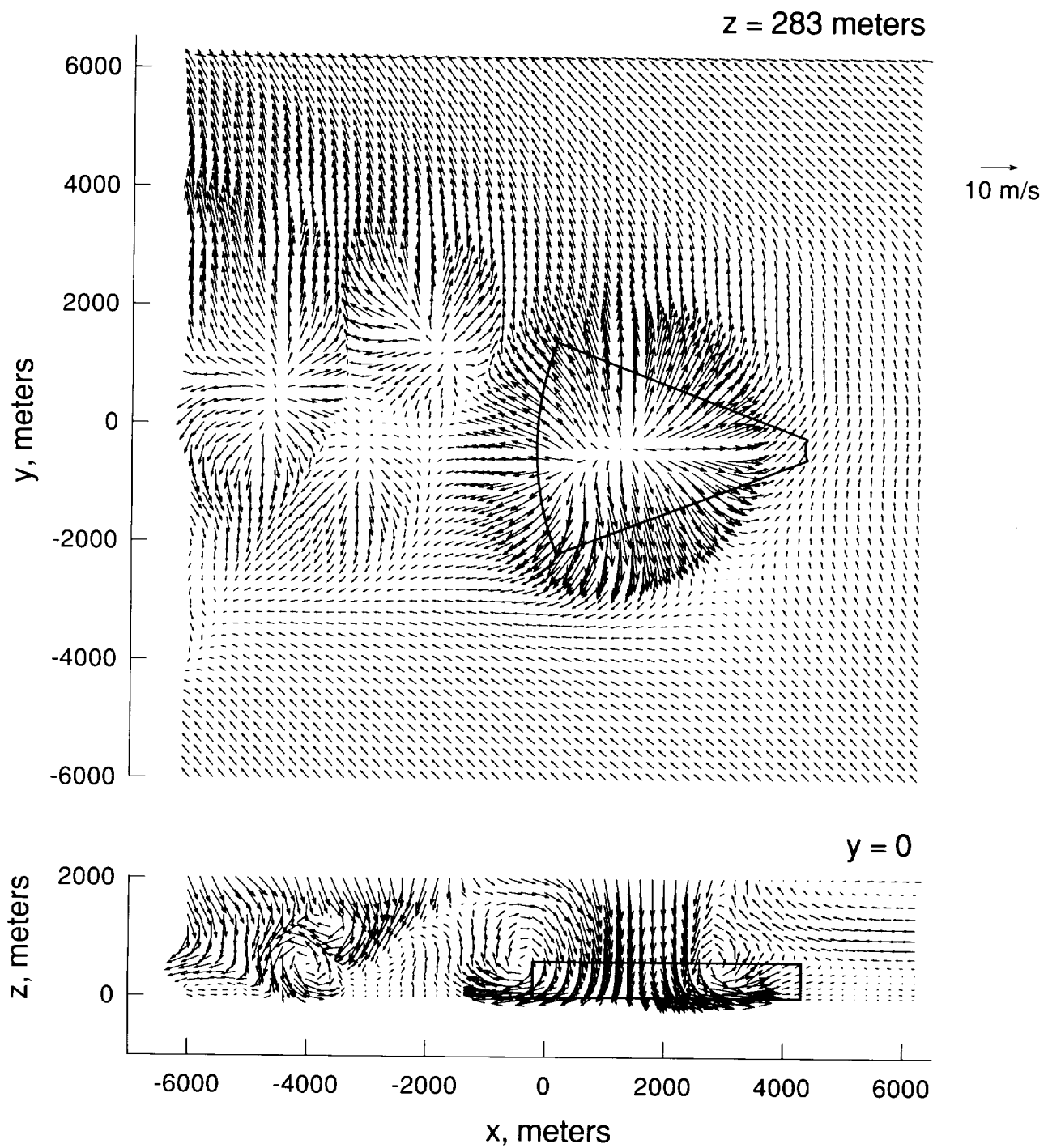
(c) $t = 51$ min.

Figure 3. Concluded.
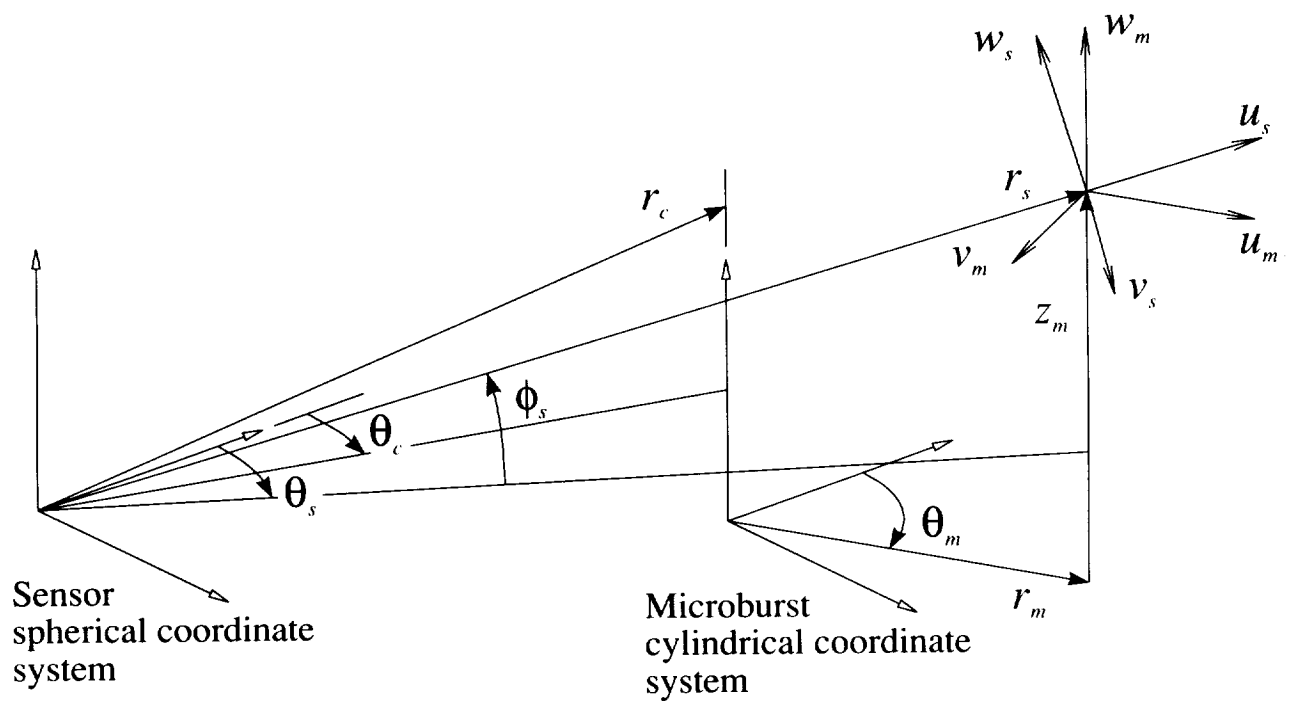
Figure 4. Microburst and sensor-referenced coordinate systems and corresponding velocity components.
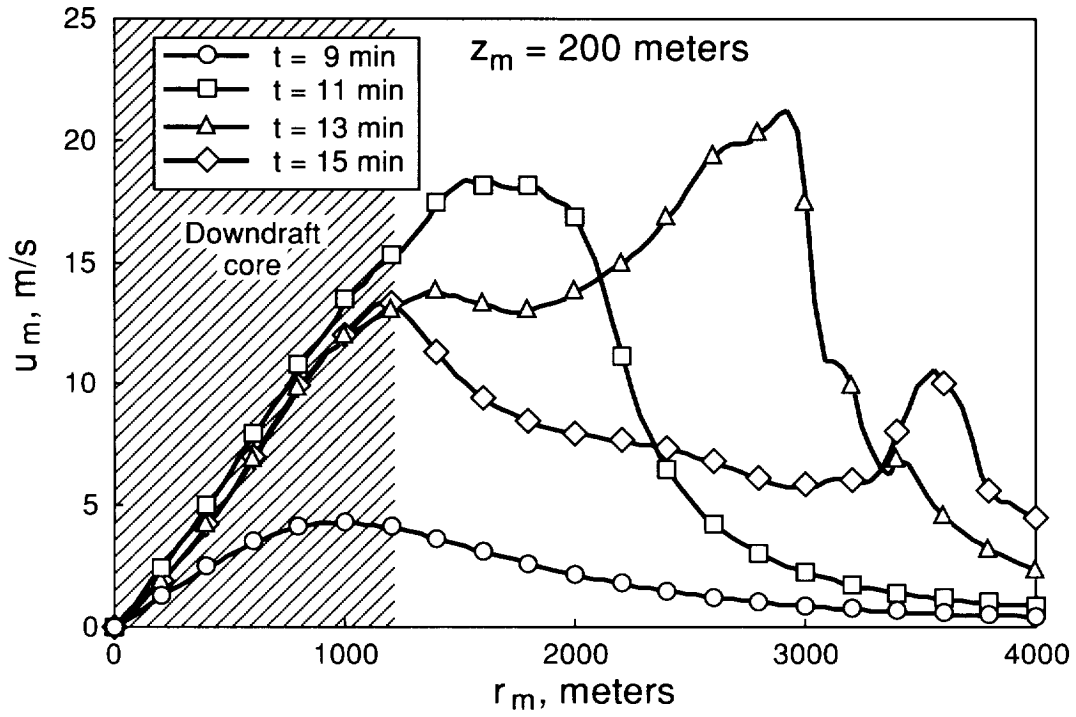
Figure 5. Radial variation of radial wind of TASS generated axisymmetric microburst. (From ref. 3.)
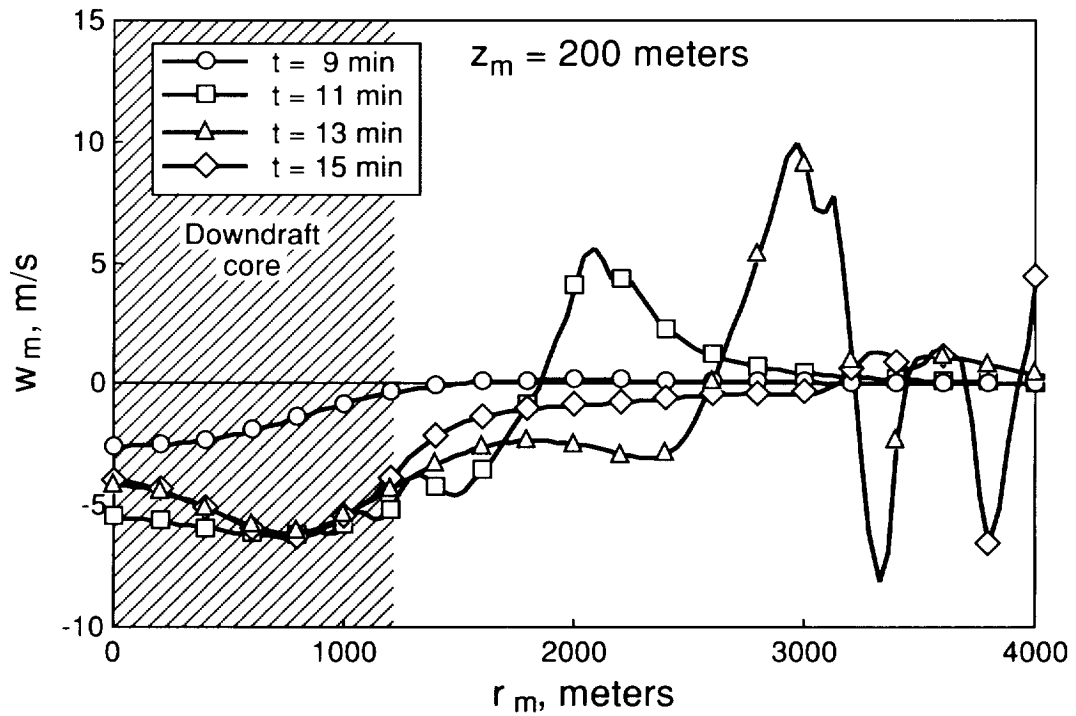
Figure 6. Radial variation of vertical wind of TASS generated axisymmetric microburst. (From ref. 3.)
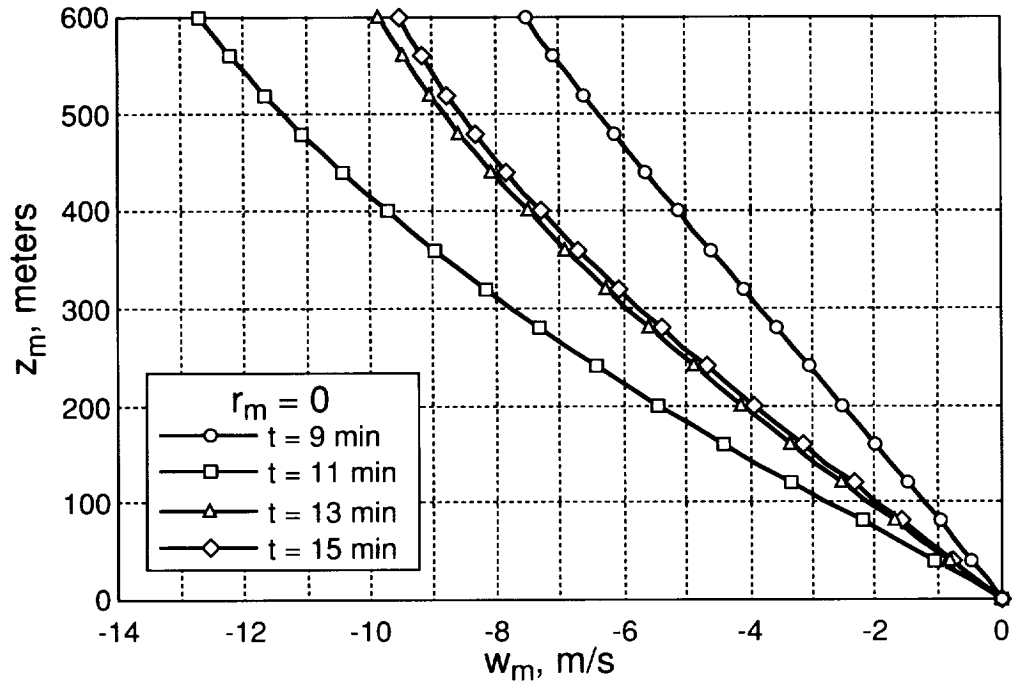
Figure 7. Vertical wind variation with altitude at center of TASS generated axisymmetric microburst.
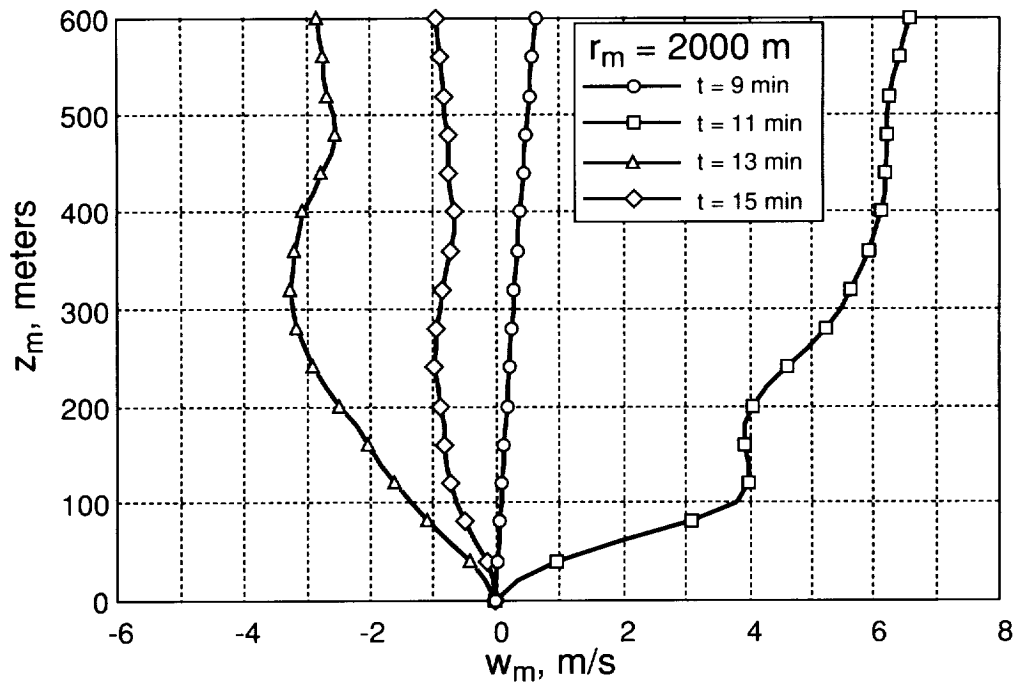
Figure 8. Vertical wind variation with altitude of TASS generated axisymmetric microburst at a radius of 2000 m.
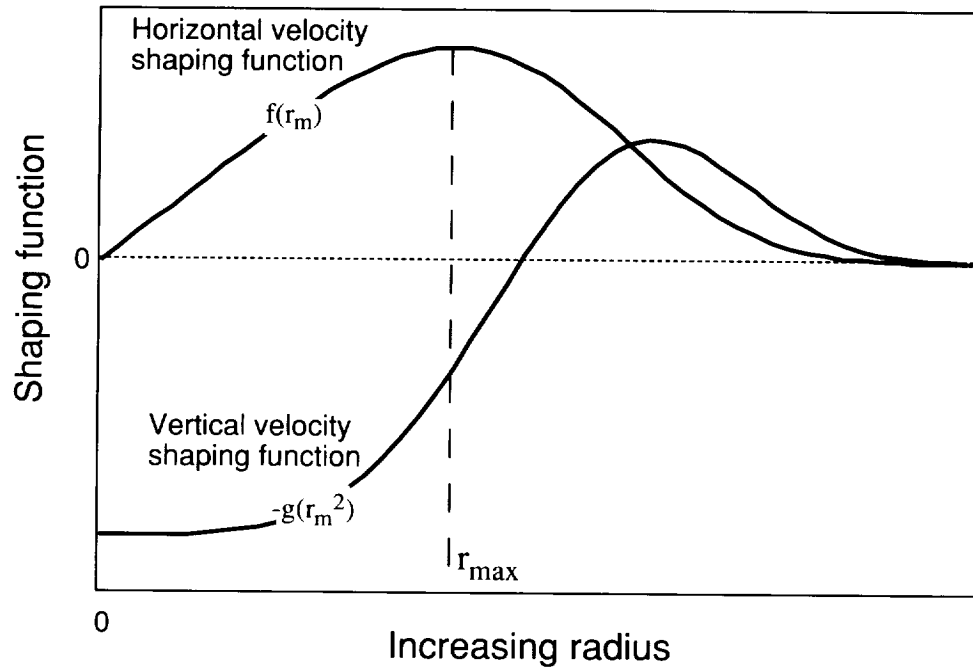
Figure 9. Characteristic variation of radial shaping functions.
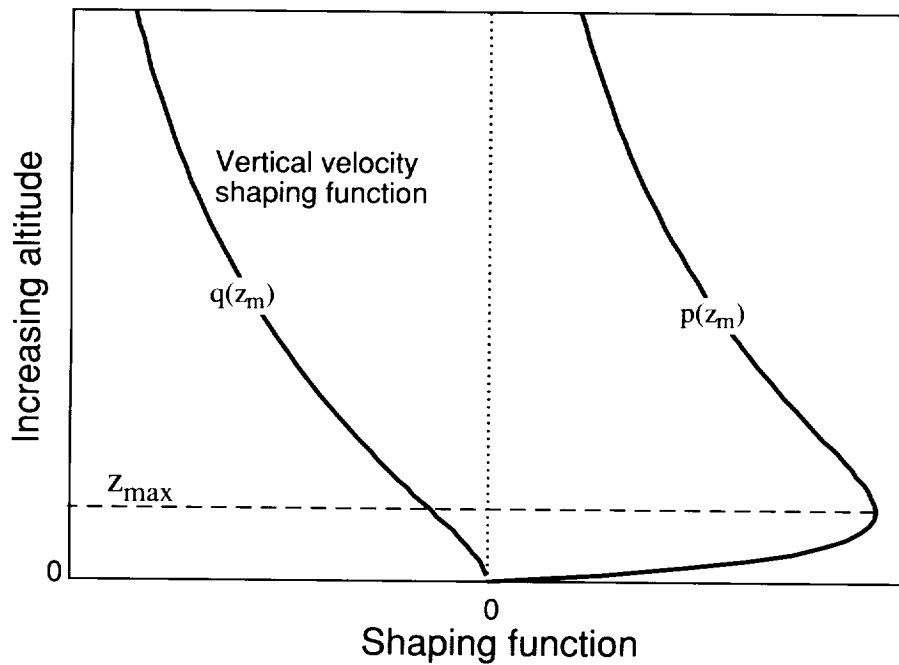
Figure 10. Characteristic variation of vertical shaping functions.
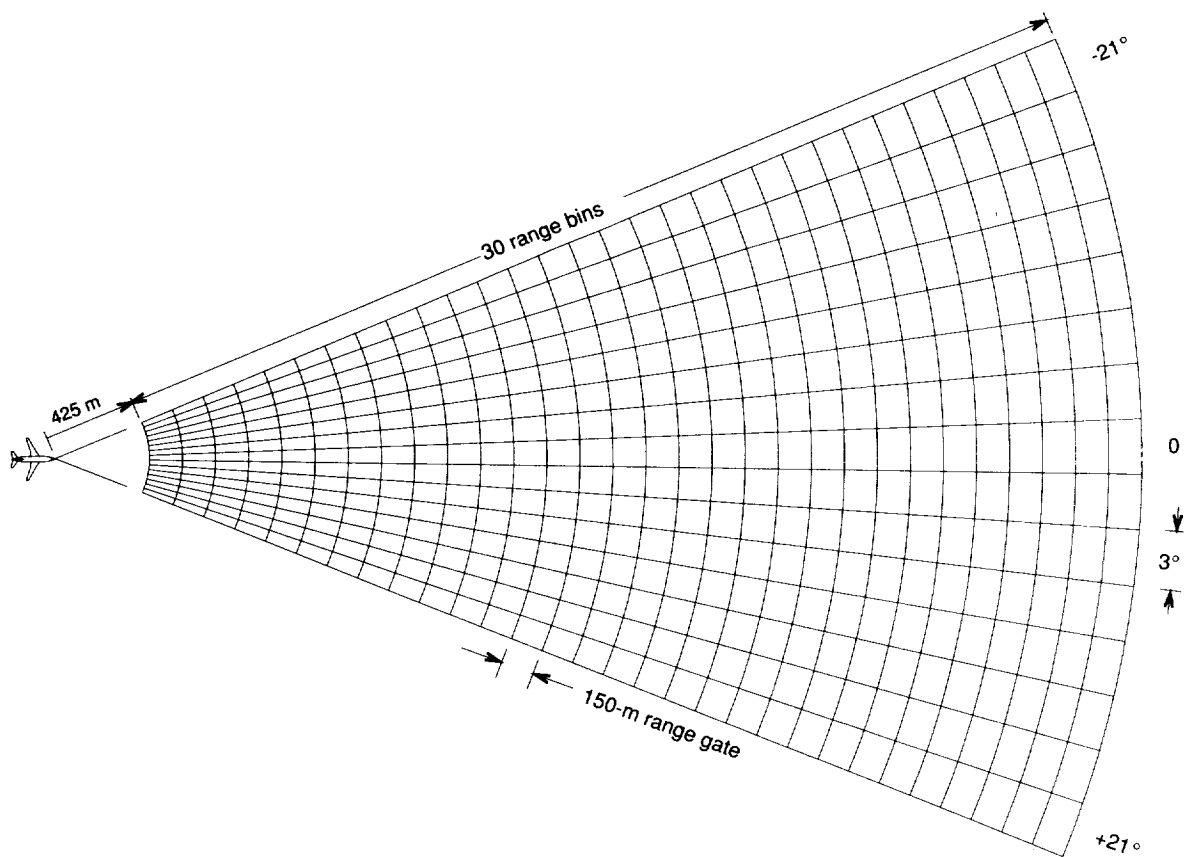
Figure 11. Radar simulation measurement grid.

True radial wind   Measured radial wind

u_s, m/s

14
12
10
8
6
4
2
0
-2
-4
-6
-8
-10
-12
-14

600 meters

500 meters

400 meters

300 meters

200 meters

100 meters
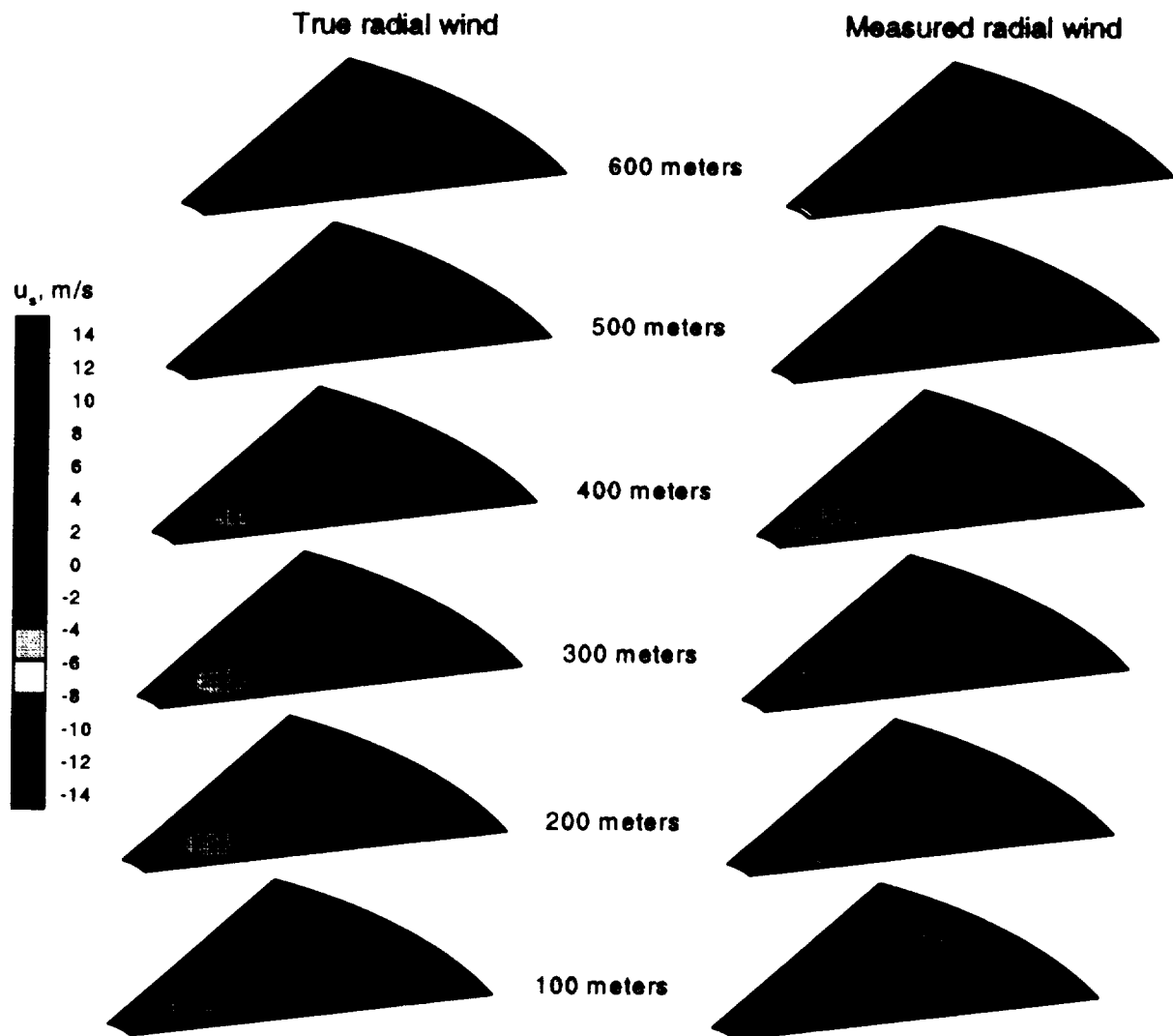
(a) $t = 49$ min.

Figure 12. True radial wind and measured radial wind from AWDRS program at six scan altitudes for asymmetric microburst case.

True radial wind

Measured radial wind

u_s, m/s

14
12
10
8
6
4
2
0
-2
-4
-6
-8
-10
-12
-14

600 meters

500 meters

400 meters

300 meters

200 meters

100 meters
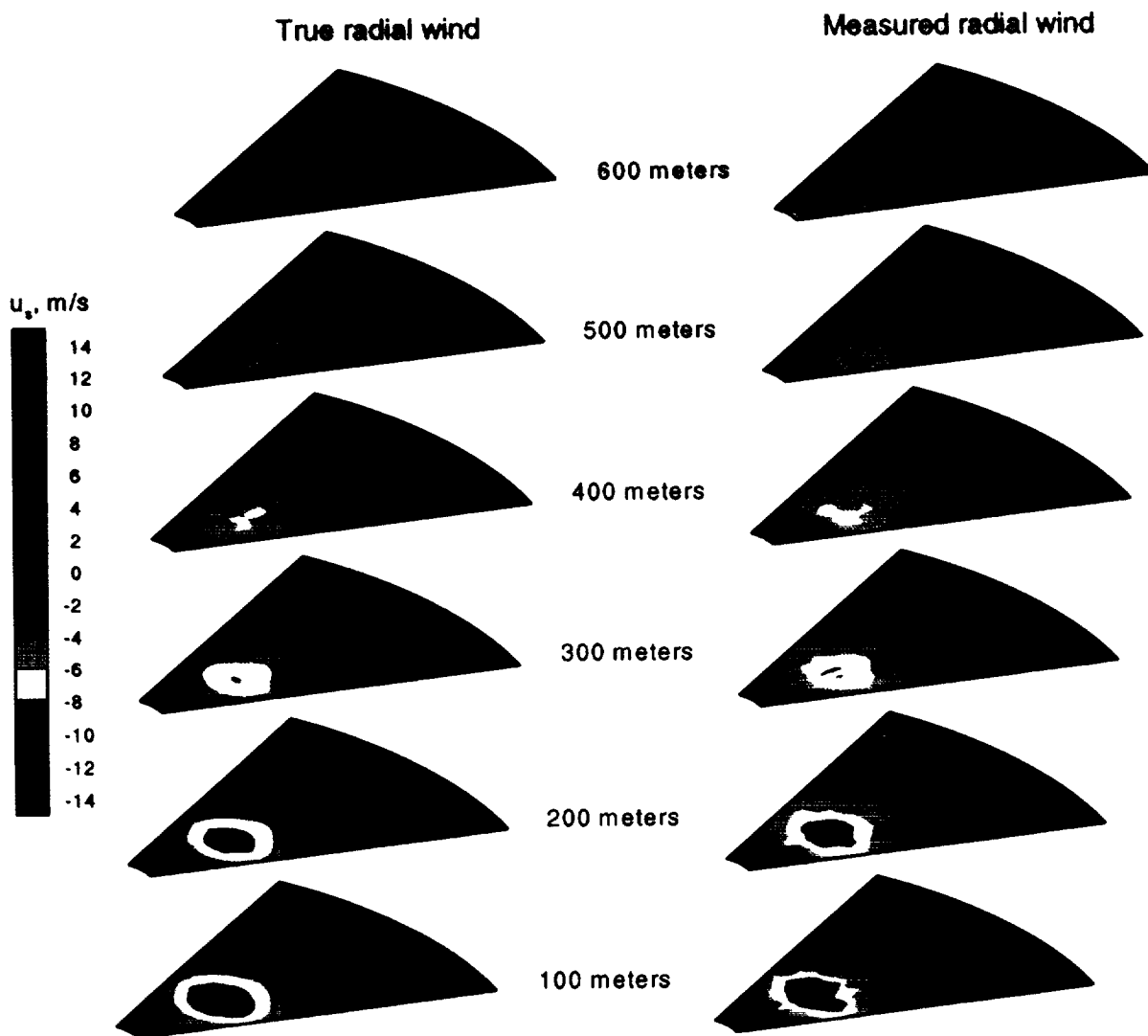
(b) $t = 50$ min.

Figure 12. Continued.

True radial wind   Measured radial wind

u$_s$, m/s

14
12
10
8
6
4
2
0
-2
-4
-6
-8
-10
-12
-14

600 meters

500 meters

400 meters

300 meters

200 meters

100 meters
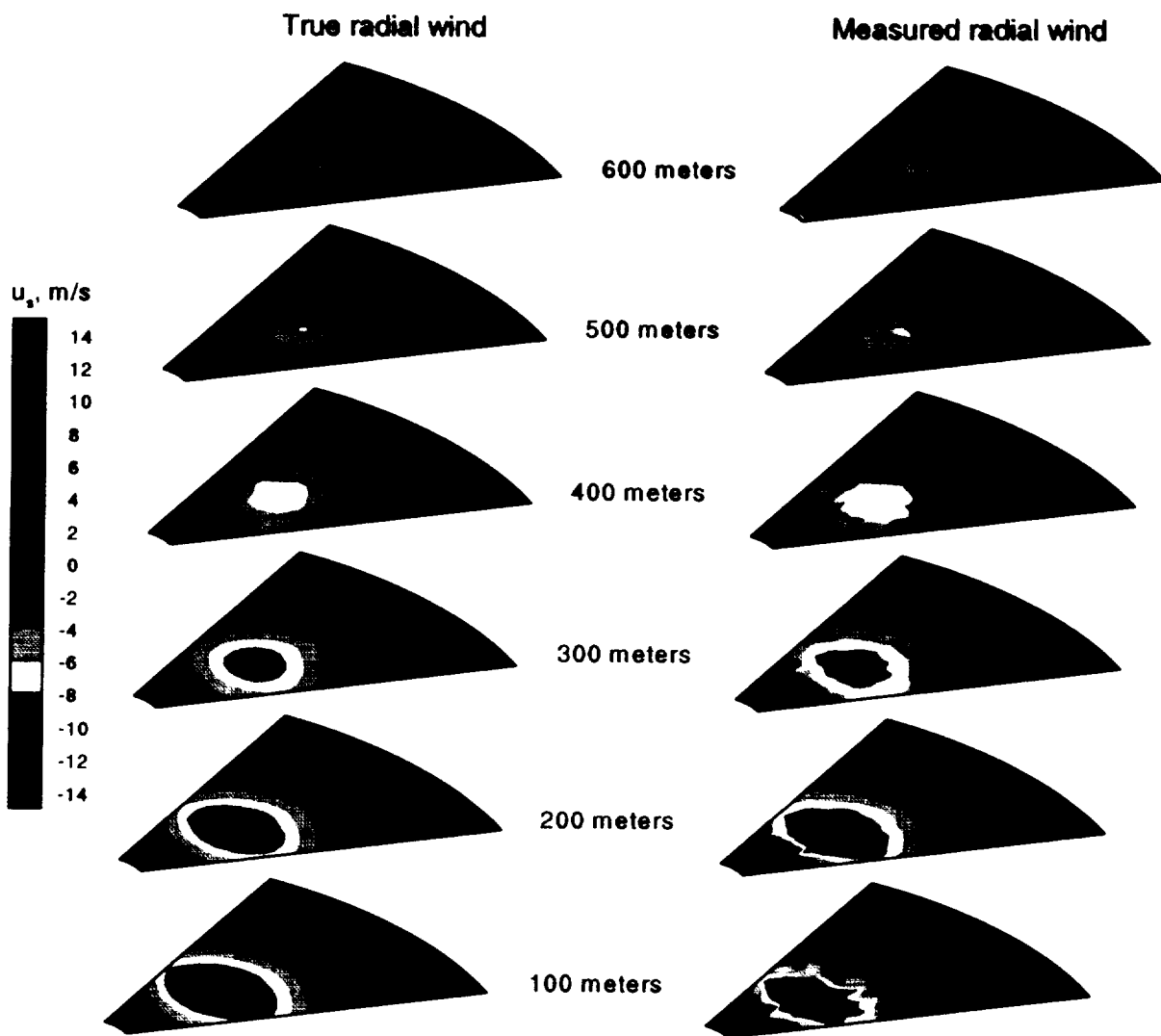
(c) $t = 51$ min.

Figure 12. Concluded.
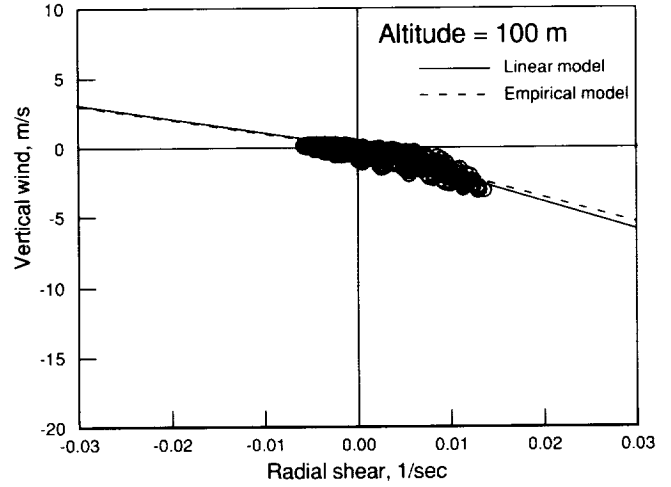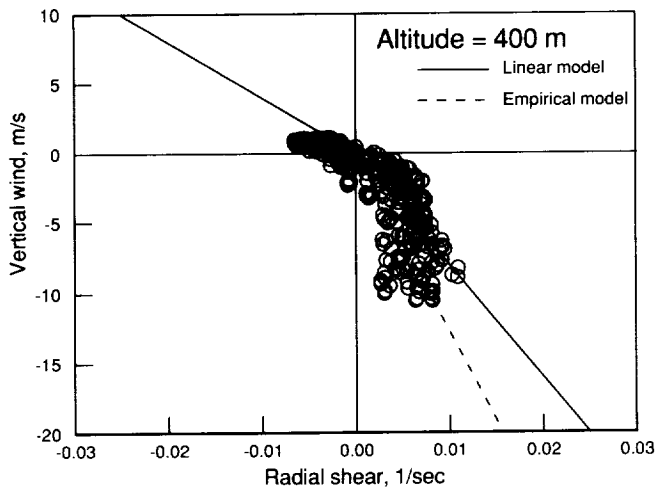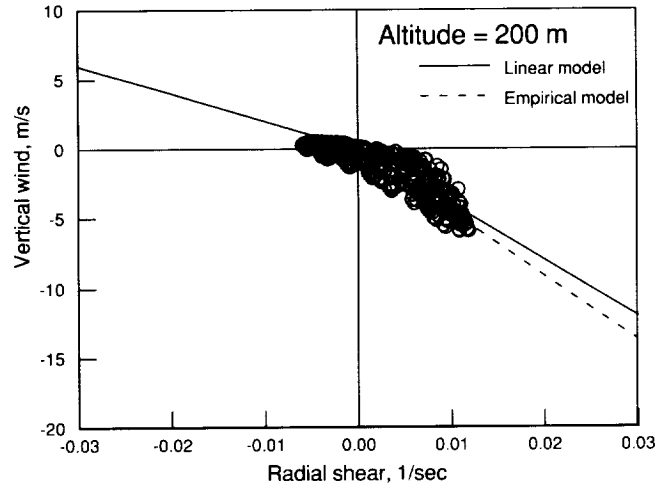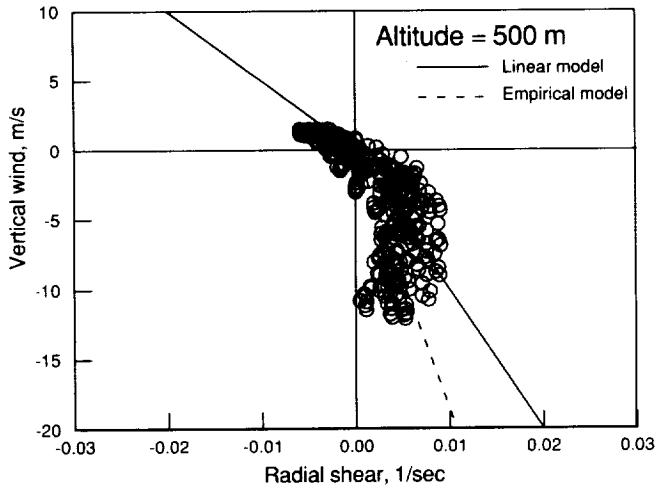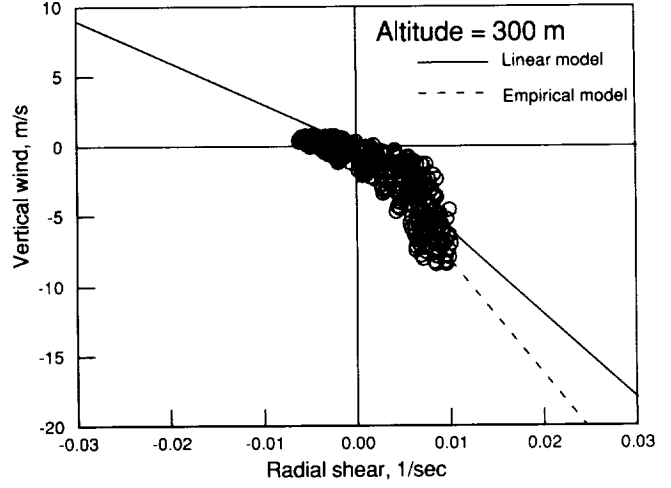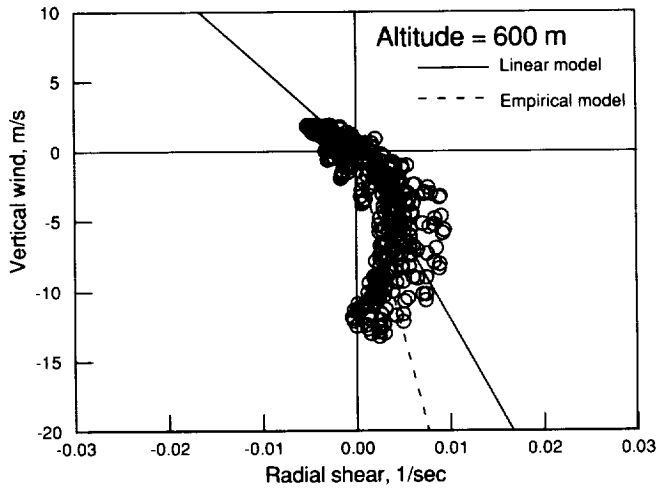
(a) $t = 49$ min.

Figure 13. Vertical wind and radial shear at each radar scan grid point.
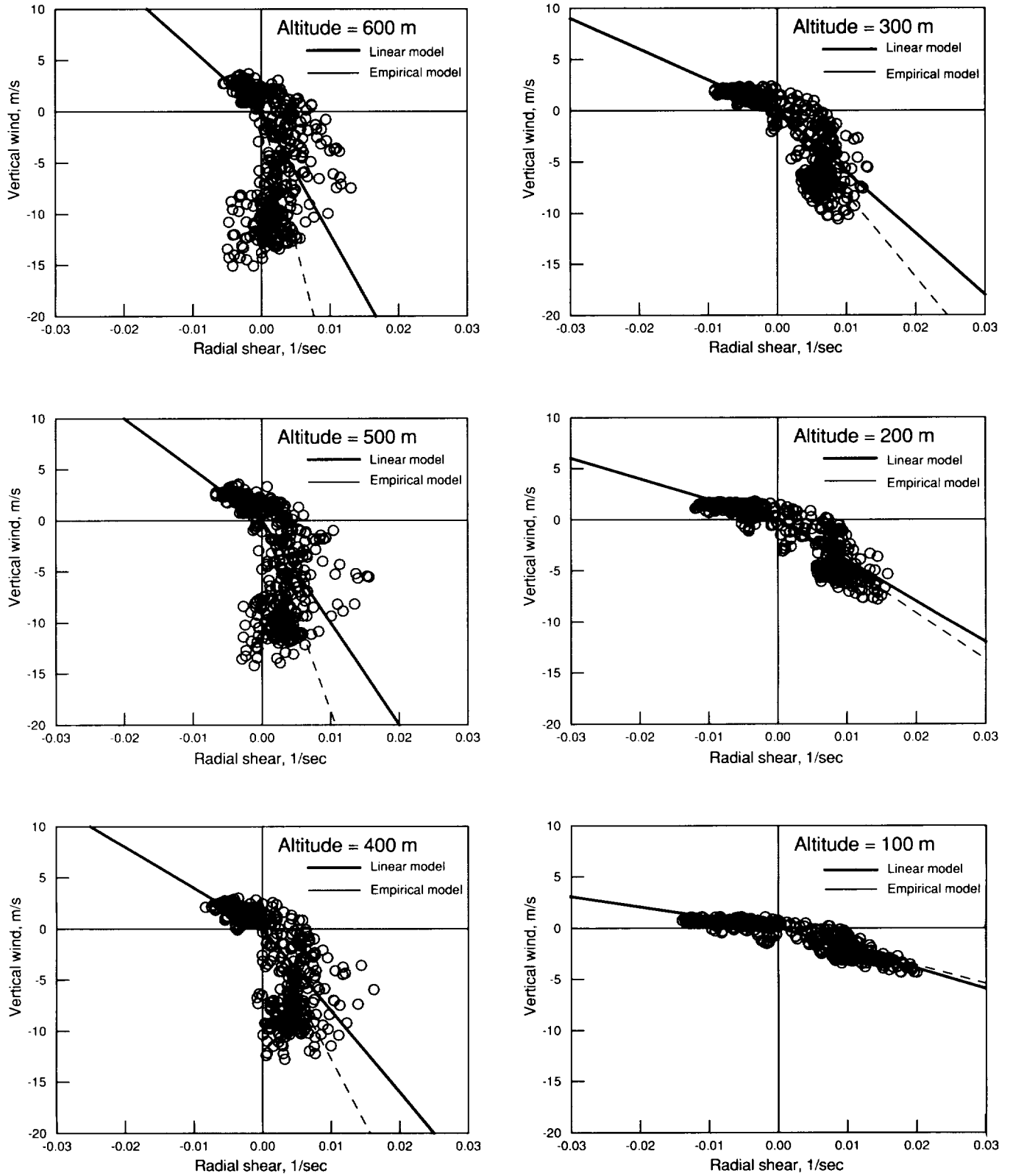
(b) $t = 50$ min.

Figure 13. Continued.

(c) $t = 51$ min.

Figrue 13. Concluded.
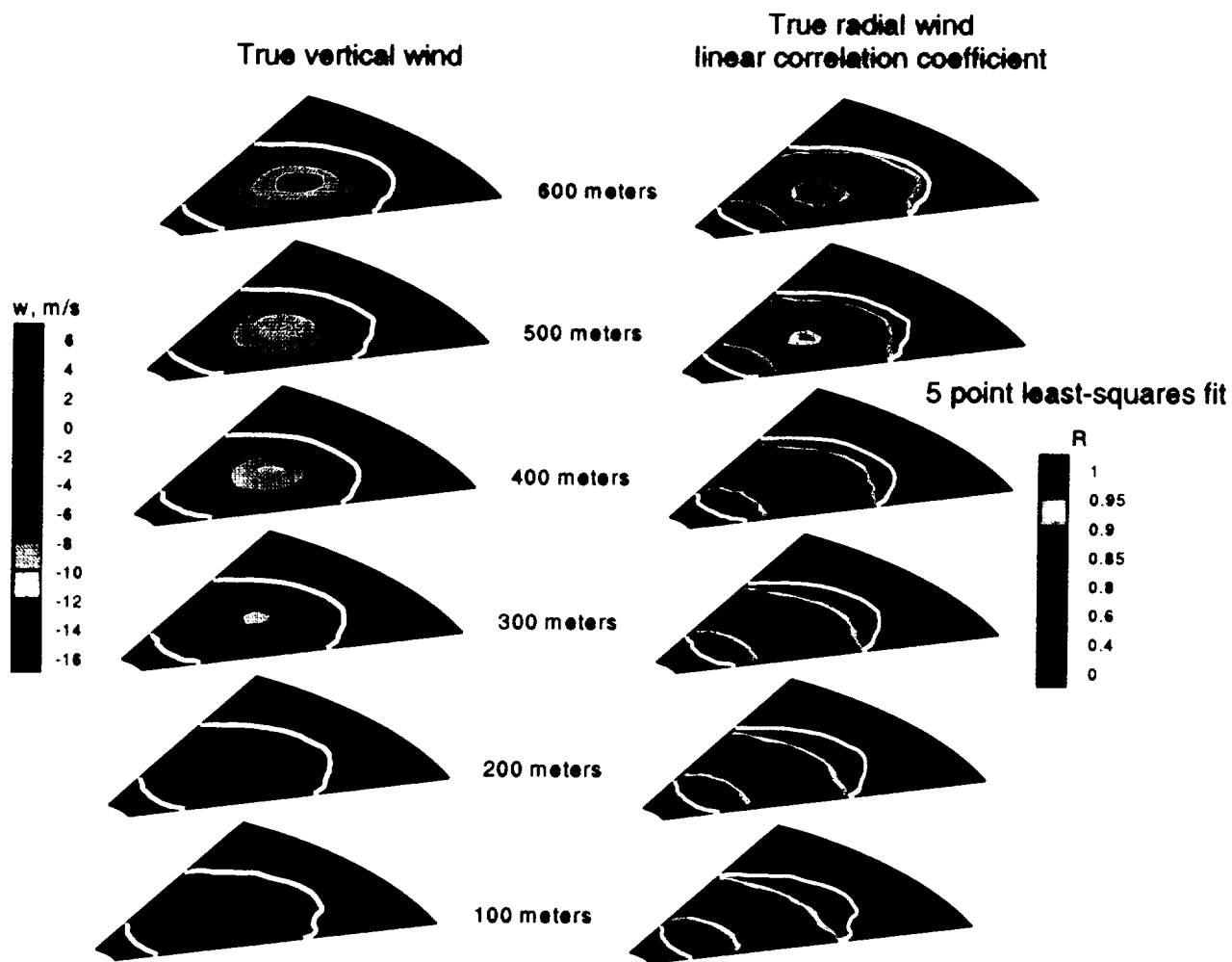
Figure 14. Vertical wind and linear correlation coefficient of radial wind profile at six scan altitudes for asymmetric microburst case.

(a) $t = 49$ min.

True vertical wind

**True radial wind
linear correlation coefficient**

5 point least-squares fit
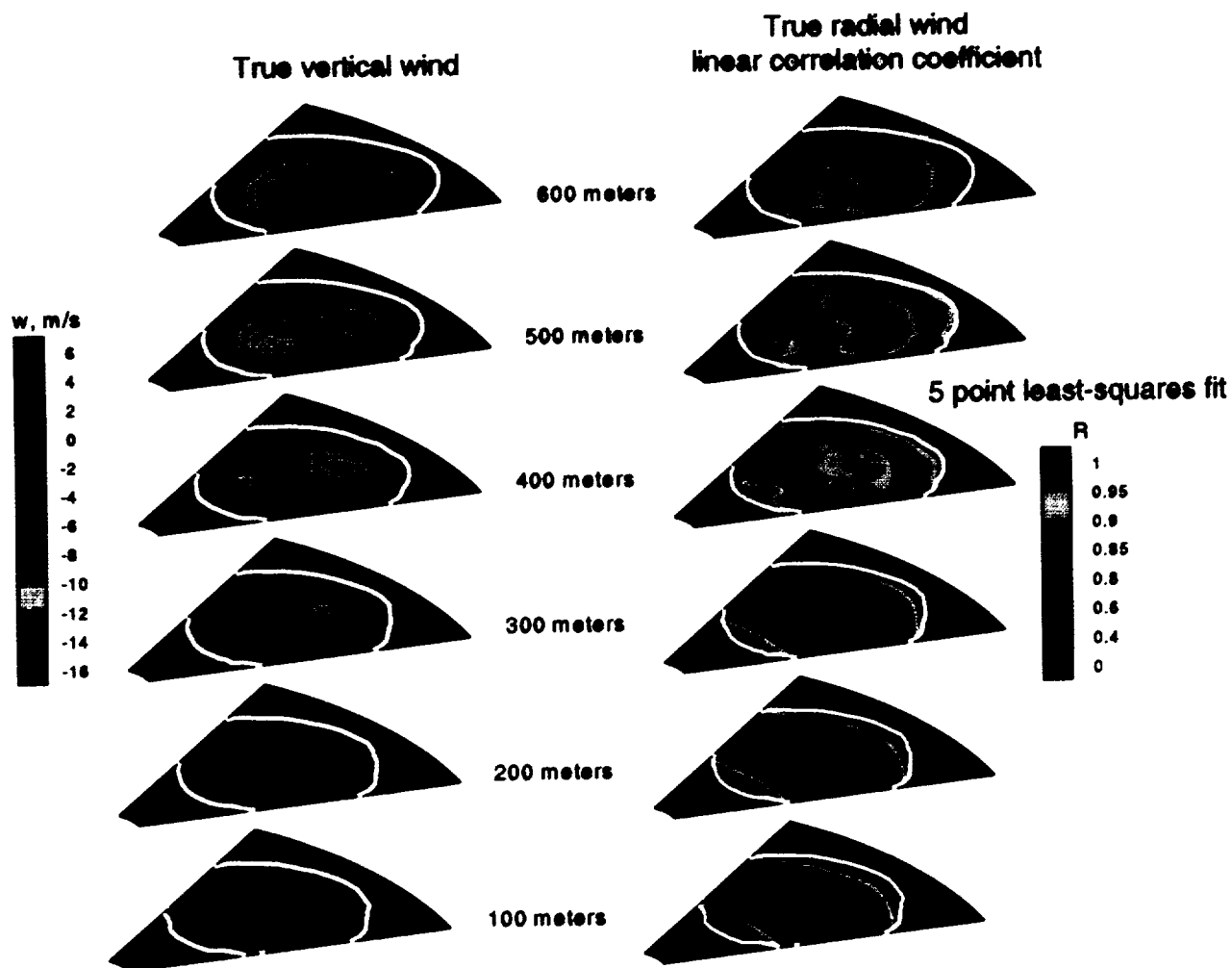
(b) $t = 50$ min.

Figure 14. Continued.

True vertical wind

True radial wind
linear correlation coefficient

w, m/s

6
4
2
0
-2
-4
-6
-8
-10
-12
-14
-16

600 meters

500 meters

400 meters

300 meters

200 meters

100 meters

5 point least-squares fit

R

1
0.95
0.9
0.85
0.8
0.6
0.4
0
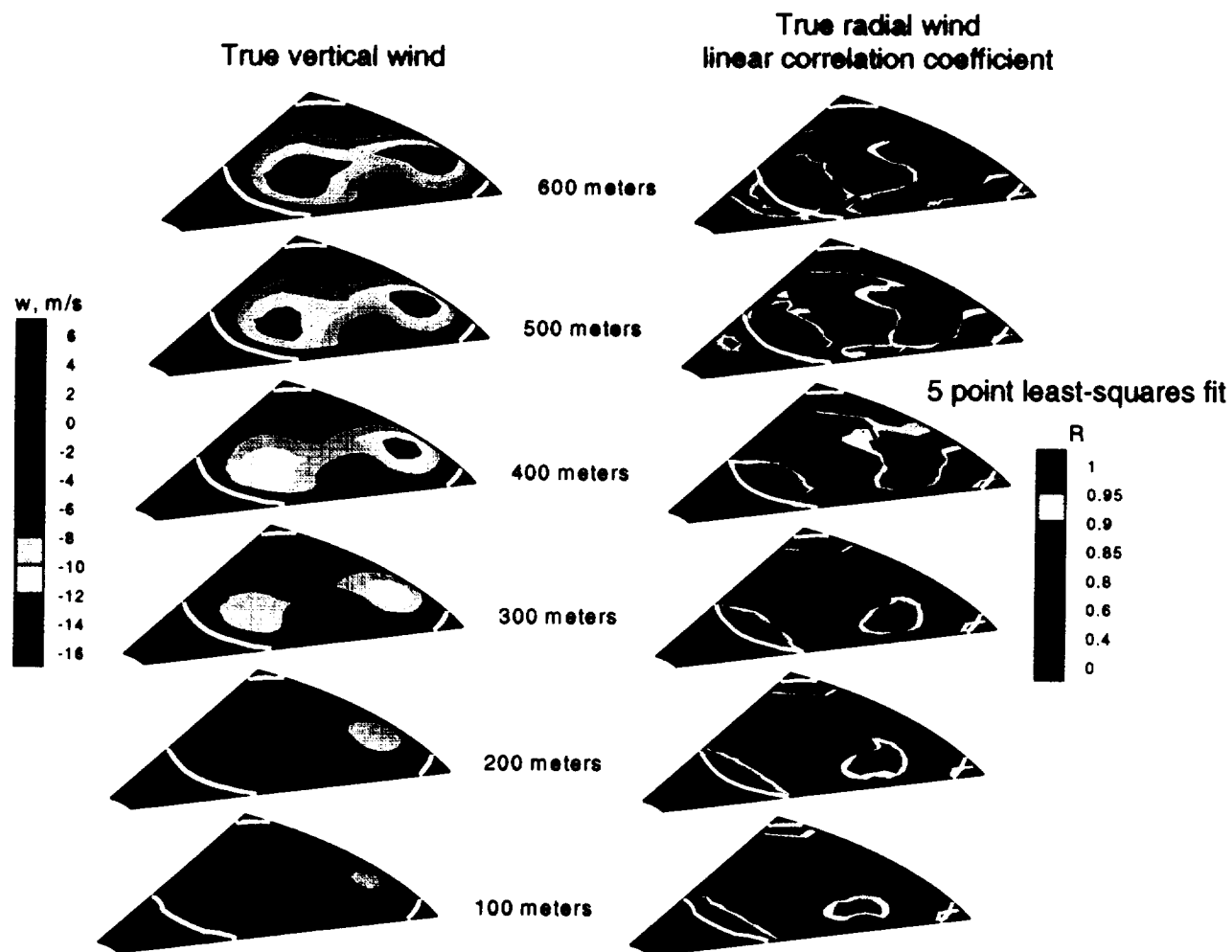
(c) $t = 51$ min.

Figure 14. Concluded.

True vertical wind

Measured radial wind
linear correlation coefficient

w, m/s

5 point least-squares fit
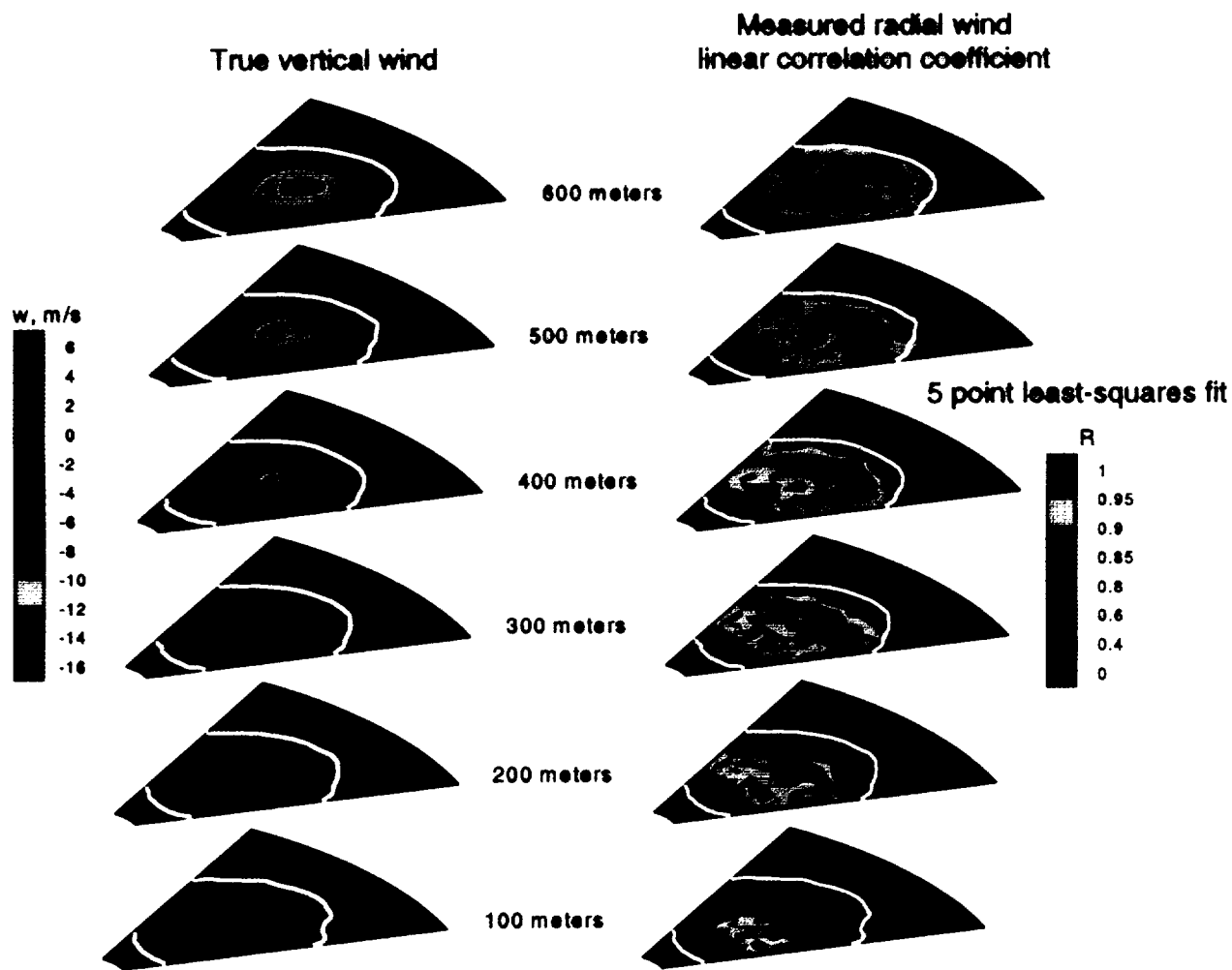
(a) $t = 49$ min.

Figure 15. Vertical wind and linear correlation coefficient of simulated radar radial wind measurement at six scan altitudes for asymmetric microburst case.

True vertical wind

Measured radial wind
linear correlation coefficient

w, m/s

600 meters

500 meters

400 meters

300 meters

200 meters

100 meters

5 point least-squares fit

R
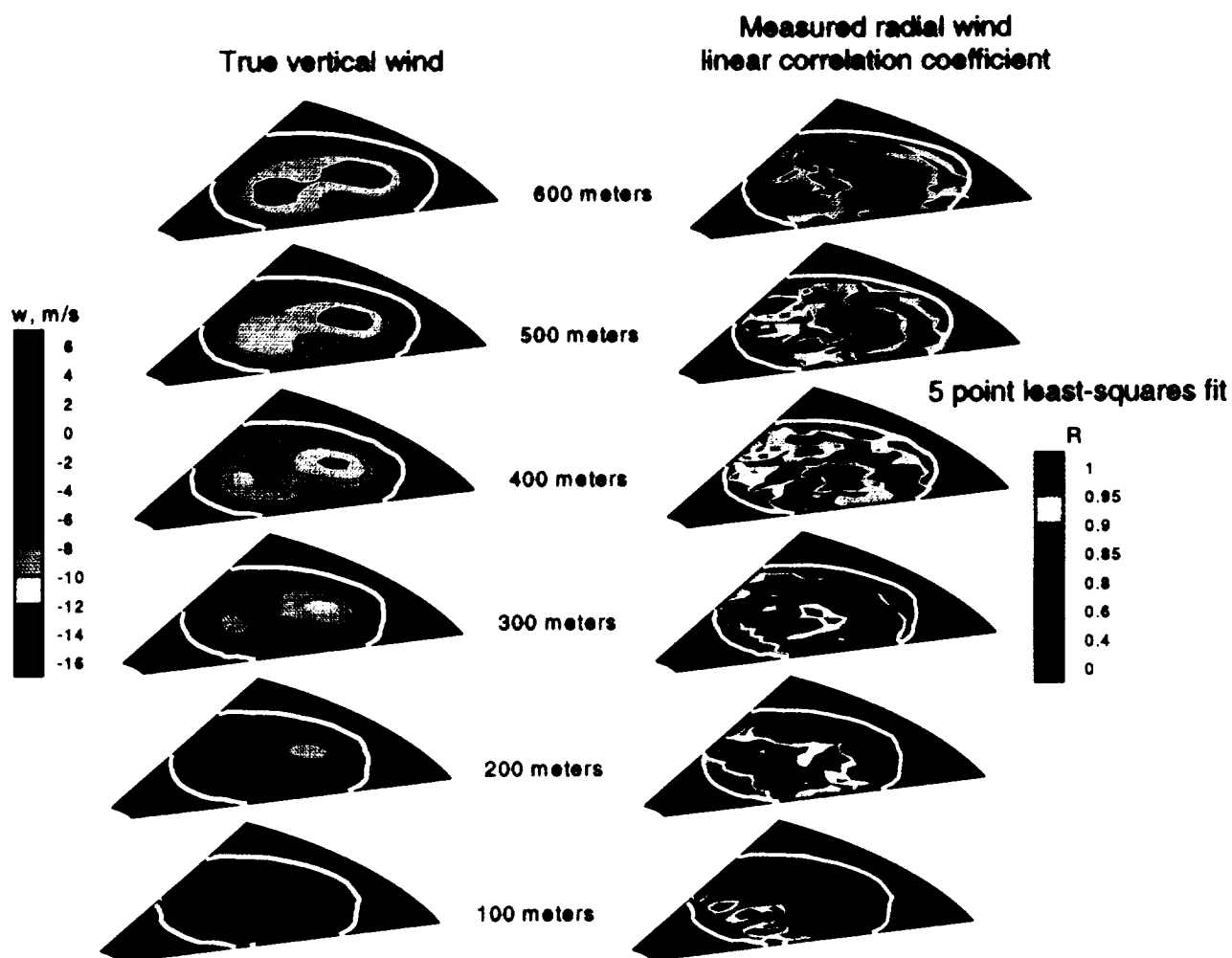
(b) $t = 50$ min.

Figure 15. Continued.

True vertical wind

Measured radial wind
linear correlation coefficient

w, m/s

6
4
2
0
-2
-4
-6
-8
-10
-12
-14
-16

600 meters

500 meters

400 meters

300 meters

200 meters

100 meters

5 point least-squares fit

R

1
0.95
0.9
0.85
0.8
0.6
0.4
0
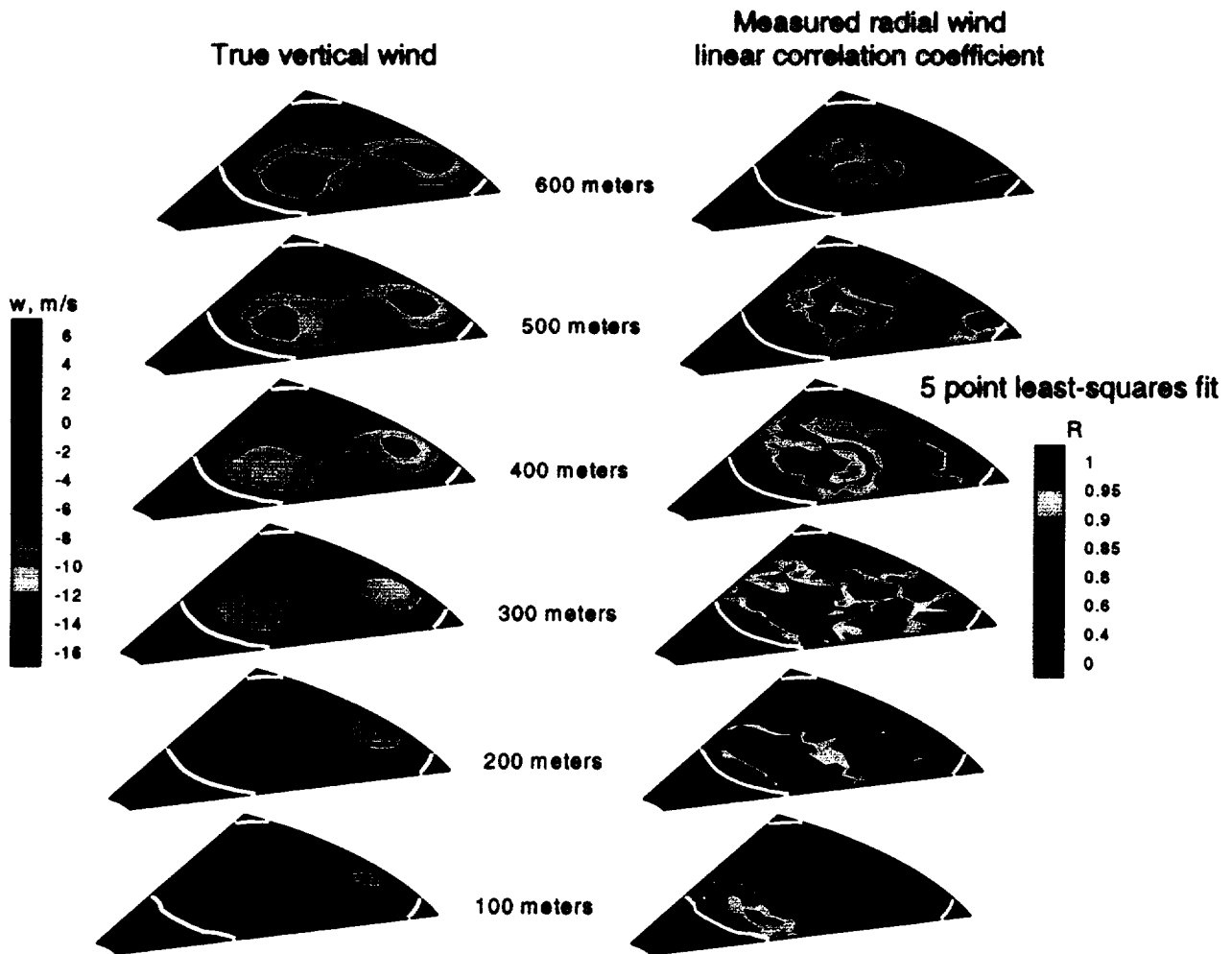
(c) $t = 51$ min.

Figure 15. Concluded.

42
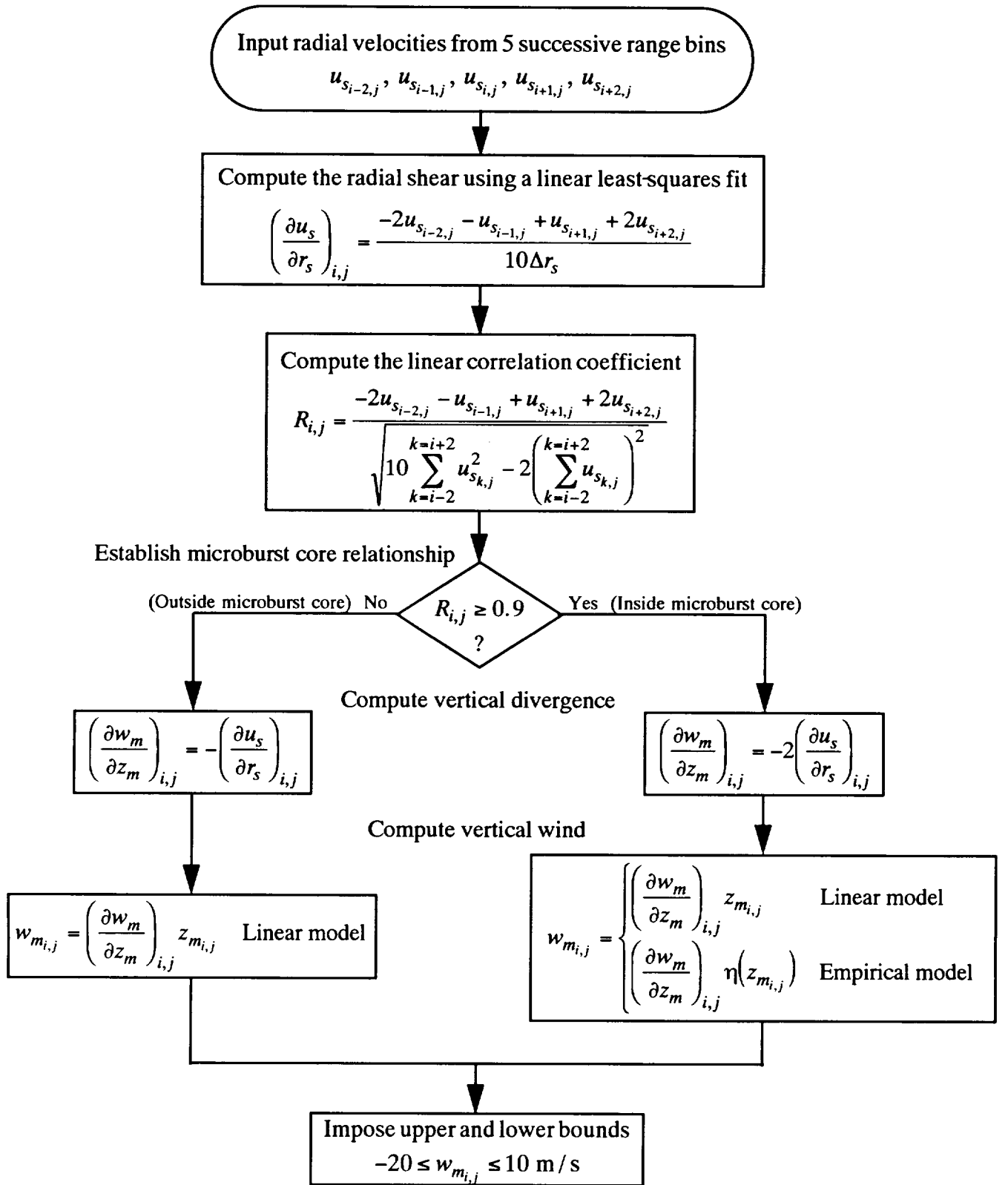
Figure 16. Flowchart of vertical wind calculation at range bin i along scan line j. $3 \leq i \leq$ Number of range bins -2; $1 \leq j \leq$ Number of scan lines.
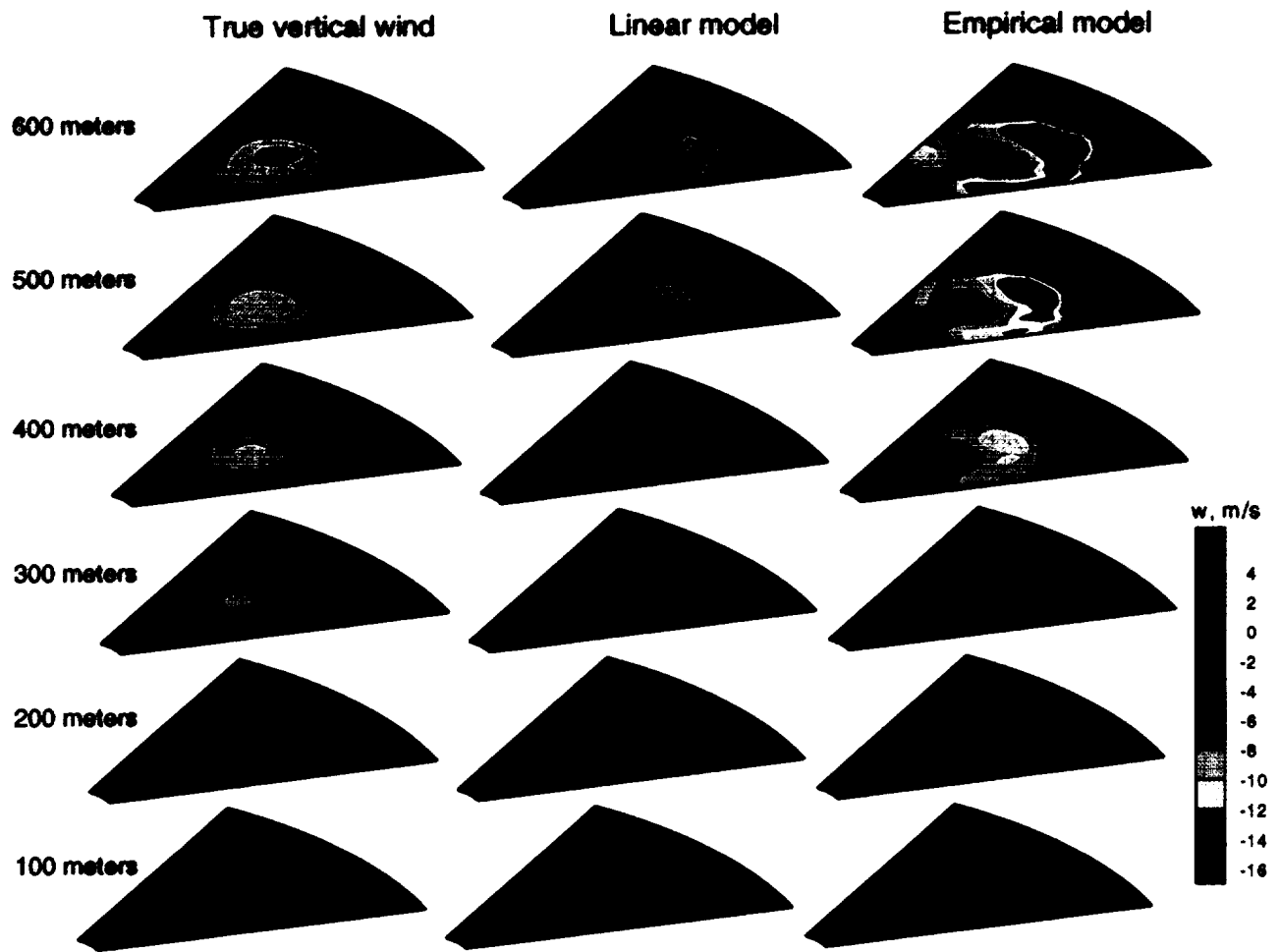
(a) $t = 49$ min.

Figure 17. True vertical wind and vertical wind computed from linear and empirical models with no measurement error at six scan altitudes for asymmetric microburst case.

True vertical wind Linear model Empirical model
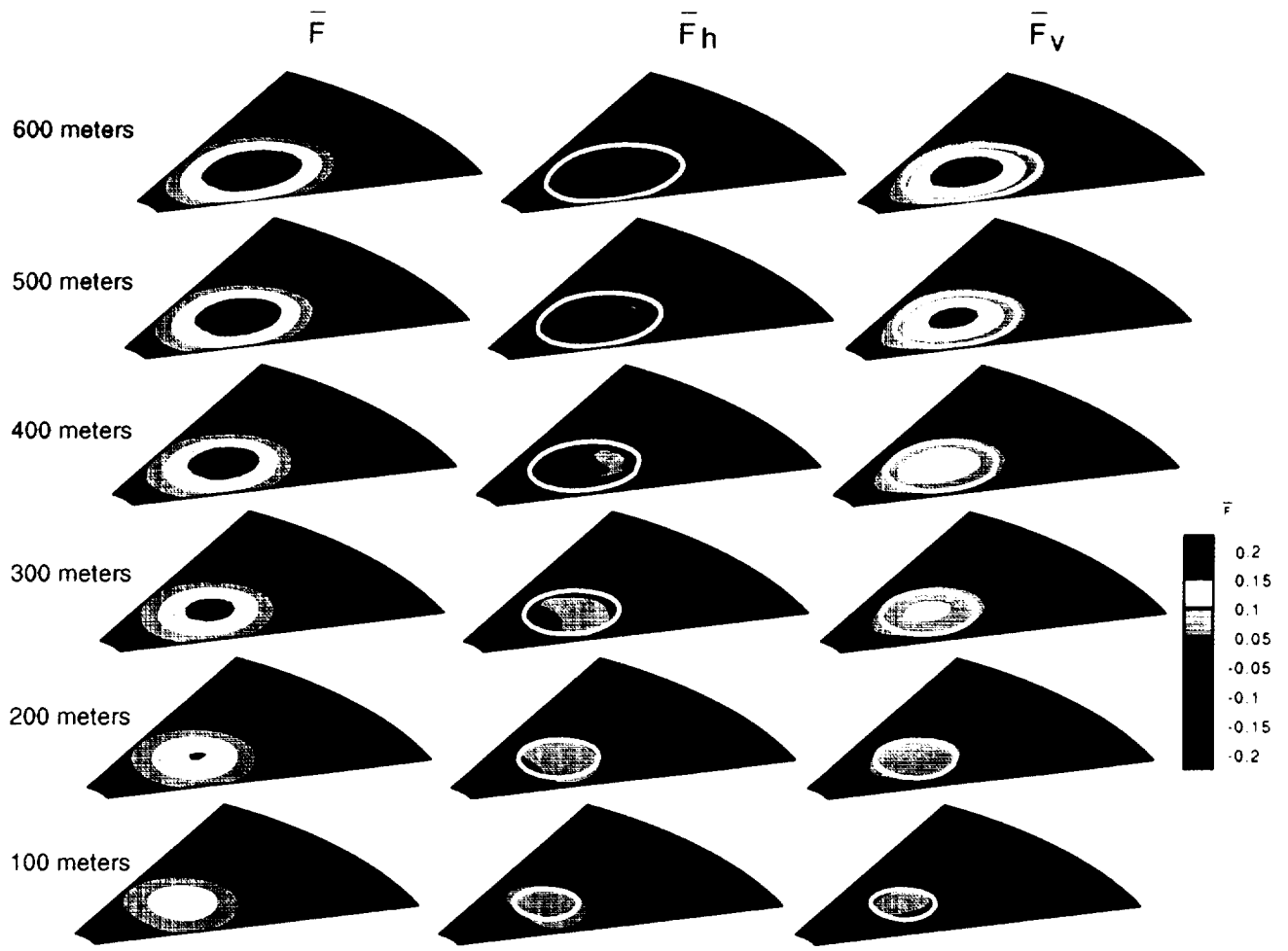
600 meters

500 meters

400 meters

300 meters

200 meters

100 meters

w, m/s

4
2
0
-2
-4
-6
-8
-10
-12
-14
-16
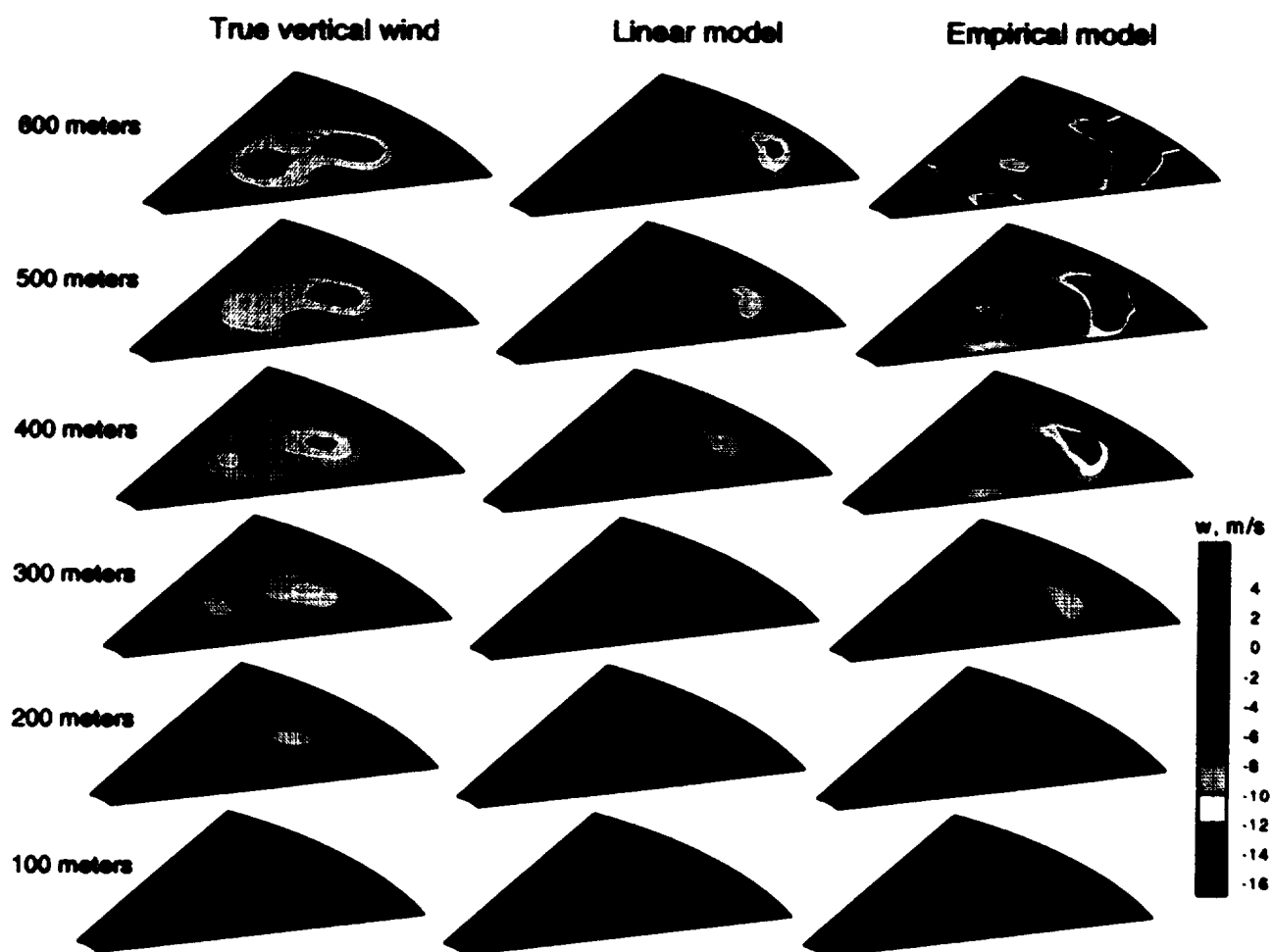
(b) $t = 50$ min.

Figure 17. Continued.
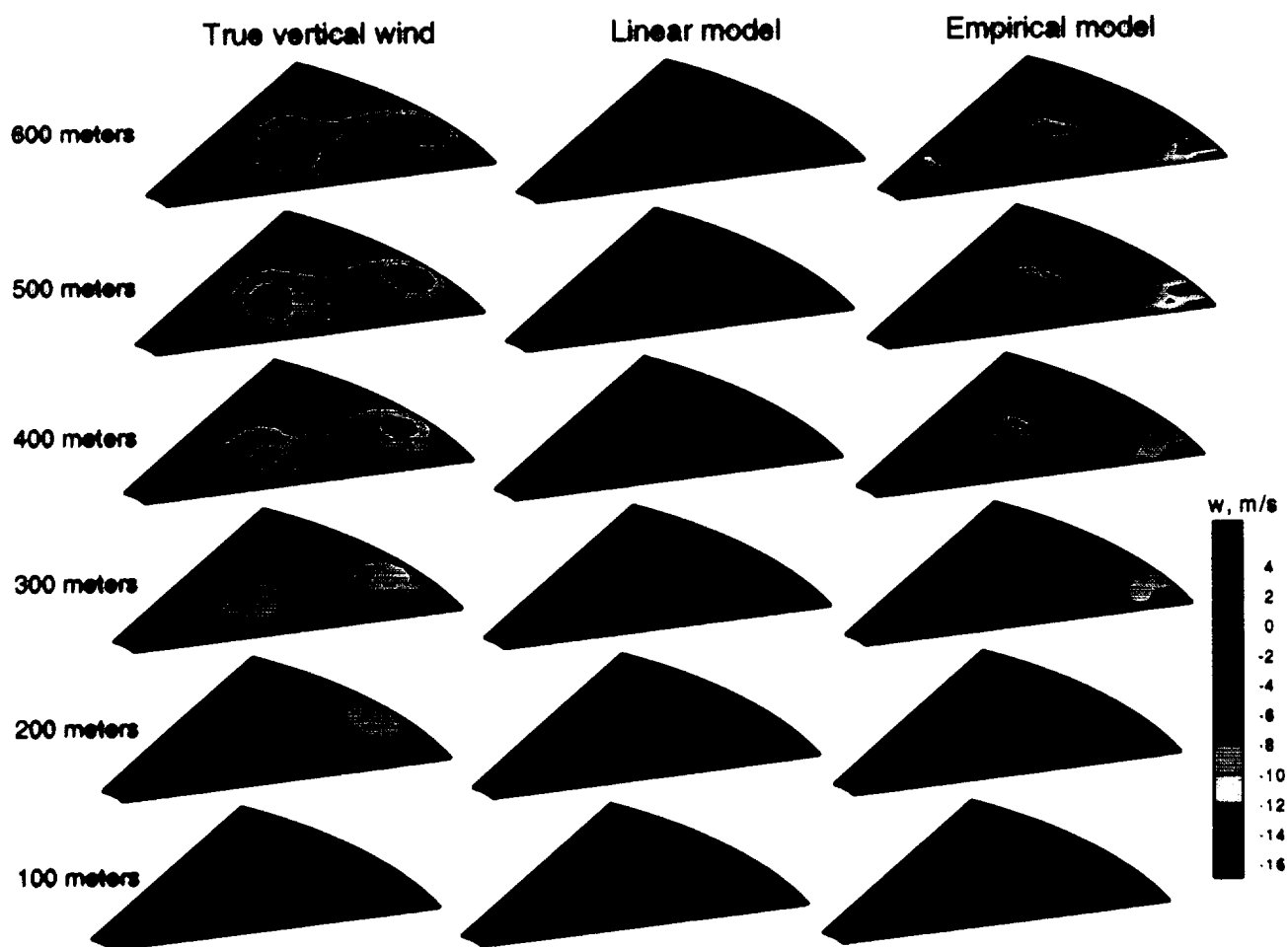
(c) $t = 51$ min.

Figure 17. Concluded.
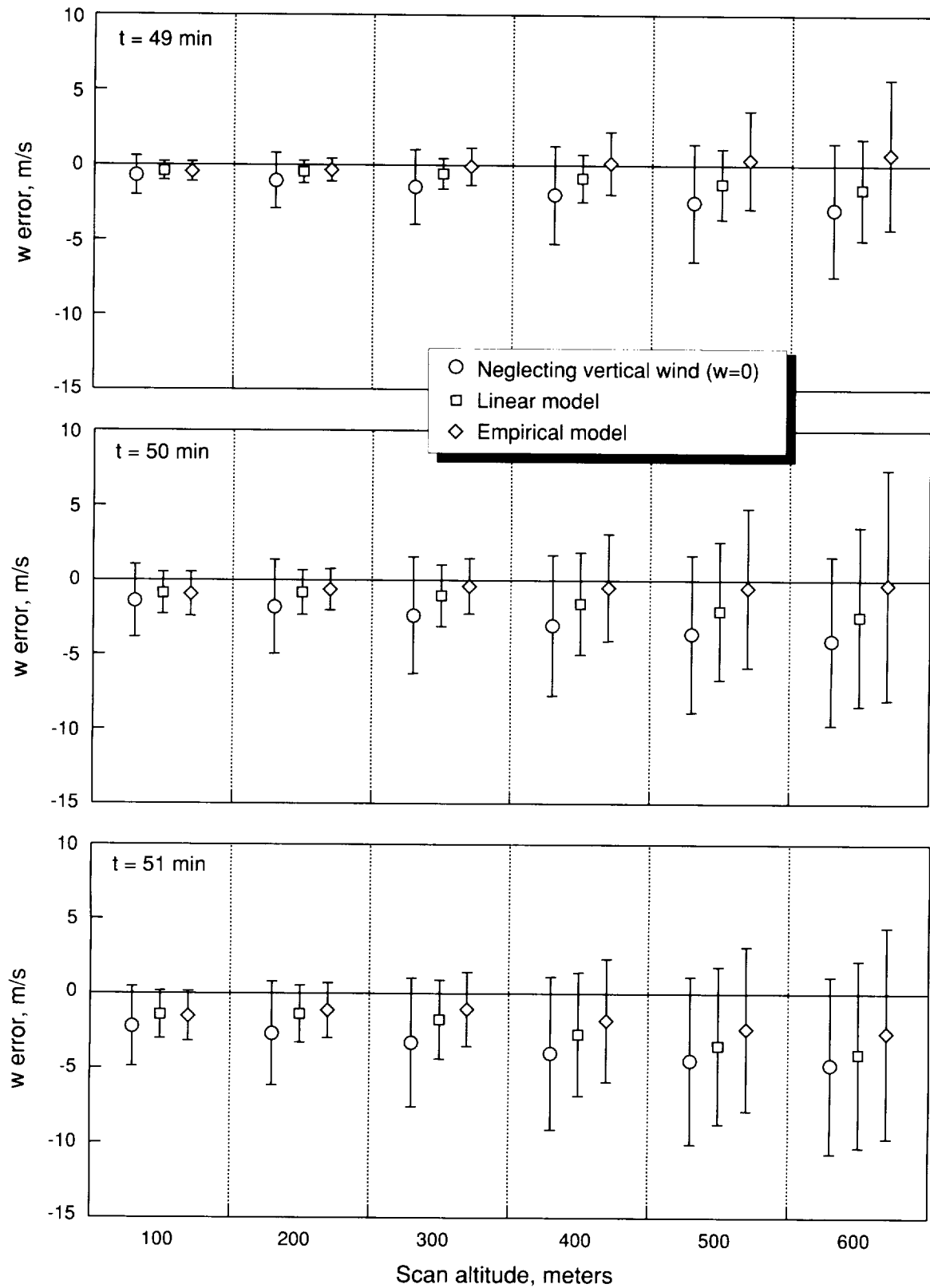
Figure 18. Mean and standard deviation of vertical wind estimate error for asymmetric microburst case with no radar measurement error.
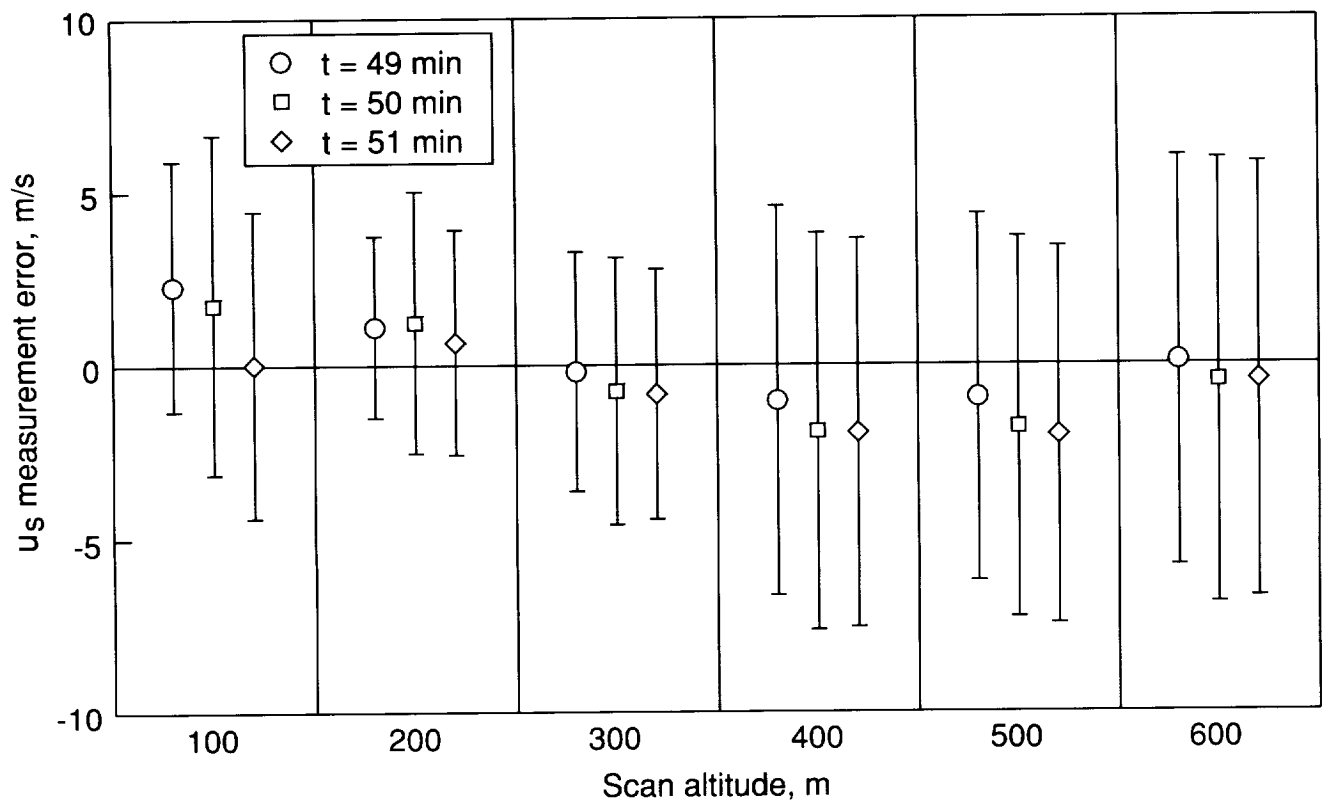
Figure 19.   Mean and standard deviation of simulated radial velocity measurement error of asymmetric microburst case.
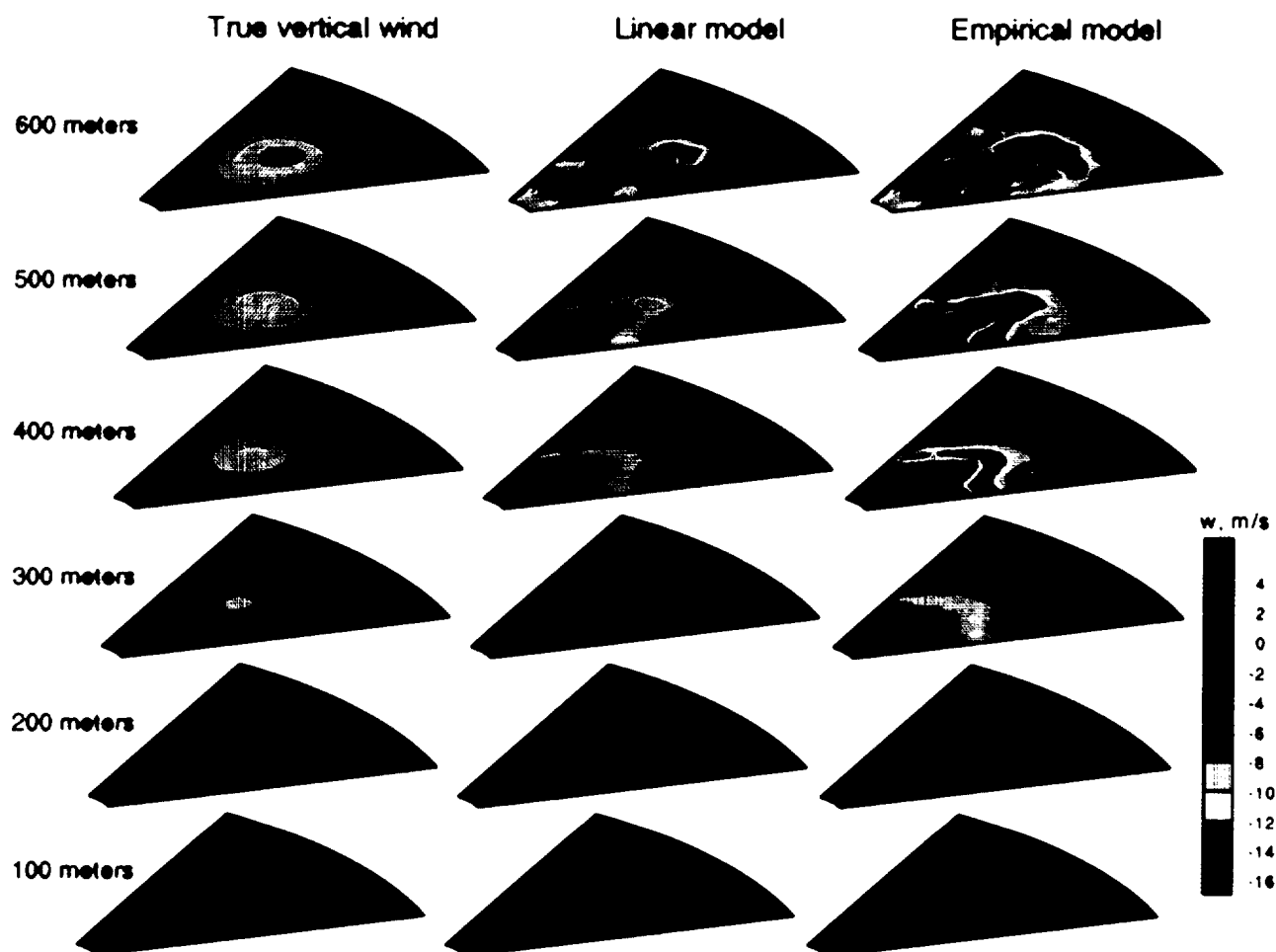
(a) $t = 49$ min.

Figure 20. True vertical wind and vertical wind computed from linear and empirical models with radar measurement errors at six scan altitudes for asymmetric microburst case.

True vertical wind   Linear model   Empirical model

600 meters

500 meters

400 meters

300 meters

200 meters

100 meters

w, m/s

4
2
0
-2
-4
-6
-8
-10
-12
-14
-16
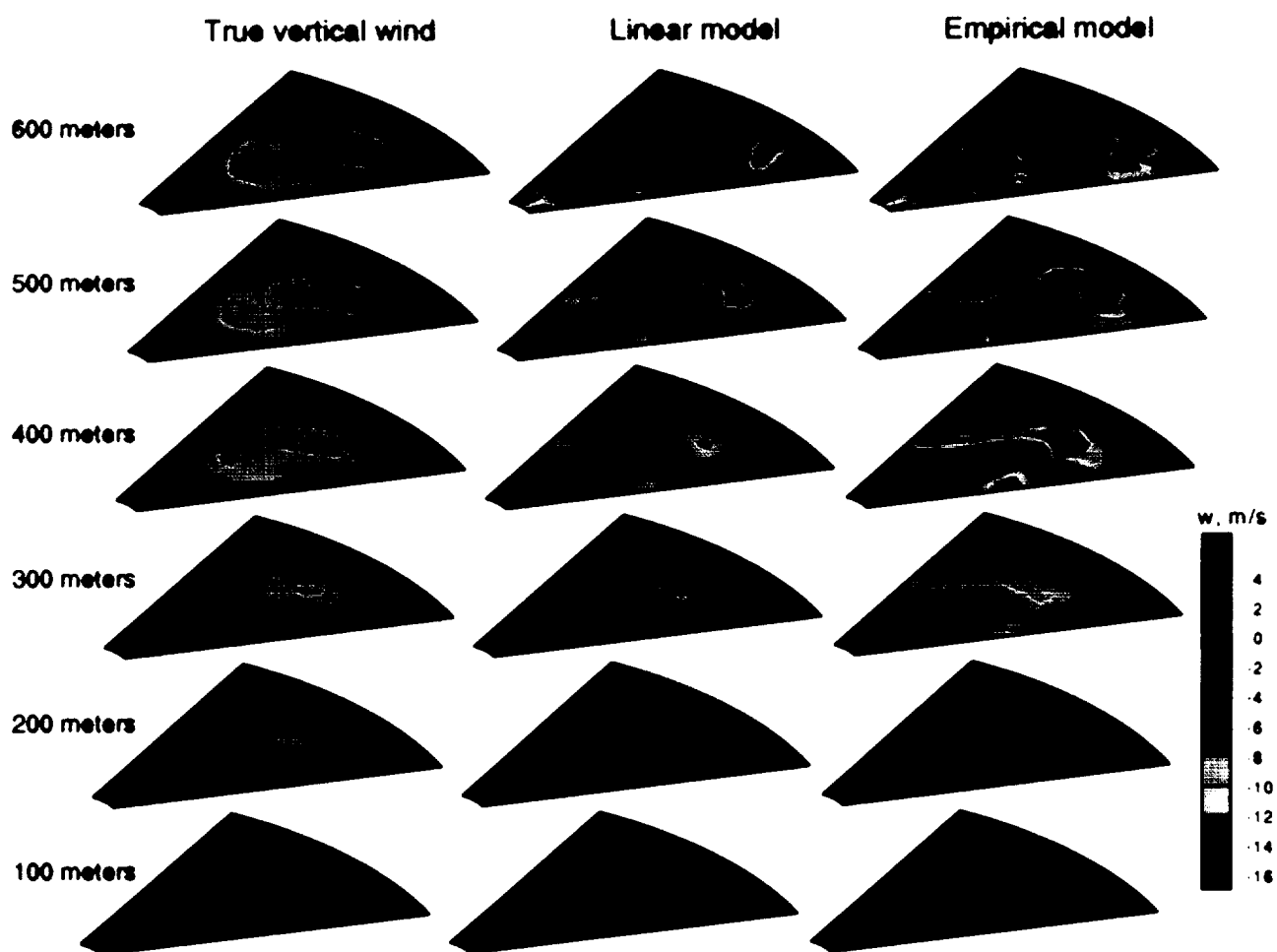
(b) $t = 50$ min.

Figure 20. Continued.
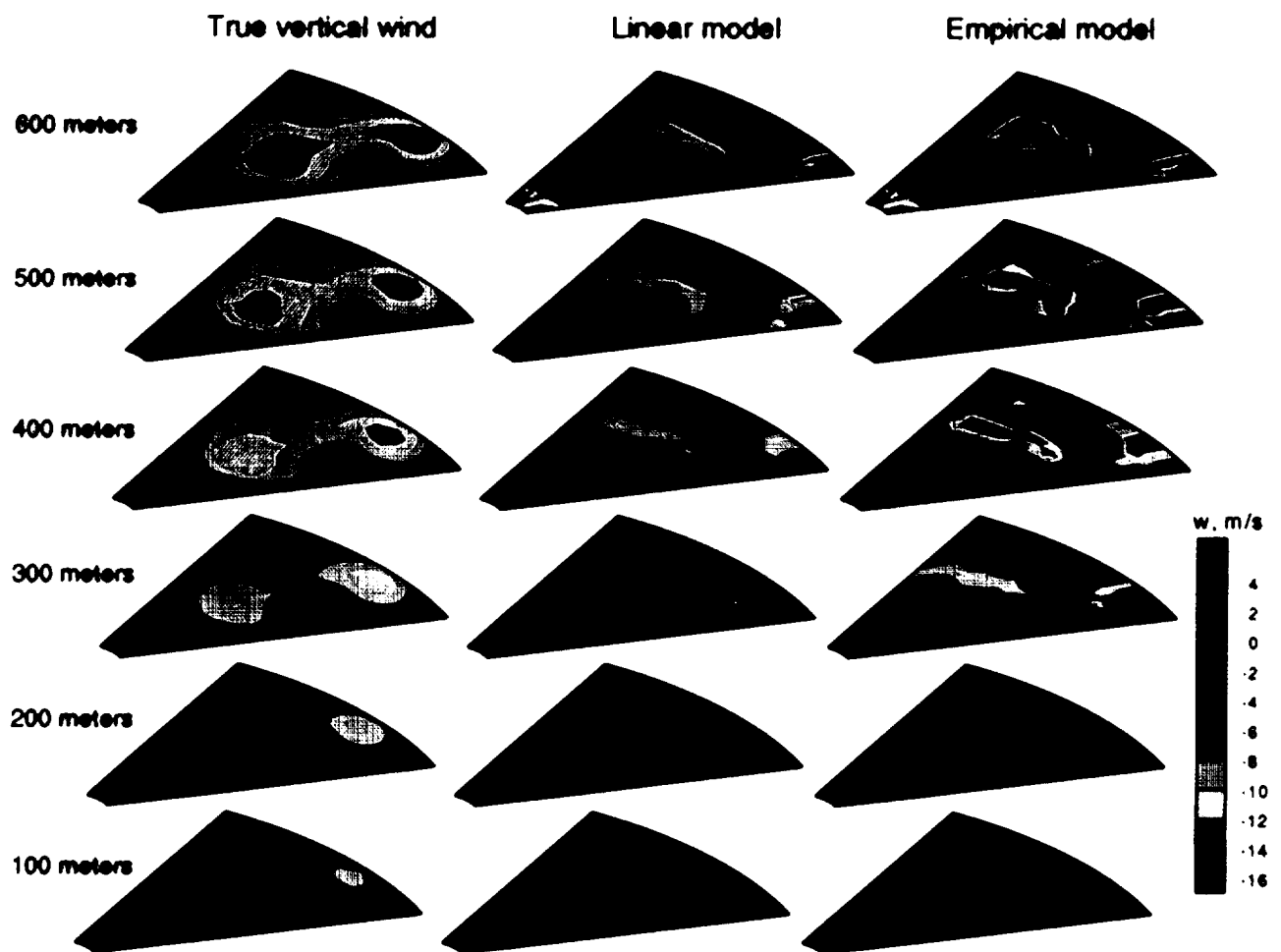
Figure 20. Concluded.

(c) $t = 51$ min.
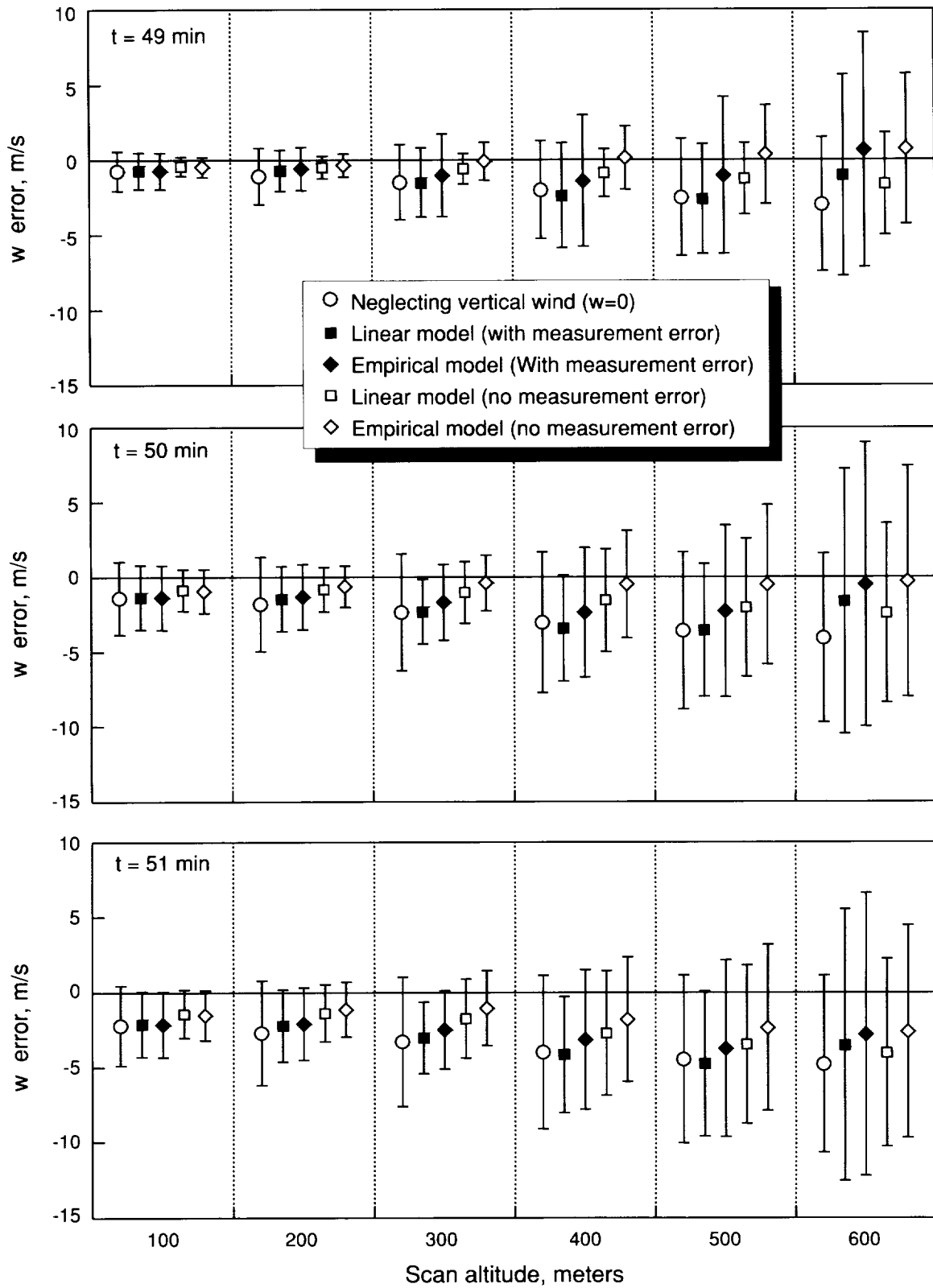
Figure 21. Mean and standard deviation of vertical wind estimate error at each scan altitude for asymmetric microburst case.
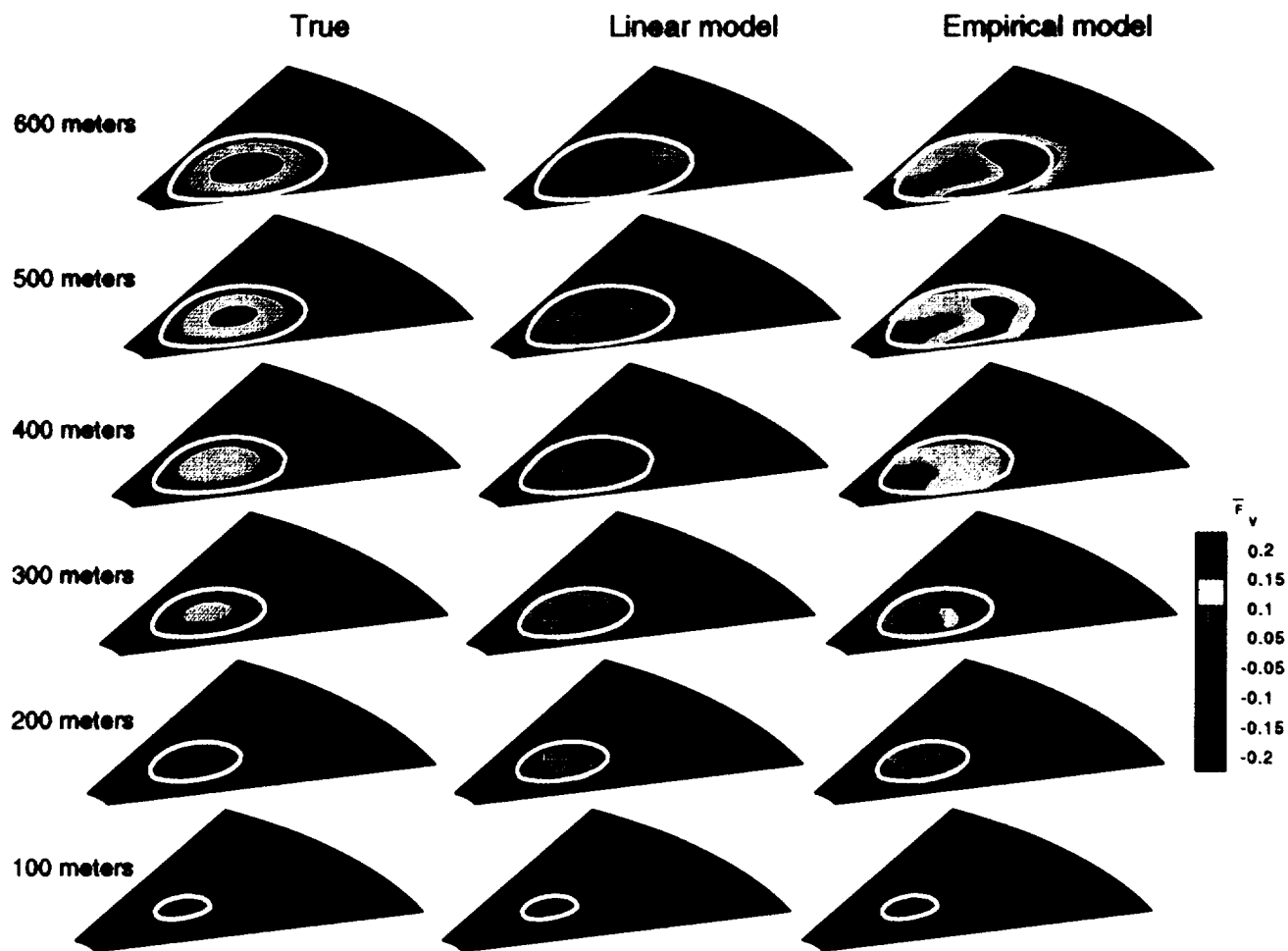
(a) $t = 49$ min.

Figure 22. True $\overline{F}_v$ and $\overline{F}_v$ computed from linear and empirical models without radar measurement errors at six scan altitudes for asymmetric microburst case.
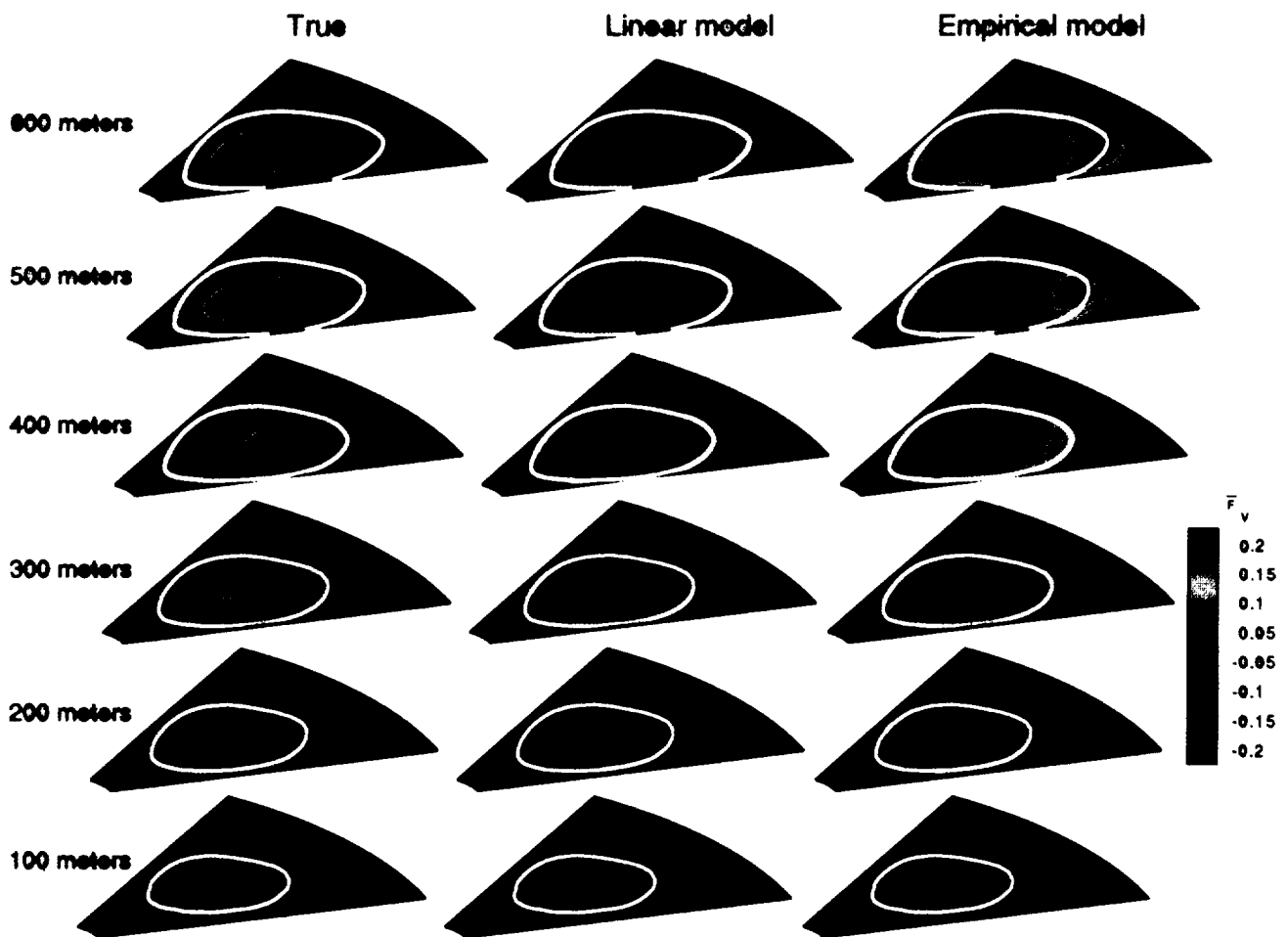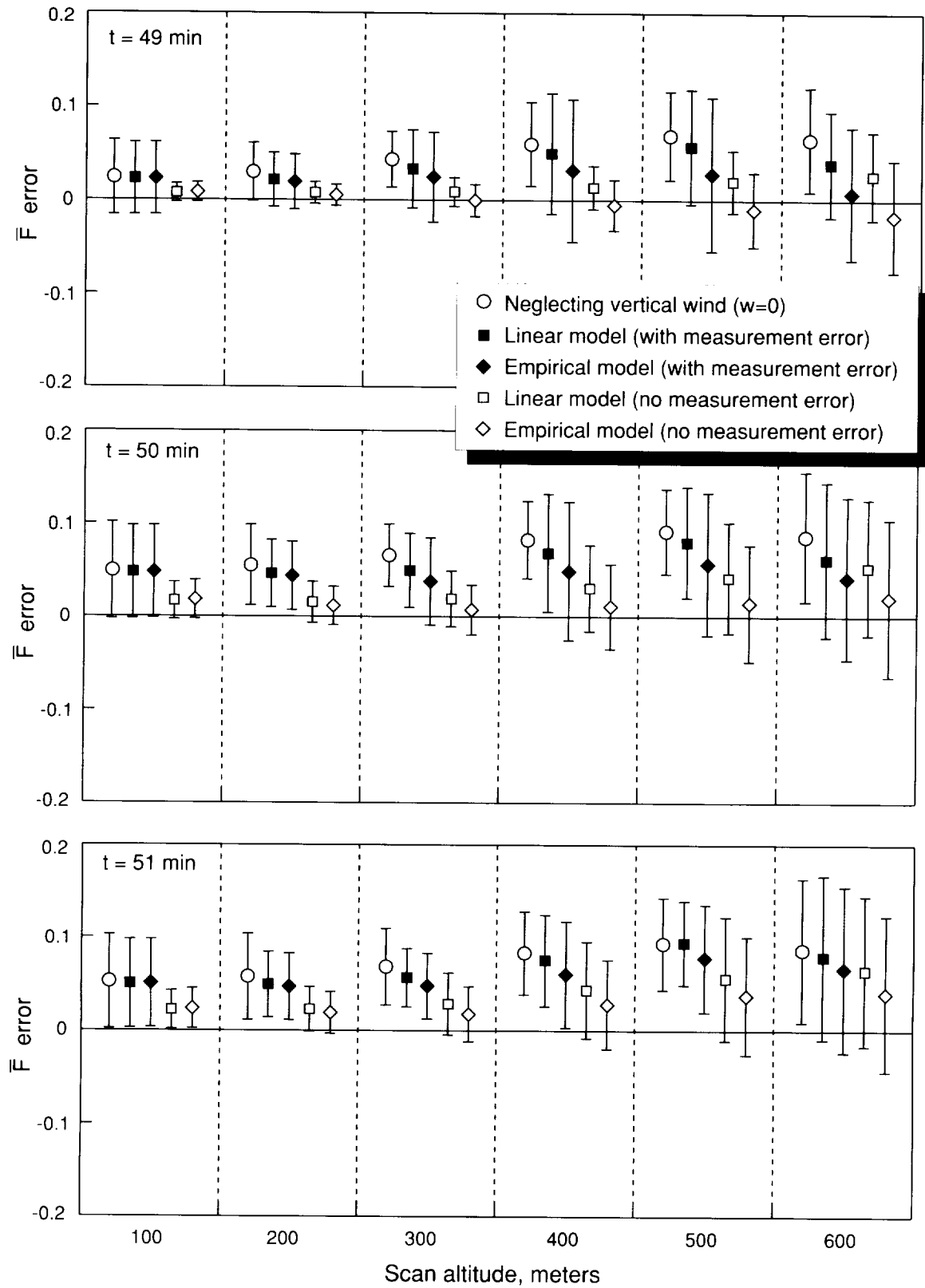
(b) $t = 50$ min.

Figure 22. Continued.

True   Linear model   Empirical model
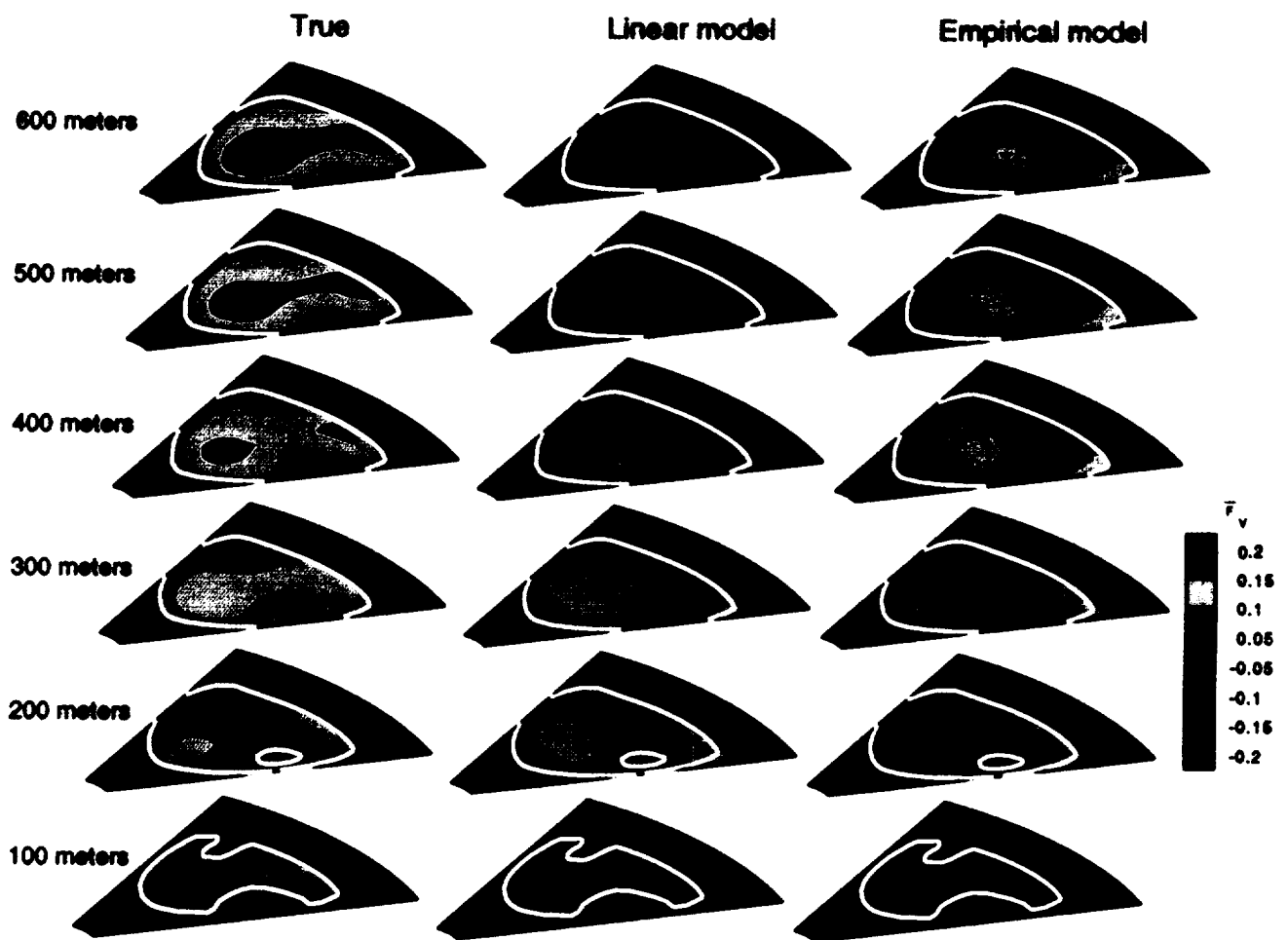
(c) $t = 51$ min.

Figure 22. Concluded.

True   Linear model   Empirical model

600 meters

500 meters

400 meters

300 meters

200 meters

100 meters

$\overline{F}_v$

0.2
0.15
0.1
0.05
-0.05
-0.1
-0.15
-0.2
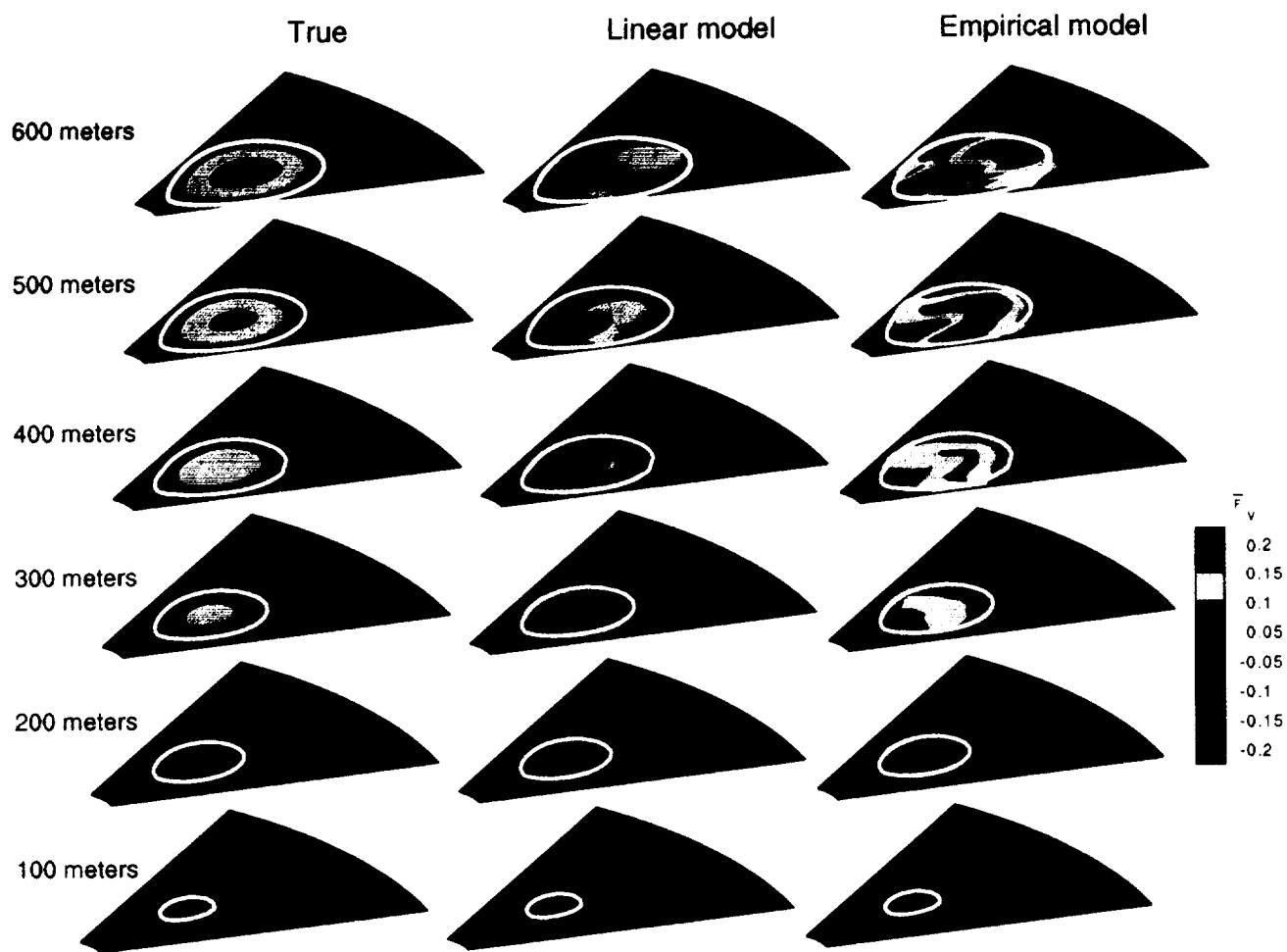
(a) $t = 49$ min.

Figure 23. True $\overline{F}_v$ and $\overline{F}_v$ computed from linear and empirical models with radar measurement errors at six scan altitudes for asymmetric microburst case.
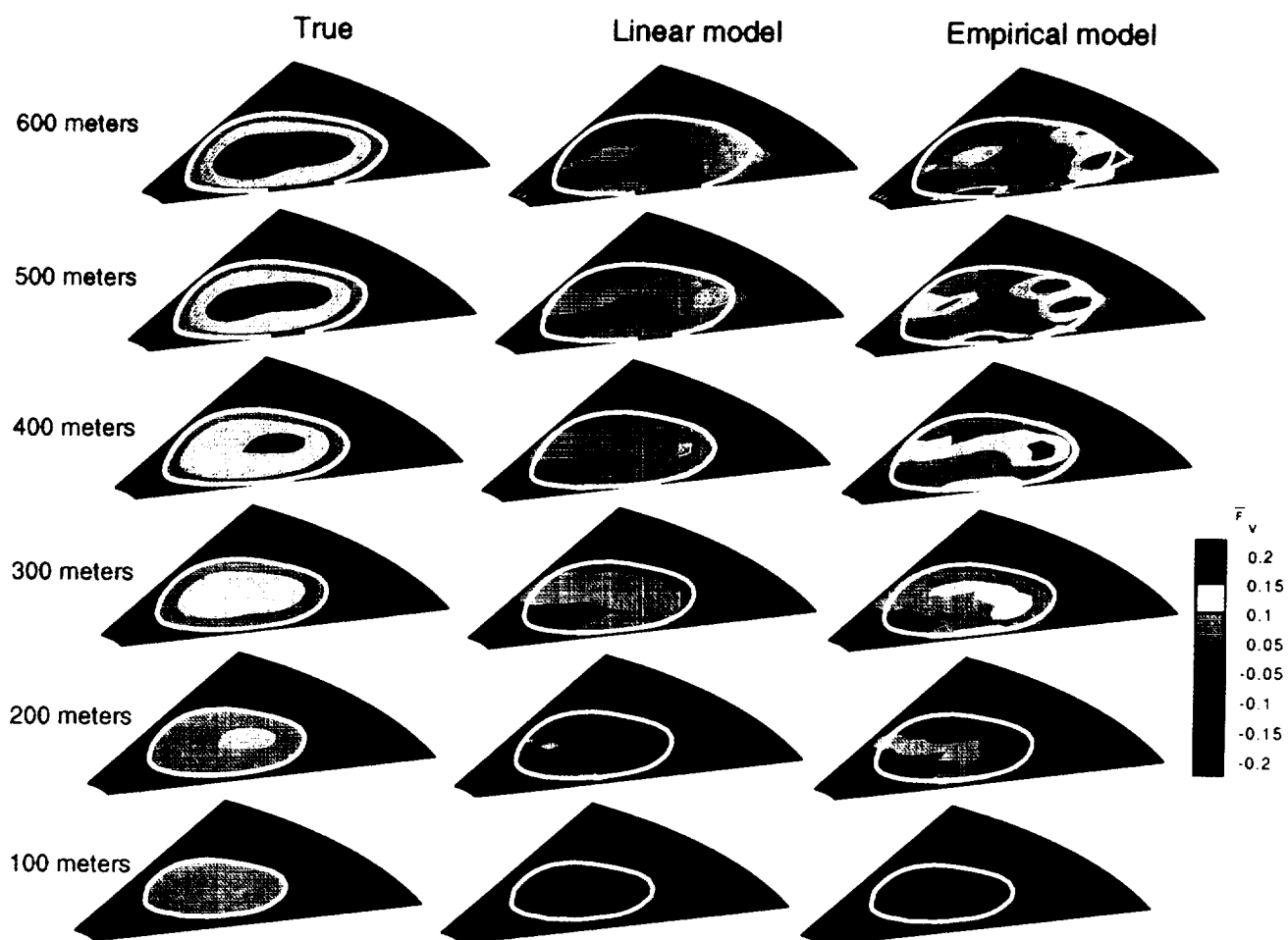
(b) $t = 50$ min.

Figure 23. Continued.
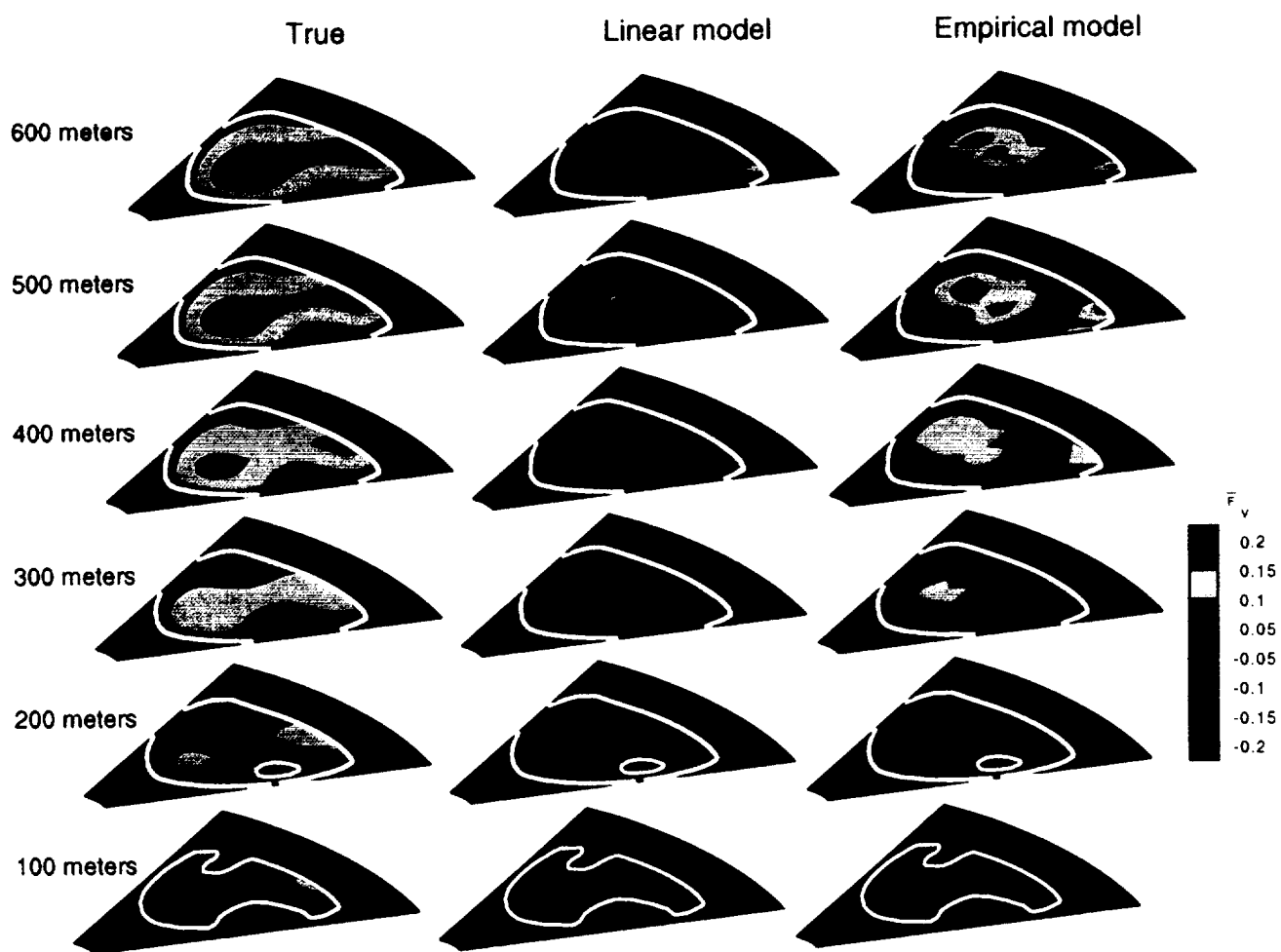
(c) $t = 51$ min.

Figure 23. Concluded.

58
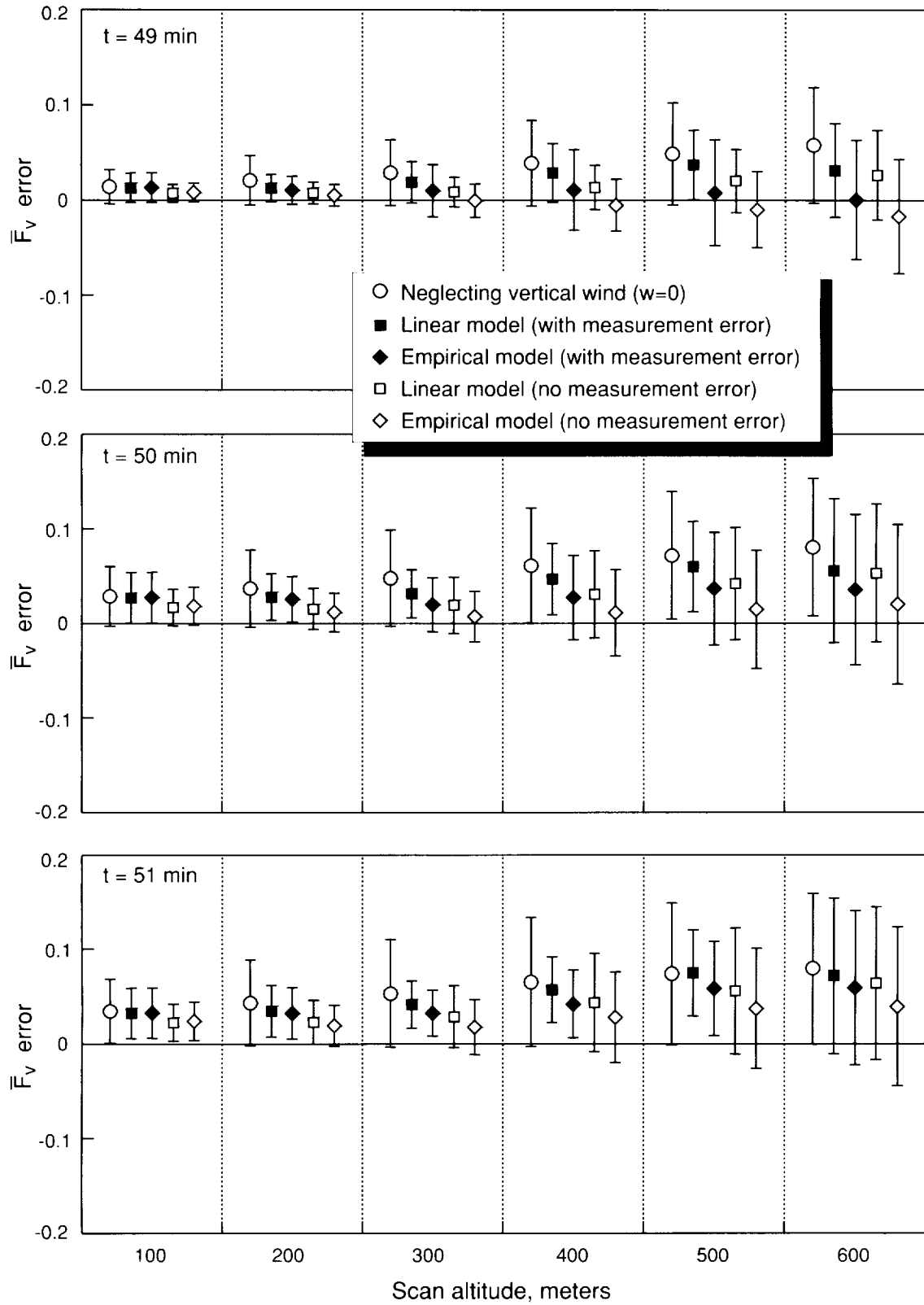
Figure 24. Mean and standard deviation of error in $\overline{F}_v$ for asymmetric microburst case.
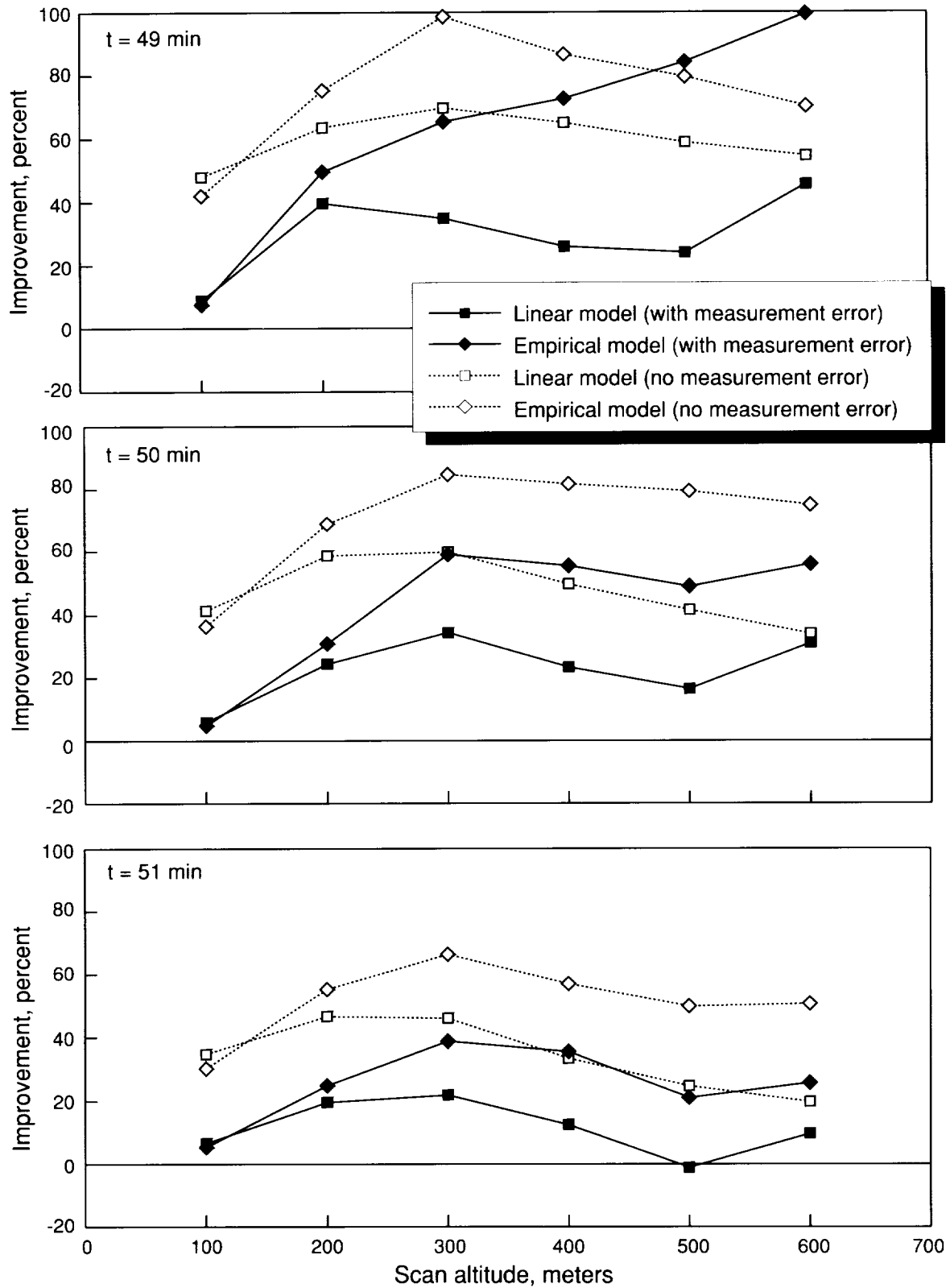
Figure 25. Improvement in $\overline{F}_v$ mean error.
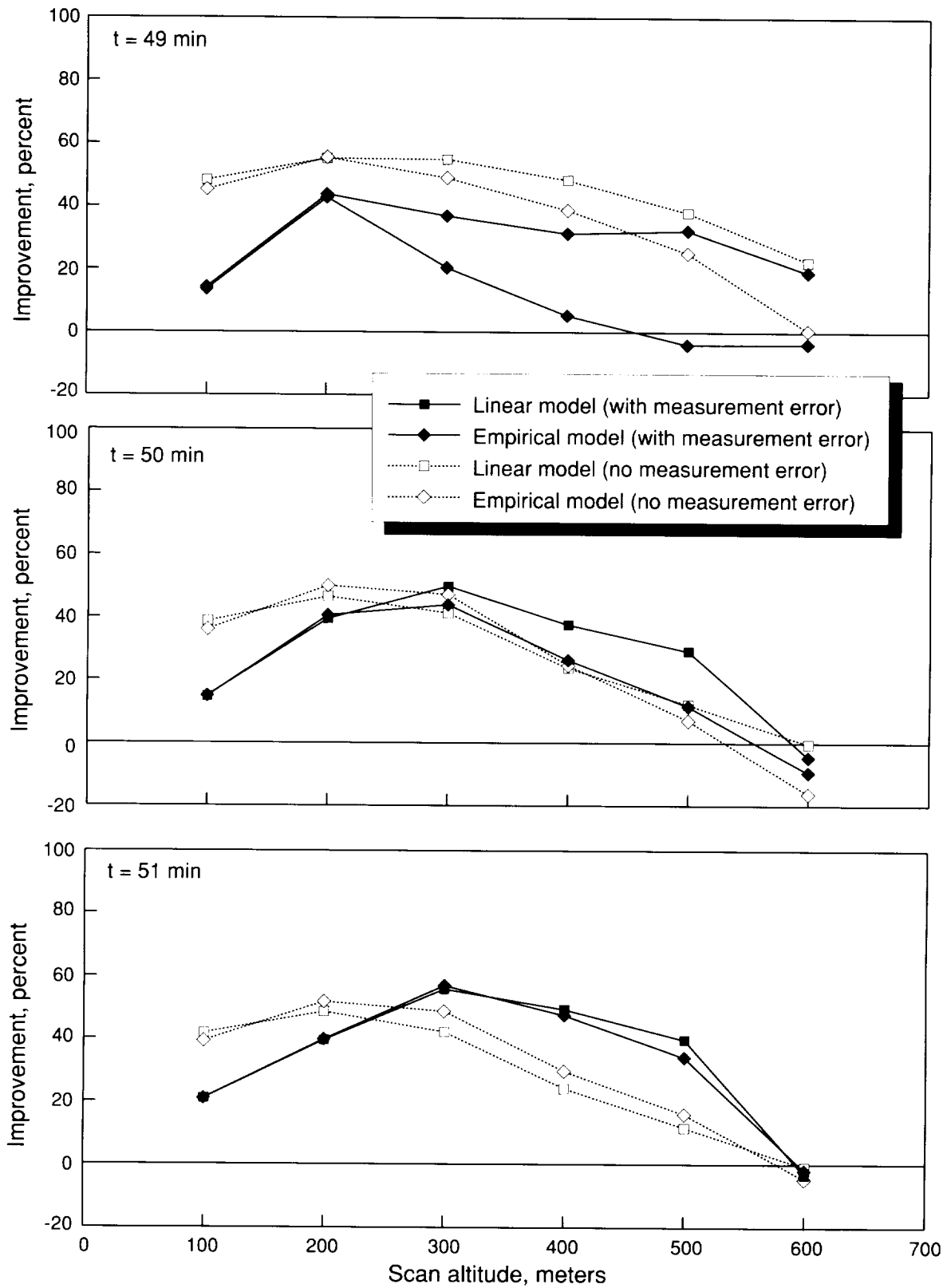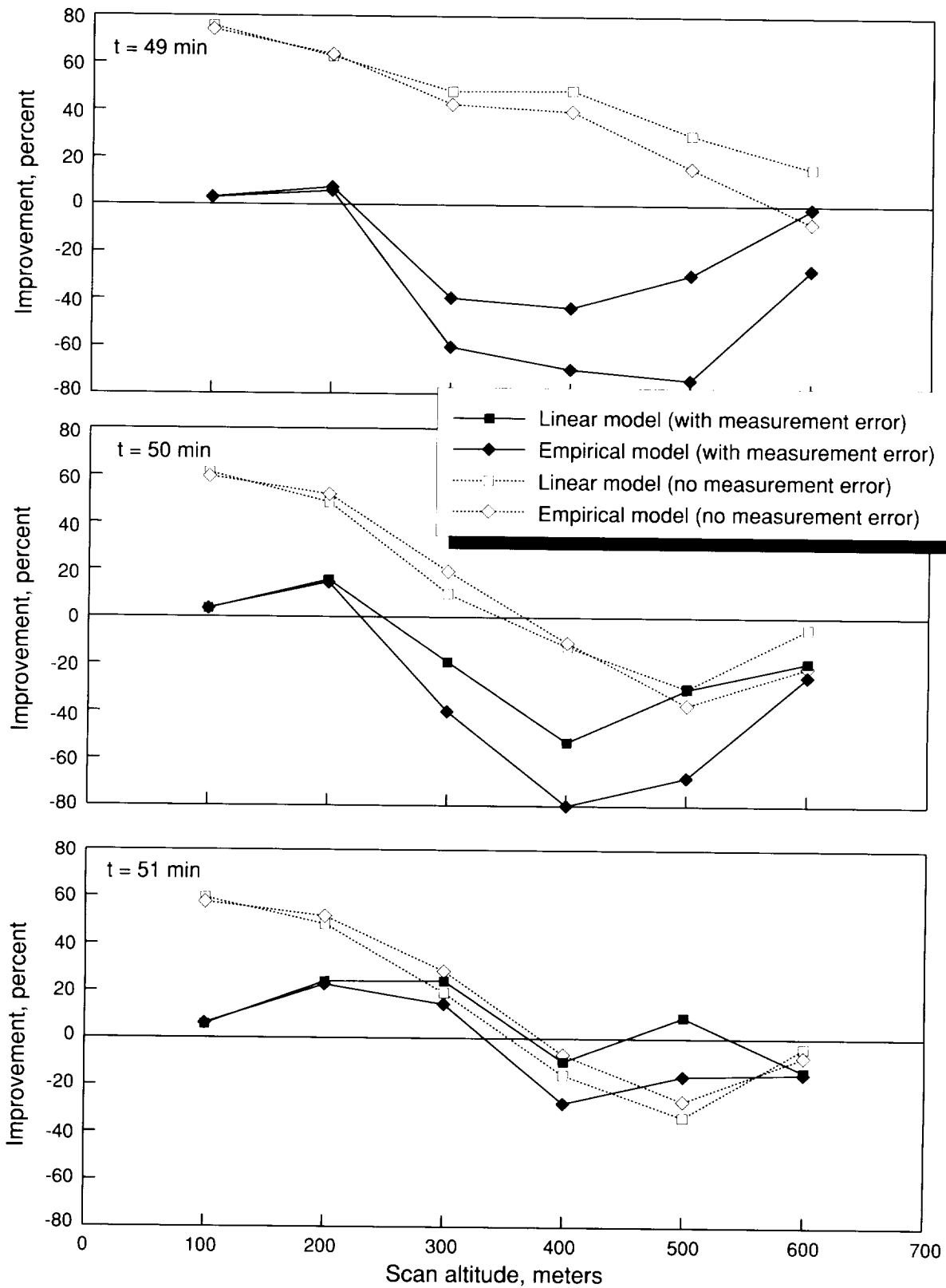
Figure 26. Improvement in $\overline{F}_v$ error standard deviation.
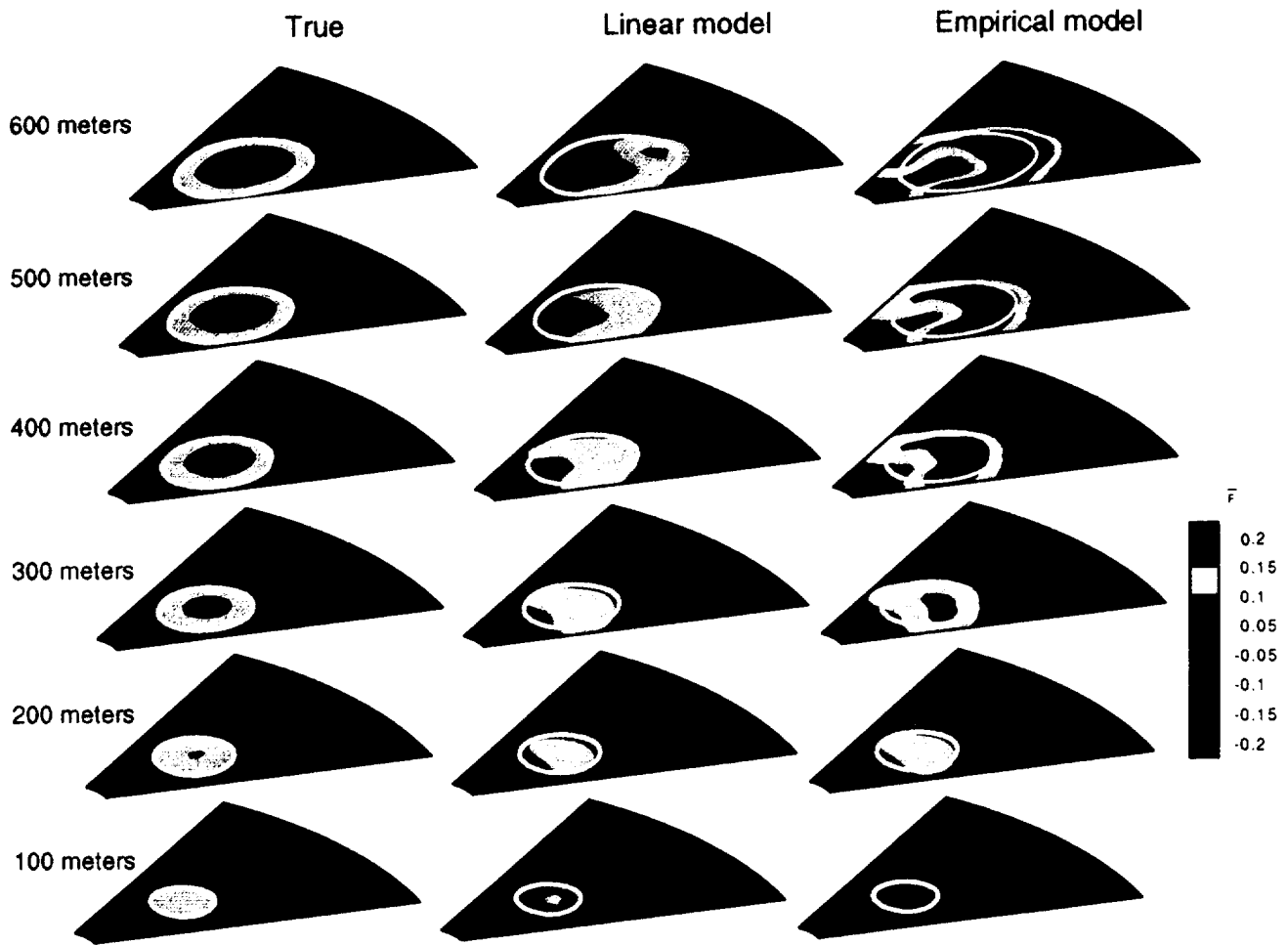
(a) $t = 49$ min.

Figure 27. The $\overline{F}$ true and $\overline{F}$ computed from linear and empirical models without radar measurement errors at six scan altitudes for asymmetric microburst case.

True Linear model Empirical model

600 meters

500 meters

400 meters

300 meters

200 meters

100 meters

$\bar{F}$

0.2
0.15
0.1
0.05
-0.05
-0.1
-0.15
-0.2
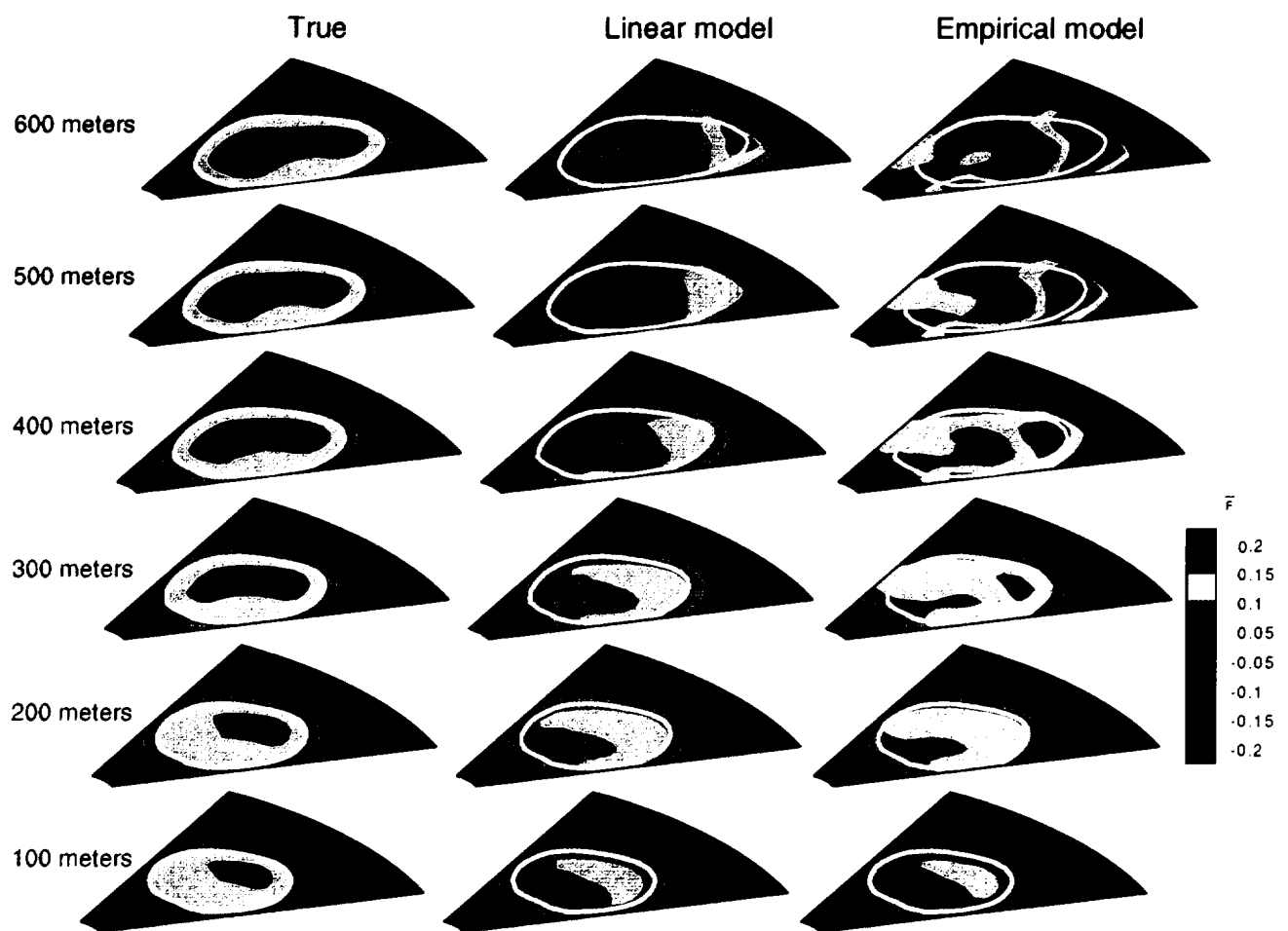
(b) $t = 50$ min.

Figure 27. Continued.

True　　　　Linear model　　　Empirical model

600 meters

500 meters

400 meters

300 meters

200 meters

100 meters

$\bar{F}$

0.2
0.15
0.1
0.05
-0.05
-0.1
-0.15
-0.2
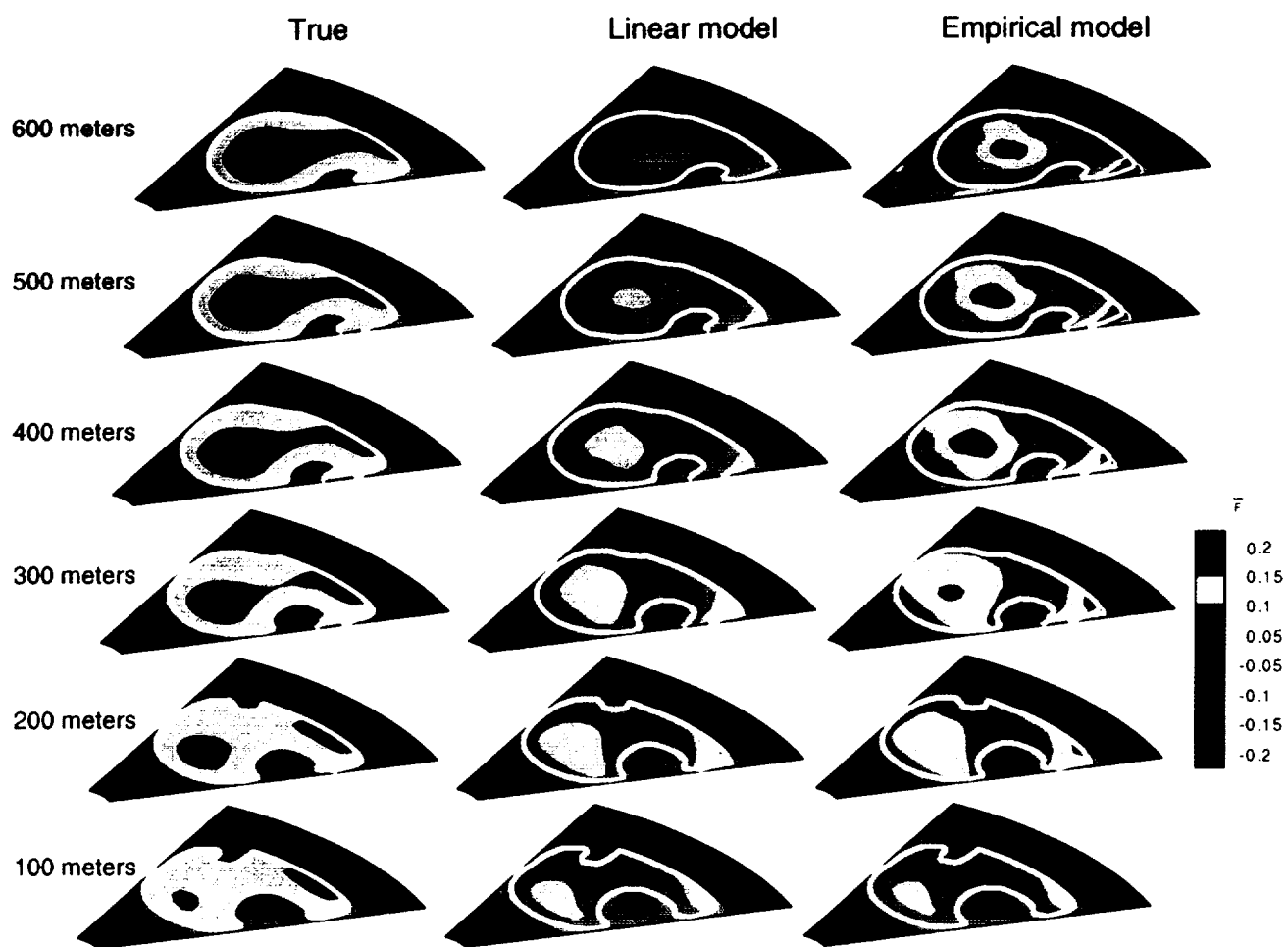
(c) $t = 51$ min.

Figure 27. Concluded.

$\overline{F}$ $\overline{F}_h$ $\overline{F}_v$

600 meters

500 meters

400 meters

300 meters

200 meters

100 meters

$\overline{F}$

0.2
0.15
0.1
0.05
-0.05
-0.1
-0.15
-0.2

(a) $t = 49$ min.

Figure 28. True $\overline{F}, \overline{F}_h$, and $\overline{F}_v$ at six scan altitudes for asymmetric microburst case.
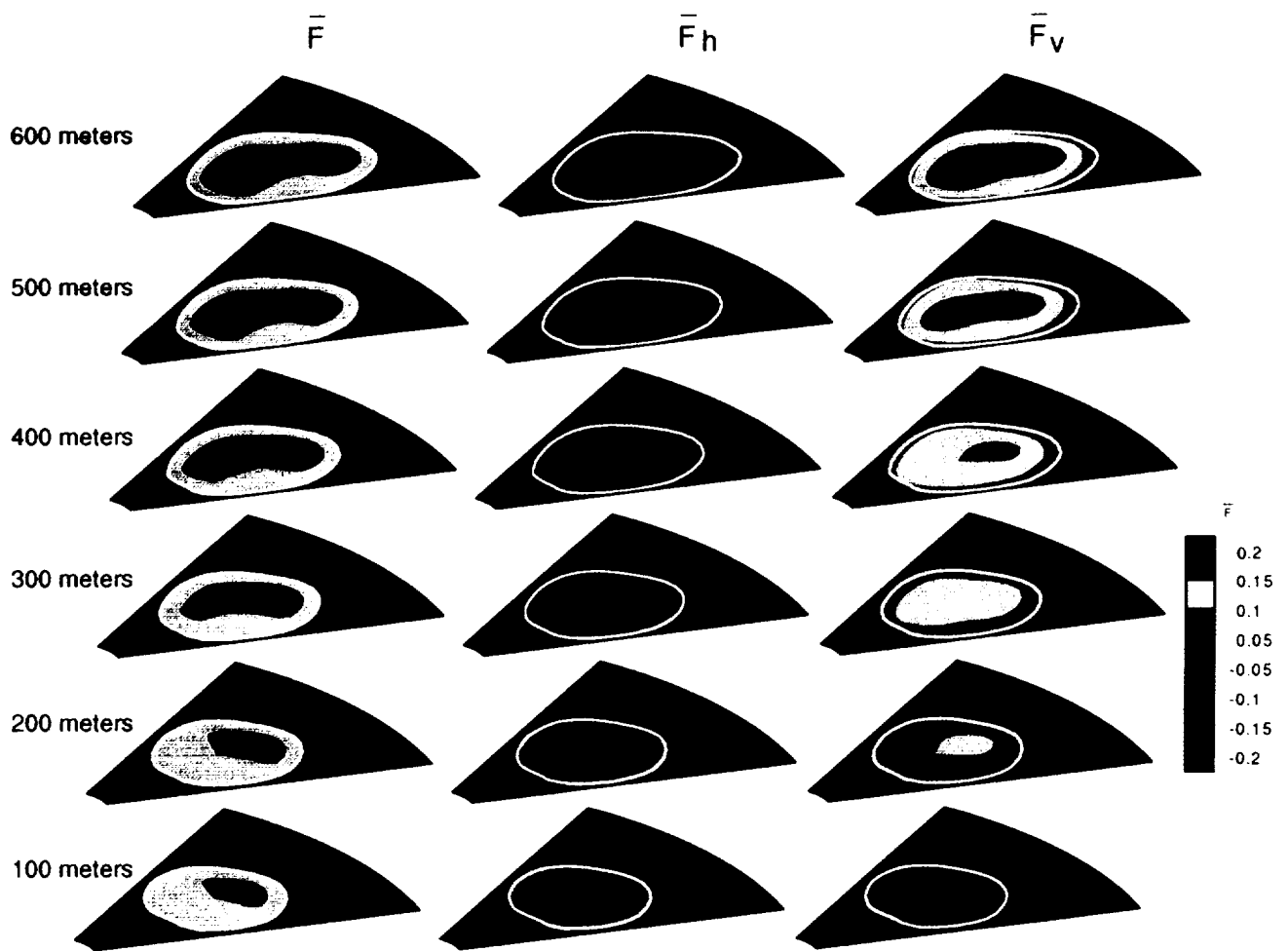
(b) $t = 50$ min.

Figure 28. Continued.
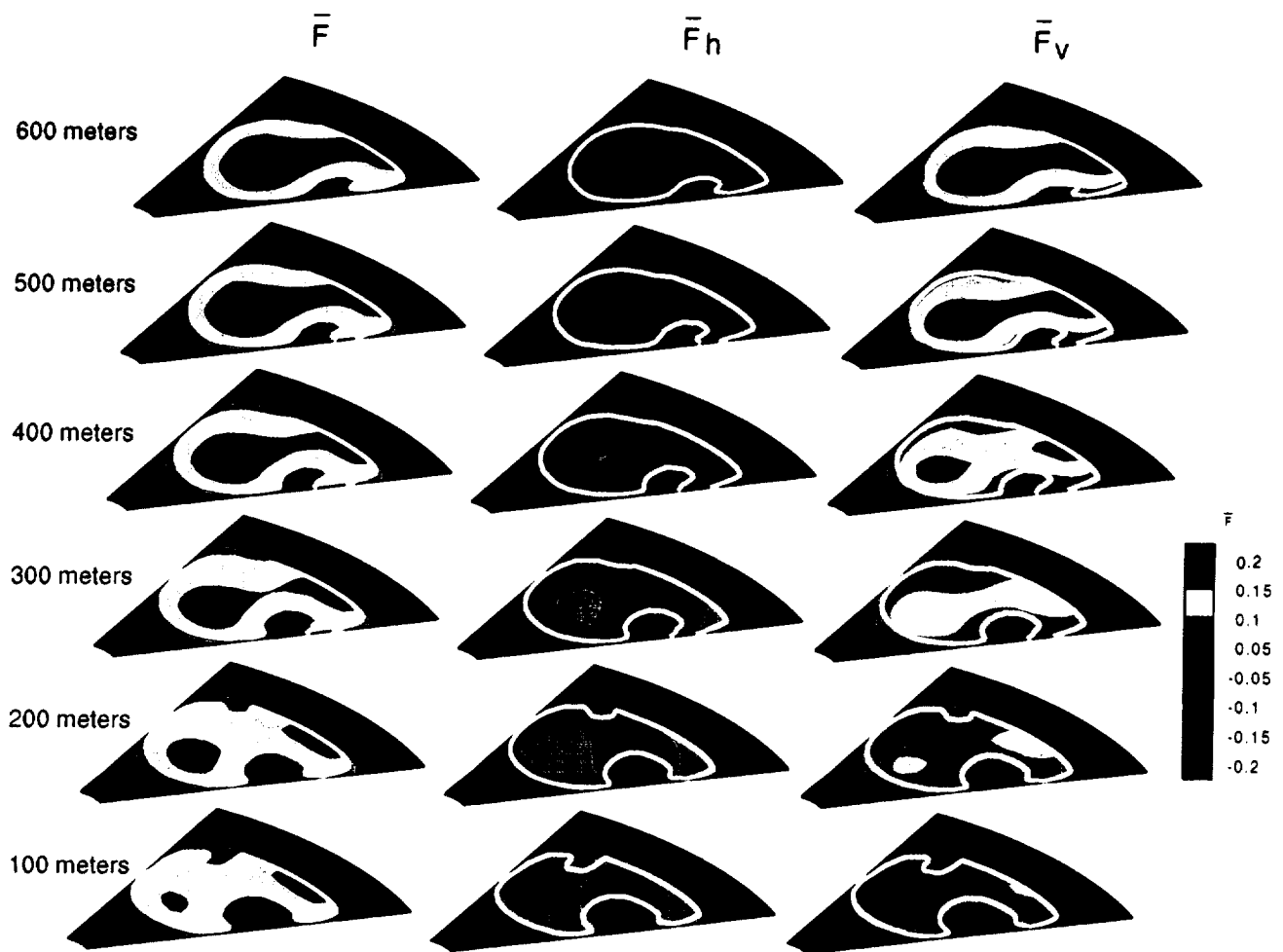
(c) $t = 51$ min.

Figure 28. Concluded.

67

True   Linear model   Empirical model

600 meters

500 meters

400 meters

300 meters

200 meters

100 meters
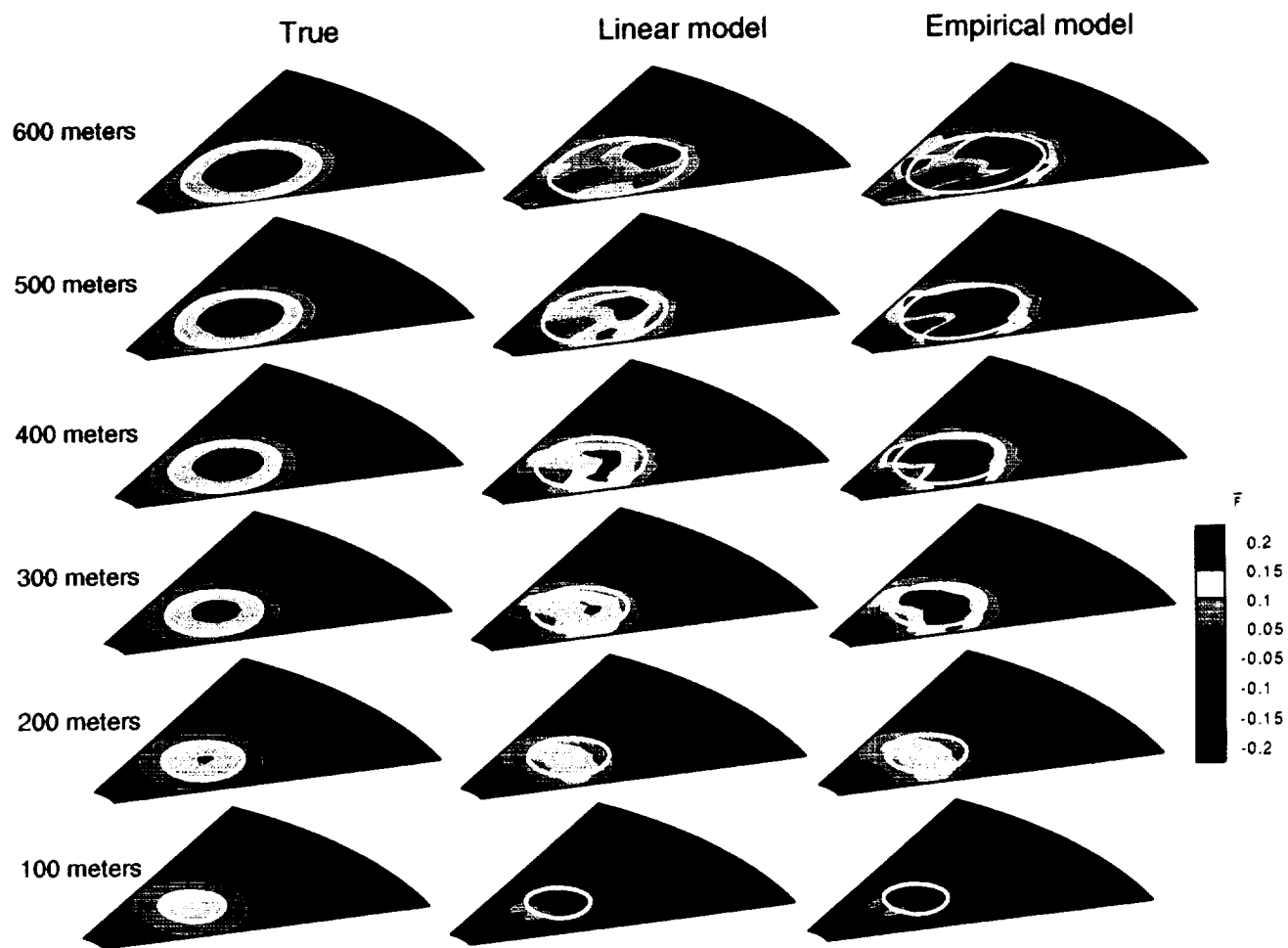
(a) $t = 49$ min.

Figure 29. True $\overline{F}$ and $\overline{F}$ computed from linear and empirical models with radar measurement errors at six scan altitudes for asymmetric microburst case.

	True	Linear model	Empirical model
600 meters			
500 meters			
400 meters			
300 meters			
200 meters			
100 meters			

$\bar{F}$

0.2
0.15
0.1
0.05
-0.05
-0.1
-0.15
-0.2
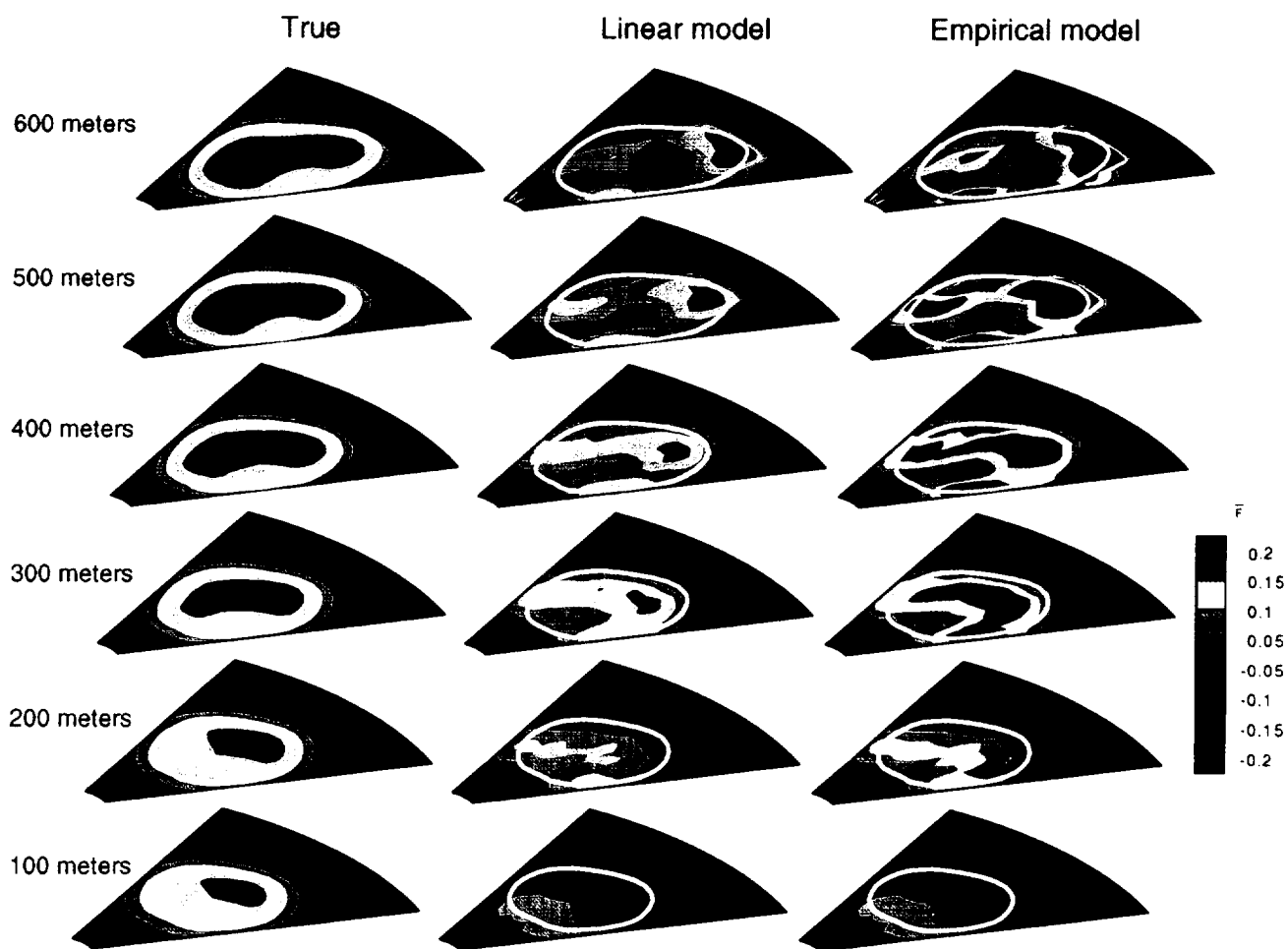
(b) $t = 50$ min.

Figure 29. Continued.

True   Linear model   Empirical model

600 meters

500 meters

400 meters

300 meters

200 meters

100 meters
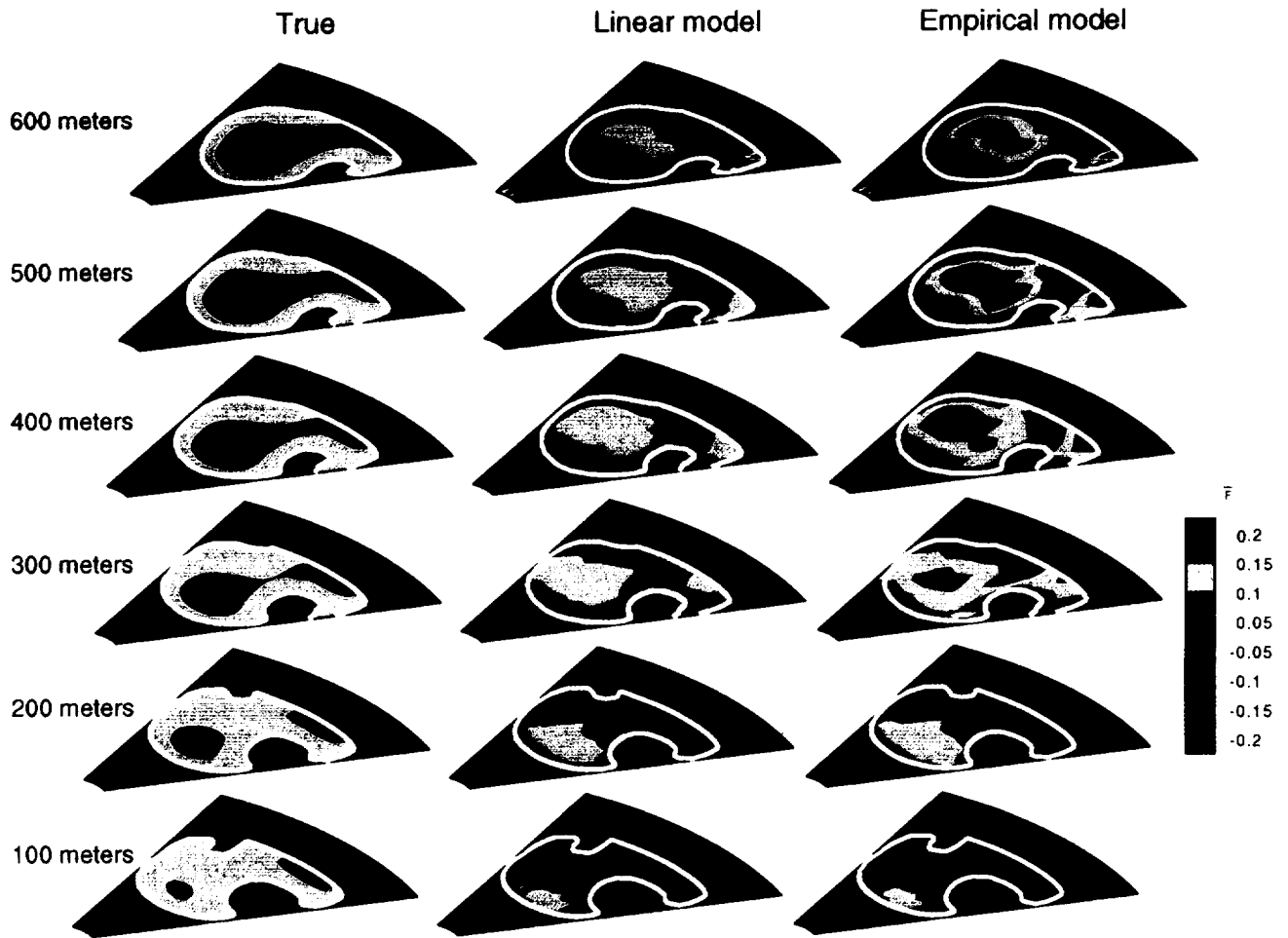
(c) $t = 51$ min.

Figure 29. Concluded.

70

Figure 30. Mean and standard deviation of error in $\overline{F}$ for asymmetric microburst case.
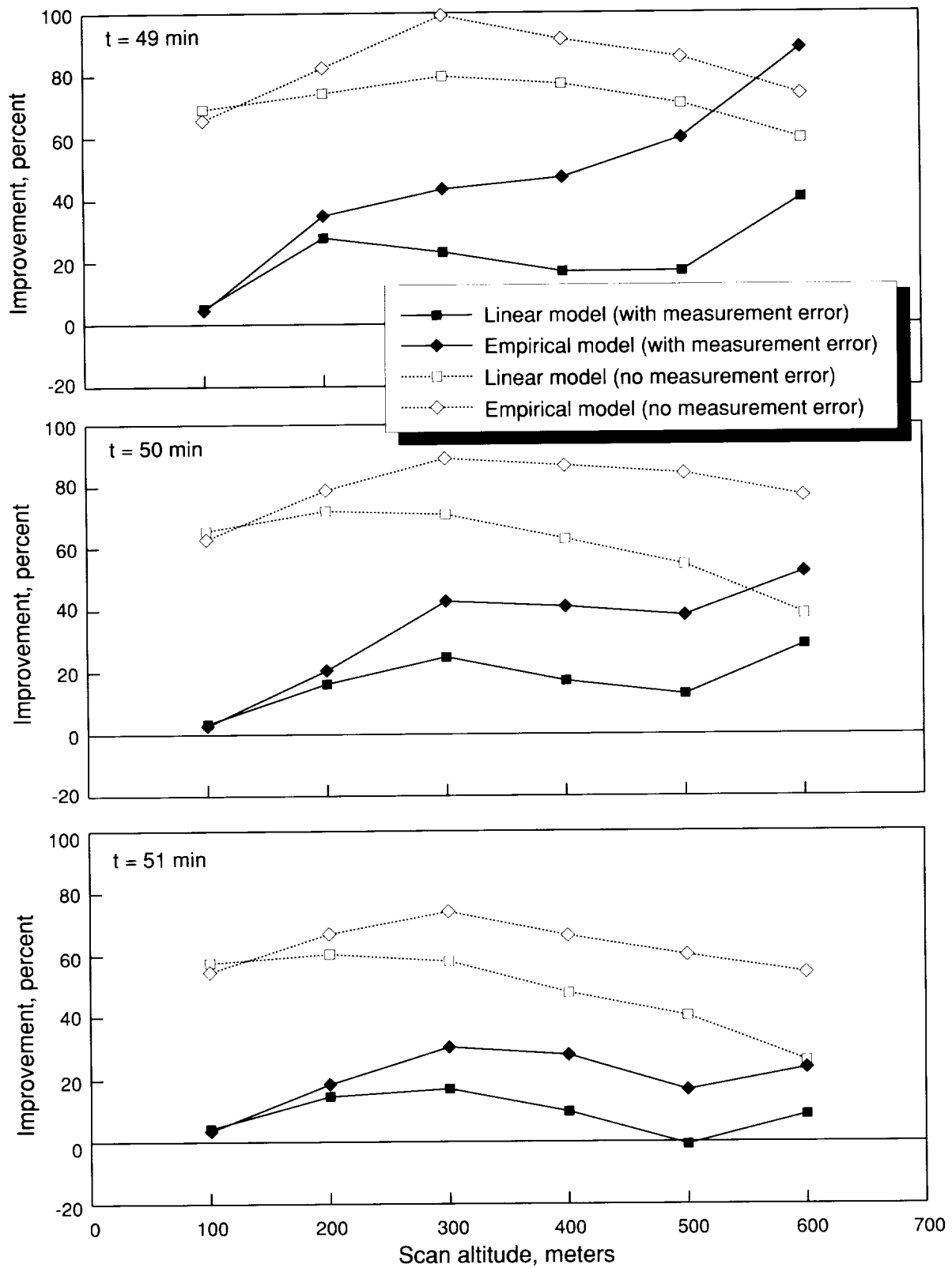
Figure 31. Improvement in $\overline{F}$ mean error.

Figure 32. Improvement in $\overline{F}$ error standard deviation.
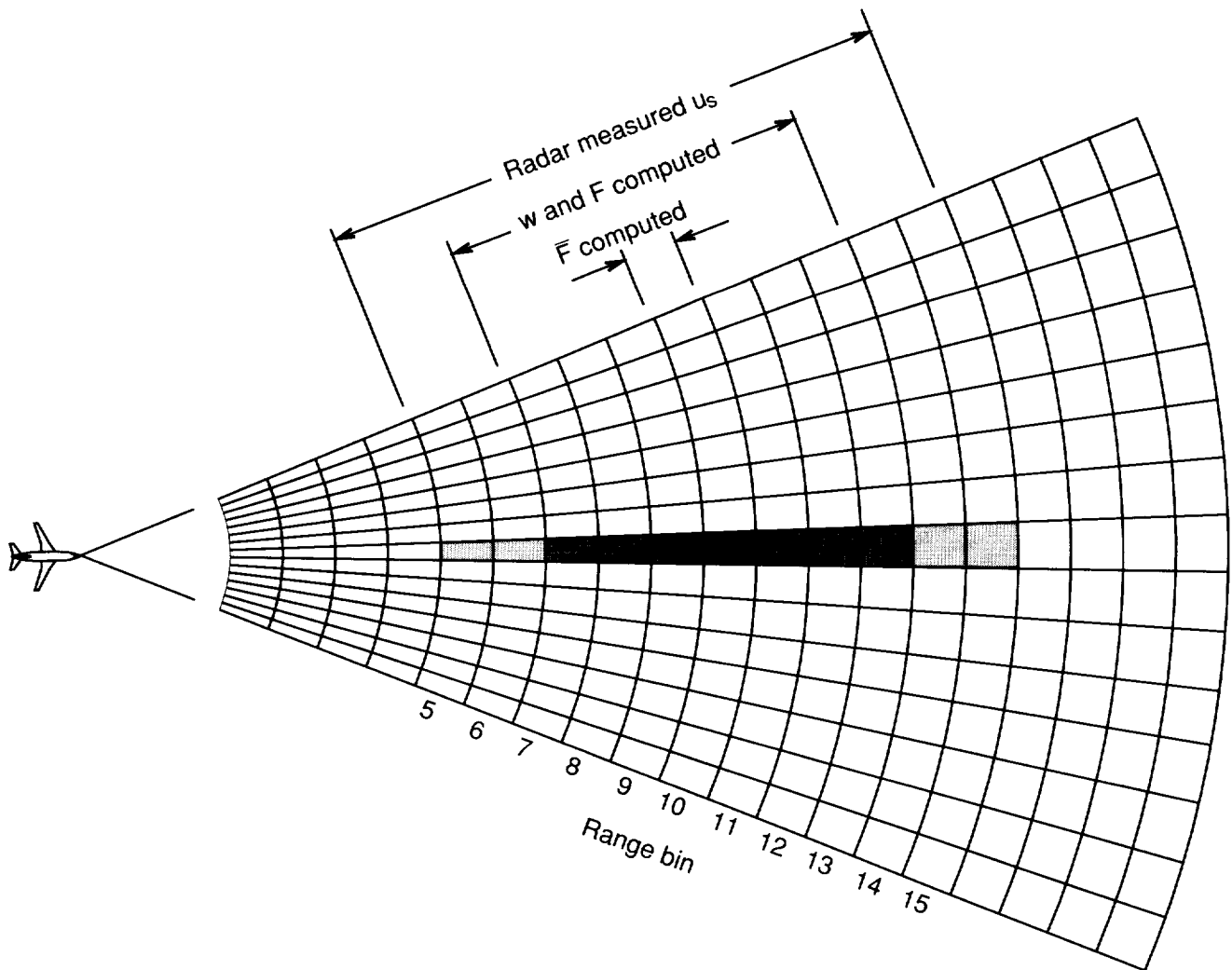
Figure 33. Radar range bins used in flight data analysis.
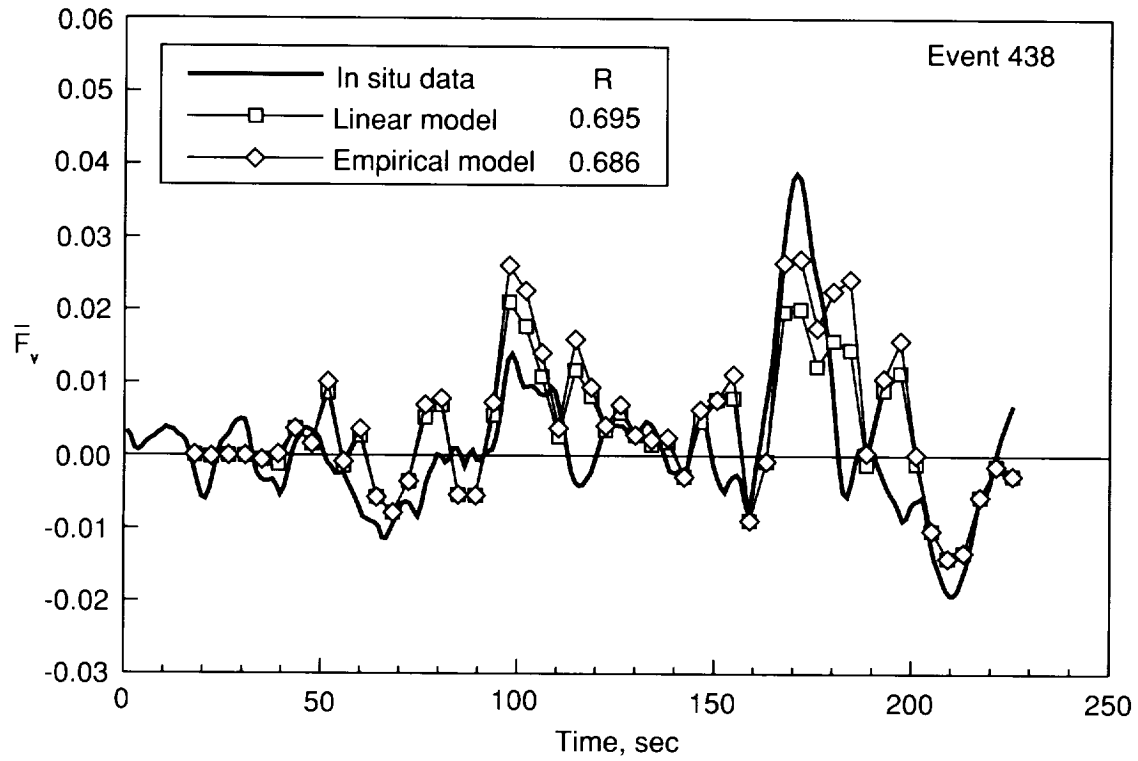
(a) Event 438.
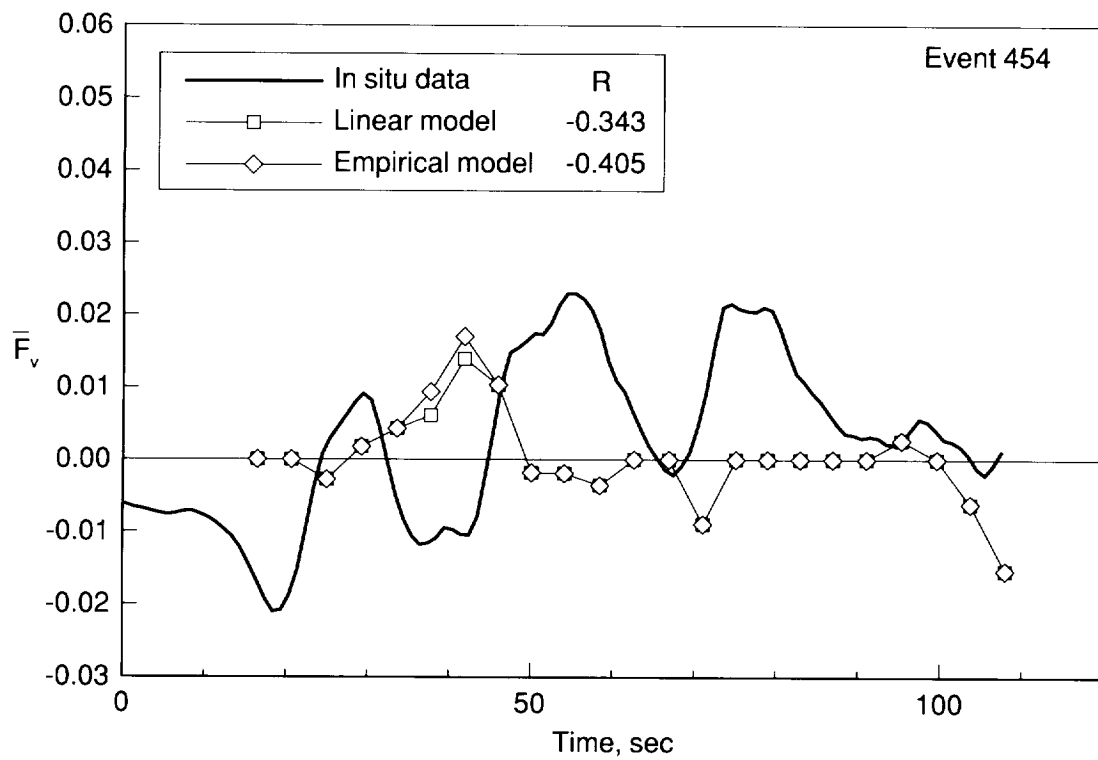
(b) Event 454.

Figure 34. Estimated $\overline{F}$ and in situ measured $\overline{F}_v$ time histories with corresponding R.
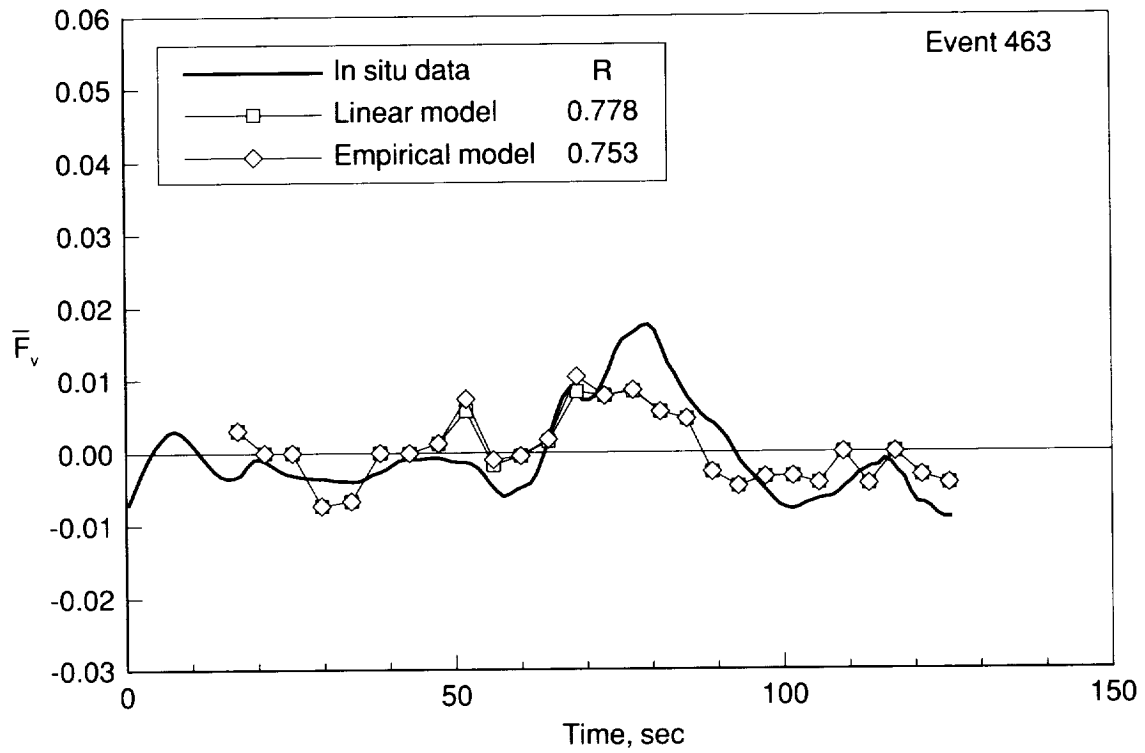
(c) Event 463.
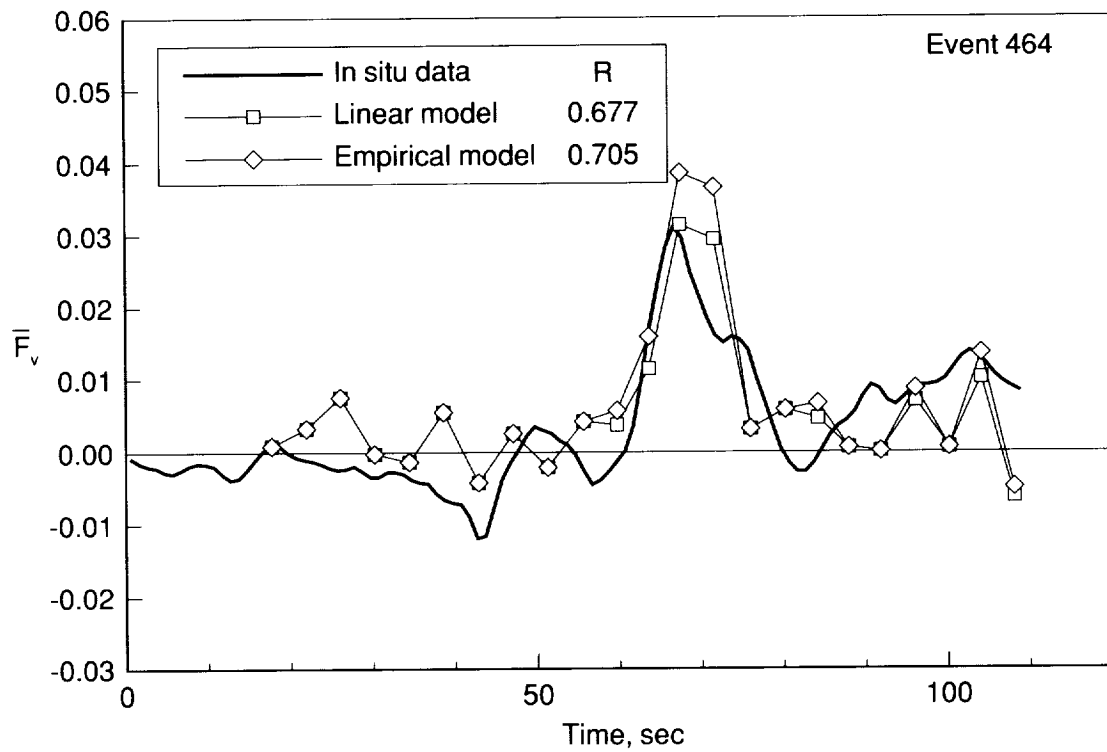
(d) Event 464.

Figure 34. Continued.
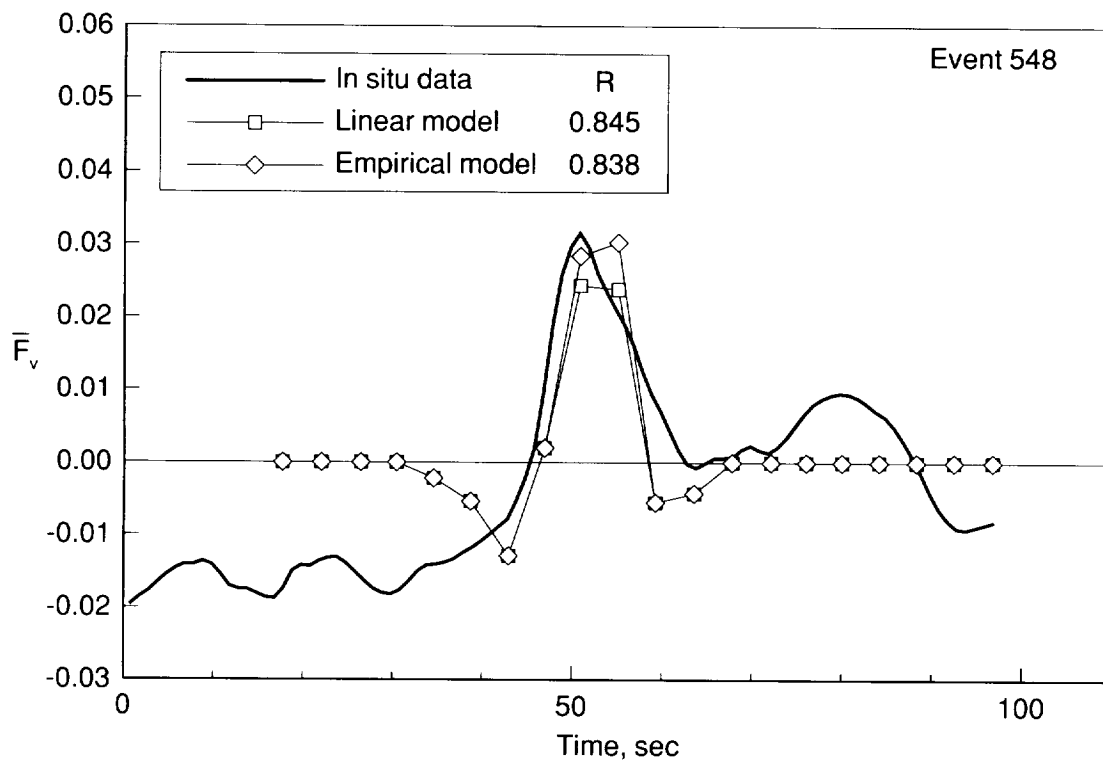
(e) Event 548.
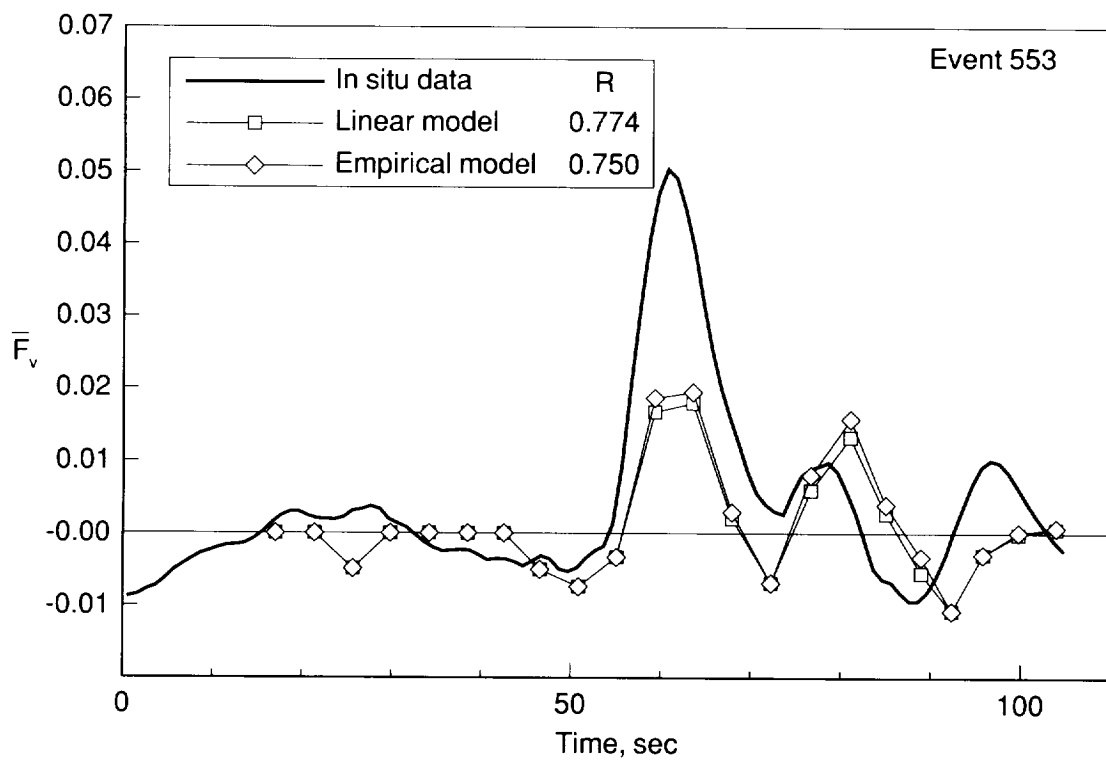
(f) Event 553.

Figure 34. Continued.
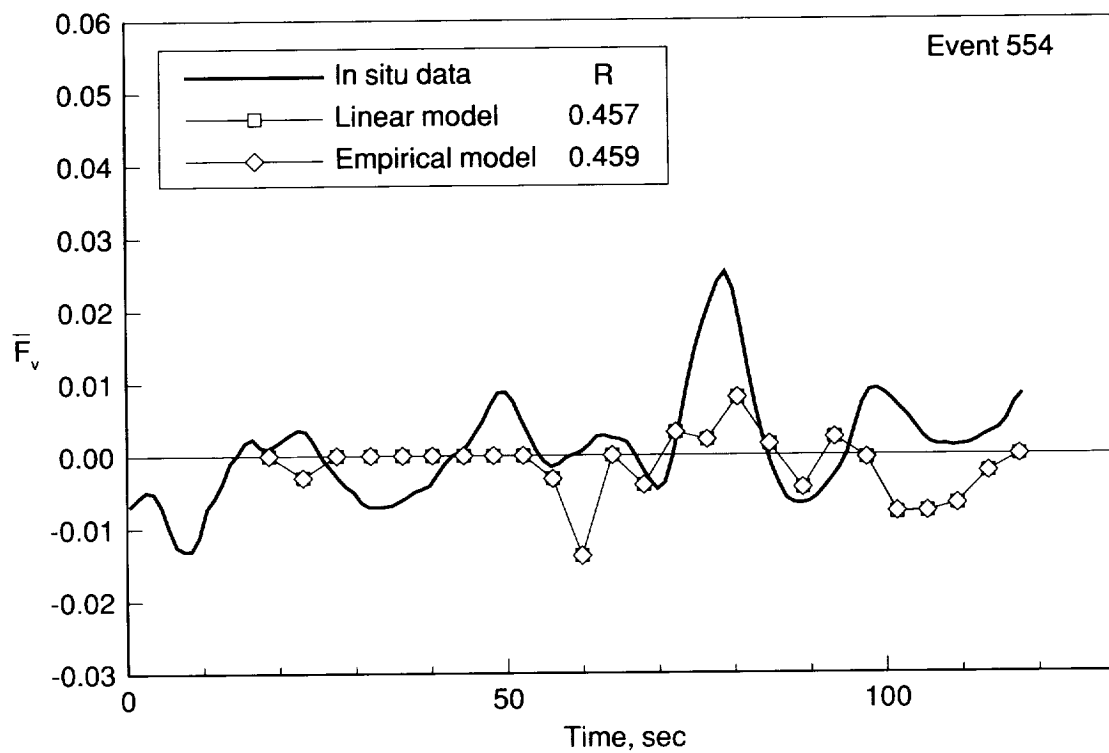
(g) Event 554.
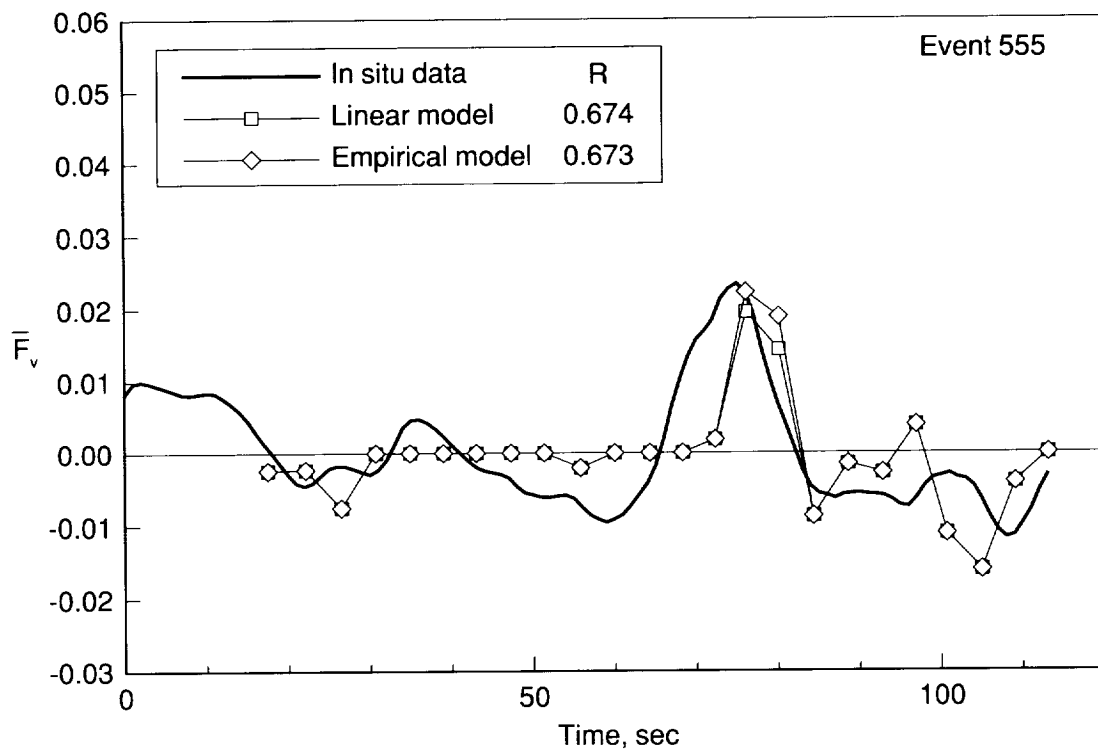
(h) Event 555.

Figure 34. Continued.
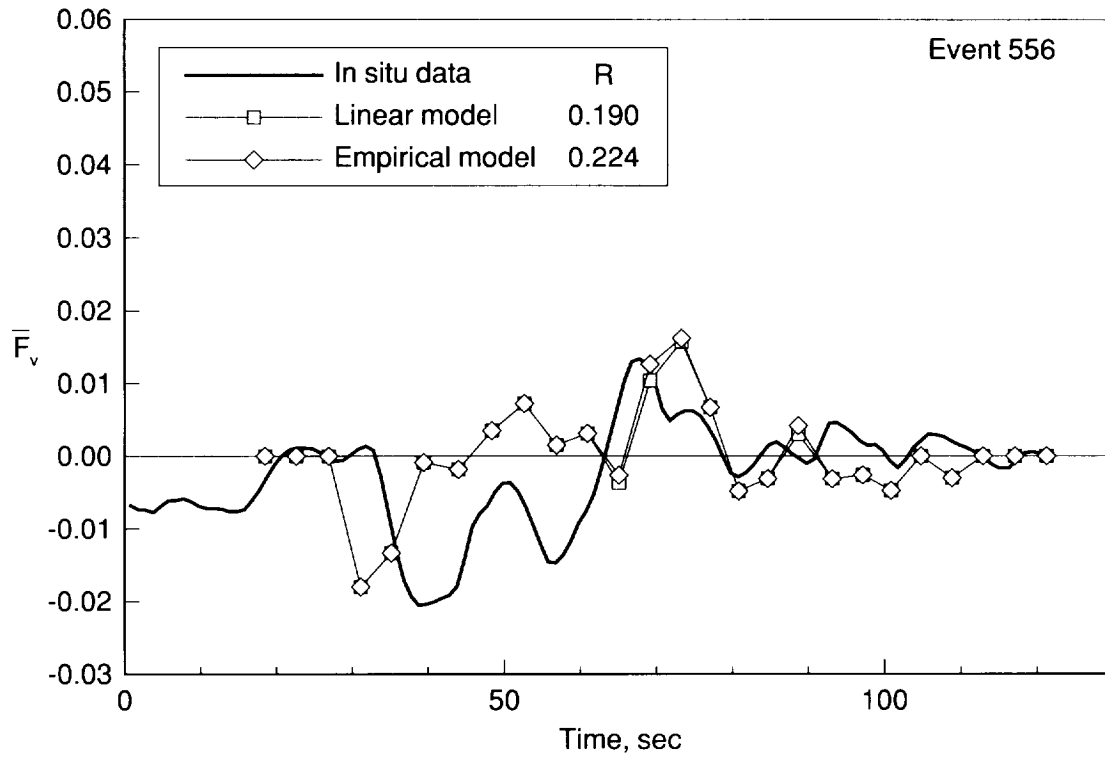
(i) Event 556.
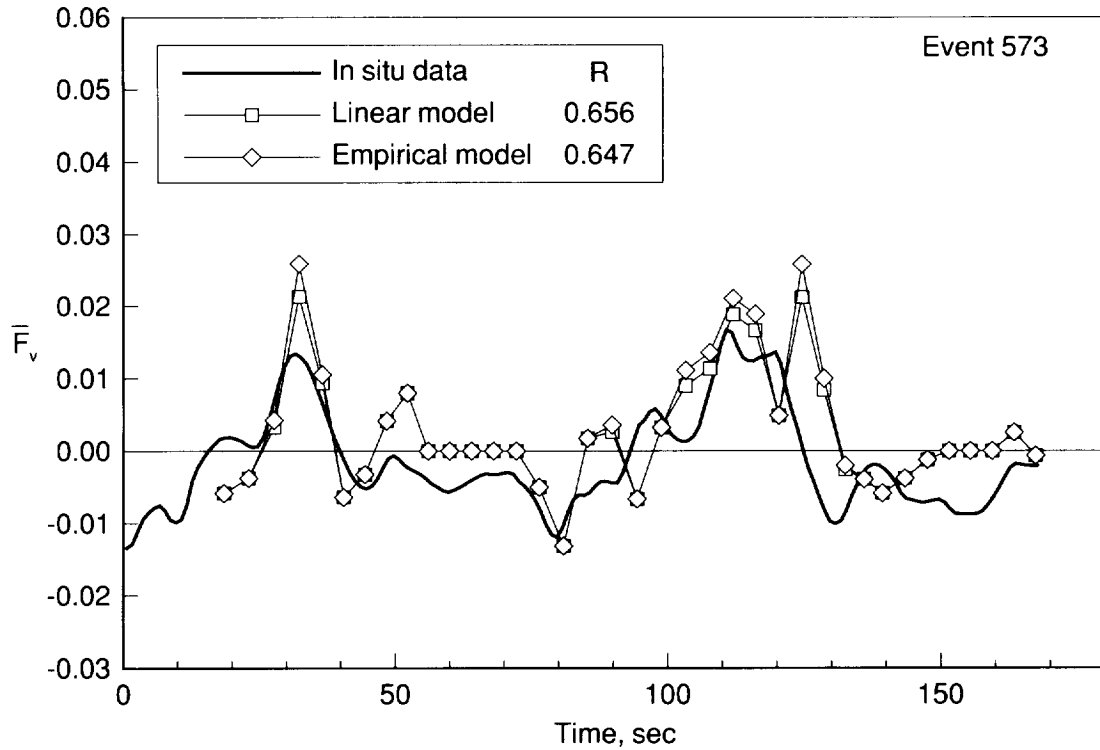
(j) Event 573.

Figure 34. Concluded.
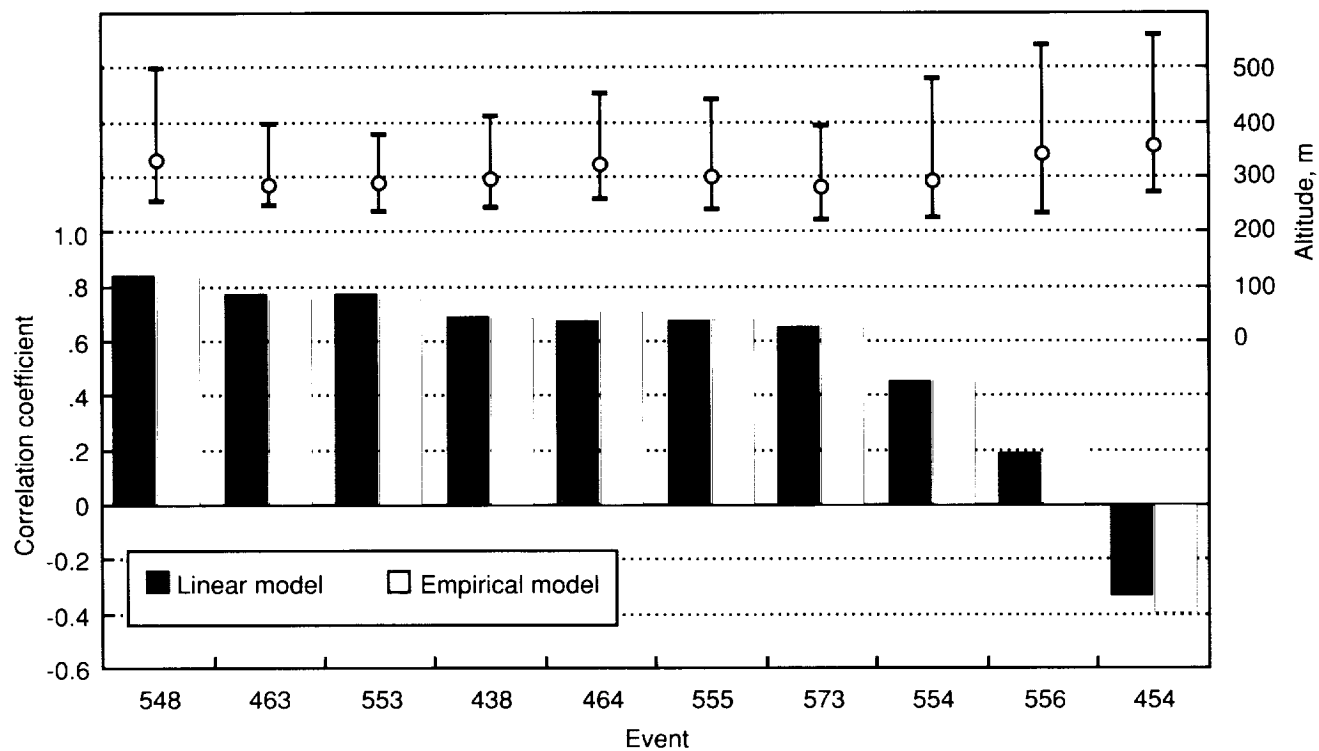
Figure 35. Correlation between in situ $\overline{F}$ and radar $\overline{F}_v$ for selected flight test events.
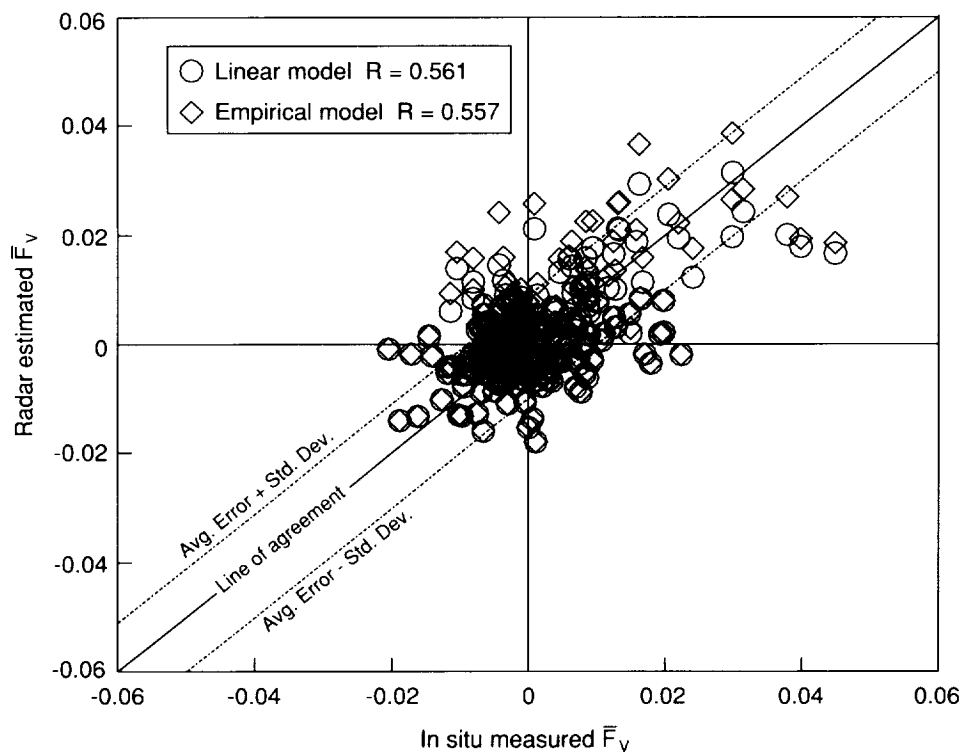

Figure 36. Summary of in situ $\overline{F}_v$ and radar $\overline{F}_v$ for selected flight test events with corresponding R.

ERRATA

NASA Technical Paper 3460
DOT/FAA/RD-94/7

MICROBURST VERTICAL WIND ESTIMATION FROM HORIZONTAL WIND MEASUREMENTS

Dan D. Vicroy
December 1994

Page 6: Equation (24) should be

$$q(z_m) = -\lambda \left\{ \frac{z_{max}}{c_1} \left[\exp\left(c_1 \frac{z_m}{z_{max}} \right) - 1 \right] - \frac{z_{max}}{c_2} \left[\exp\left(c_2 \frac{z_m}{z_{max}} \right) - 1 \right] \right\}$$

Page 6: Equation (31) should be

$$\eta(z_m) = \frac{\dfrac{z_{max}}{c_1} \left[\exp\left(c_1 \dfrac{z_m}{z_{max}} \right) - 1 \right] - \dfrac{z_{max}}{c_2} \left[\exp\left(c_2 \dfrac{z_m}{z_{max}} \right) - 1 \right]}{\exp\left(c_1 \dfrac{z_m}{z_{max}} \right) - \exp\left(c_2 \dfrac{z_m}{z_{max}} \right)}$$

REPORT DOCUMENTATION PAGE

1. AGENCY USE ONLY *(Leave blank)*	2. REPORT DATE December 1994	3. REPORT TYPE AND DATES COVERED Technical Paper

4. TITLE AND SUBTITLE
Microburst Vertical Wind Estimation From Horizontal Wind Measurements

5. FUNDING NUMBERS
WU 505-64-13-01

6. AUTHOR(S)
Dan D. Vicroy

7. PERFORMING ORGANIZATION NAME(S) AND ADDRESS(ES)
NASA Langley Research Center
Hampton, VA 23681-0001

8. PERFORMING ORGANIZATION REPORT NUMBER
L-17376

9. SPONSORING/MONITORING AGENCY NAME(S) AND ADDRESS(ES)
National Aeronautics and Space Administration
Washington, DC 20546-0001

10. SPONSORING/MONITORING AGENCY REPORT NUMBER
NASA TP-3460

DOT/FAA/RD-94/7

11. SUPPLEMENTARY NOTES

12a. DISTRIBUTION/AVAILABILITY STATEMENT

Unclassified–Unlimited

Subject Category 05

12b. DISTRIBUTION CODE

13. ABSTRACT *(Maximum 200 words)*
The vertical wind or downdraft component of a microburst-generated wind shear can significantly degrade airplane performance. Doppler radar and lidar are two sensor technologies being tested to provide flight crews with early warning of the presence of hazardous wind shear. An inherent limitation of Doppler-based sensors is the inability to measure velocities perpendicular to the line of sight, which results in an underestimate of the total wind shear hazard. One solution to the line-of-sight limitation is to use a vertical wind model to estimate the vertical component from the horizontal wind measurement. The objective of this study was to assess the ability of simple microburst environment. Both simulation and flight test measurements were used to test the vertical wind models. The results indicate that in the altitude region of interest (at or below 300 m), the simple vertical wind models improved the hazard estimate. The radar simulation study showed that the magnitude of the performance improvement was altitude dependent. The altitude of maximum performance improvement occurred at about 300 m.

14. SUBJECT TERMS
Microburst; Downburst; Simulation; Wind shear

15. NUMBER OF PAGES
83

16. PRICE CODE
A05

17. SECURITY CLASSIFICATION OF REPORT Unclassified	18. SECURITY CLASSIFICATION OF THIS PAGE Unclassified	19. SECURITY CLASSIFICATION OF ABSTRACT Unclassified	20. LIMITATION OF ABSTRACT